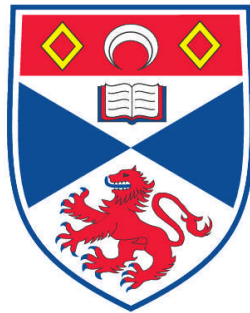


**NUMERICAL MODELING OF MODIFIED NEWTONIAN
DYNAMICS IN GALAXIES:
TESTING THE EXTERNAL FIELD EFFECTS**

Xufen Wu

**A Thesis Submitted for the Degree of PhD
at the
University of St. Andrews**



2010

**Full metadata for this item is available in
Research@StAndrews:FullText
at:**

<https://research-repository.st-andrews.ac.uk/>

**Please use this identifier to cite or link to this item:
<http://hdl.handle.net/10023/1706>**

This item is protected by original copyright

**This item is licensed under a
Creative Commons License**

**Numerical Modeling of Modified Newtonian Dynamics in galaxies :
Testing the External Field Effects**

by

Xufen Wu

Submitted for the degree of Doctor of Philosophy in Astrophysics

15th October 2010



University
of
St Andrews

Declaration

1. Candidate's declarations:

I, Xufen Wu, hereby certify that this thesis, which is approximately 33,000 words in length, has been written by me, that it is the record of work carried out by me and that it has not been submitted in any previous application for a higher degree.

I was admitted as a research student in 09, 2006 and as a candidate for the degree of PhD Physics in 09, 2006; the higher study for which this is a record was carried out in the University of St Andrews between 2006 and 2010.

Date

Signature of candidate

2. Supervisor's declaration:

I hereby certify that the candidate has fulfilled the conditions of the Resolution and Regulations appropriate for the degree of PhD Physics in the University of St Andrews and that the candidate is qualified to submit this thesis in application for that degree.

Date

Signature of supervisor

3. Permission for electronic publication:

In submitting this thesis to the University of St Andrews we understand that we are giving permission for it to be made available for use in accordance with the regulations of the University Library for the time being in force, subject to any copyright vested in

the work not being affected thereby. We also understand that the title and the abstract will be published, and that a copy of the work may be made and supplied to any bona fide library or research worker, that my thesis will be electronically accessible for personal or research use unless exempt by award of an embargo as requested below, and that the library has the right to migrate my thesis into new electronic forms as required to ensure continued access to the thesis. We have obtained any third-party copyright permissions that may be required in order to allow such access and migration, or have requested the appropriate embargo below.

The following is an agreed request by candidate and supervisor regarding the electronic publication of this thesis: Access to Printed copy and electronic publication of thesis through the University of St Andrews.

Date

Signature of candidate

Date

Signature of supervisor

Abstract

Galaxies are natural laboratories for testing fundamental physics on the nature of the dark matter. Modified Newtonian Dynamics (MOND) has been tested for over 20 years on small and large scales. While there are several versions of how MOND extrapolates to the large scales, and these versions are not yet fully successful, the original Bekenstein-Milgrom version of MOND is fully predictive and works very well on galaxy scales. However, little work has been done to explore this theory beyond fitting the rotation curves and Tully-Fisher relation of isolated disc galaxies. So far little is known of MONDian elliptical galaxies accelerating in any galaxy cluster. A defining feature of MOND is that internal dynamics of the galaxy depends on the overall acceleration of the galaxy. The existence of cuspy triaxial equilibria for elliptical galaxies is the minimal requirement to MOND. With the PhD project here, I constructed and then further studied the evolution and stability of gravitationally bound systems resembling like cuspy elliptical galaxies, both in isolation and when embedded in a uniform external field. I also studied the escape speeds from spiral galaxies, in particular by comparing the potentials of the Milky Way Galaxy in the Cold Dark Matter (CDM) and MOND frameworks.

Acknowledgements

I am heartily thankful to my supervisor, Dr. HongSheng Zhao. This thesis would not have been possible unless with his supervision, encouragement and support from the initial to the final level.

I owe my deepest gratitude to my parents and my sister Mengfang, who supported me all the time during my PhD study. I would like to thank my husband, Guozhu, who encouraged me a lot in the completion of the project and helped me polish the English of this thesis.

It is an honor for me to thank my collaborators: Benoit Famaey, Yougang Wang, Gianfranco Gentile, Alexander Knebe, Claudio Llinares, Martin Feix, Garry Angus, Anie Robin, Françoise Combes, Oliver Teret, Hagai Perets and Olivier Bienaymé, those who made this thesis possible.

I would like to show my gratitude to the people in Astronomy group: Moira Jardine, Simon Driver, Andrew Cameron, Ian Bonnell, Keith Horne, Jane Greaves, Christiane Helling and those who supported me in any respect during the completion of the thesis project.

I thank my thesis examiners: Prof. James Binney and Prof. Keith Horne, their careful reading on my thesis and detailed comments help a lot to improve the quality of my thesis.

I am indebted to many of my colleagues and friends for supporting me during the three and a half years: Scott Gregory, Leslie Hebb, Anaëlle Halle, Carsten Weidner, Noé Kains, Rowan Smith, David Hill, Ian Taylor, Katharine Johnston, Pauline Lang, Joy, kyoung Jin, Hubing, Lining and those who smiled friendly during the coffee breaks and pubs times, who helped me improving my English speaking.

Lastly, I offer my regards and blessings to all of those who supported me in any respect during the completion of the thesis project.

Contents

Declaration	i
Abstract	iii
Acknowledgements	v
1 The MODified Newtonian Dynamics	1
1.1 Basic ideas of MOND	4
1.1.1 Empirical MOND formula	5
1.1.2 Conservation laws and Modified Gravity	8
1.1.3 MOND as a Modified Inertia	11
1.1.4 Relativistic MOND - Tensor-Vector-Scalar (TeVeS)	12
1.1.5 Dark Fluid: four-vector's covariant framework for MOND	16
1.2 External Field Effects	17
1.2.1 Binding energy of an accelerating Milky Way	19
1.3 Predictions of MOND	20
2 External Fields and Escape Speeds	25
2.1 Loss of Mass and Stability of Galaxies in MODified Newtonian Dynamics	26
2.1.1 Models for HSBs and LSBs	28
2.1.2 Fast-accelerating galaxies in clusters	29
2.1.3 Conclusion and discussion	30
2.2 Milky Way potentials in cold dark matter and MODified Newtonian Dynamics - Is the Large Magellanic Cloud on a bound orbit?	33
2.2.1 Potential of the Milky Way	33
2.2.2 Axis ratios and Phantom dark matter	37
2.2.3 Circular and escape velocities	42
2.2.4 Conclusion & Discussion	50

3	Schwarzschild’s method and MONDian field elliptical galaxies	53
3.1	An introduction to Schwarzschild’s approach	54
3.2	Models, Schwarzschild technique, and ICs for N-body	56
3.2.1	MONDian Gravity	56
3.2.2	Initial Potential	57
3.2.3	Schwarzschild technique	57
3.2.4	ICs for N-body systems	66
3.3	N-body simulations in MOND	67
3.3.1	Technical Details	67
3.3.2	Virial Theorem	69
3.3.3	Energy Distribution	71
3.3.4	Kinetics	74
3.3.5	Mass distributions	76
3.3.6	Shape	78
3.4	Conclusions and Discussion	81
4	Stability and Evolution of Galaxies in External Fields	83
4.1	The Stability of Galaxies in Uniform External Fields	84
4.1.1	MOND, mass models and static potentials	86
4.1.2	Schwarzschild Technique and Model Self-consistency	89
4.1.3	N-body and stability	94
4.1.4	Kinetic energy and shape	102
4.1.5	Conclusion and discussion	106
4.2	Cluster galaxies are non-axisymmetric in MOND	109
4.2.1	Lopsidedness and offset of the center of gravity	109
4.2.2	Schwarzschild and N-body models	111
4.2.3	Conclusion	112
5	Conclusion	117
5.1	Summary	117
5.2	Future work	118
5.2.1	Galaxy mergers and elliptical galaxies	120

A Phantom Dark Matter in External Fields	123
A.1 Vertical kinematics of the Galaxy	124
A.2 Offsets of density peaks for PDM	125
A.2.1 The Simulations	126
A.2.2 Density Peak Offsets	127
B Comparison with another MOND solver	131
Bibliography	134

List of Figures

1.1	Mass to light ratio vs. galaxy colour	2
1.2	Baryonic Tully-Fisher relation	2
1.3	Rotation curves of various galaxies	7
1.4	MOND μ -functions	8
1.5	The gravity contour of the “bullet cluster” 1E0657-56	18
1.6	Different shapes of rotation curves of LSB(NGC1560) and HSB (NGC2903) galaxies	22
2.1	Milky Way-like galaxy in external fields	29
2.2	NGC 1560-like galaxy in external fields	31
2.3	Isopotentials of the Milky Way on the $x - z$ plane.	37
2.4	The MW Potential axis ratio $z - x$	38
2.5	Isodensity of phantom dark matter in a MOND Milky Way	38
2.6	The RCs and escape speeds of MW in MOND and CDM	42
2.7	MONDian MW comparing with CDM KZS and Bsc models	45
2.8	MONDian MW and CDM RAVE models	45
2.9	Hot gas in the MW	50
3.1	Cell segmentation in Schwarzschild’s method	59
3.2	Shapes of orbits from different families	62
3.3	The orbital structure without and with regularization	63
3.4	The period of circular orbits	69
3.5	Flowchart of the simulations	70
3.6	Virial ratio and v_{rms} vs. time	71
3.7	Evolution of energy distribution	73
3.8	Evolution of $\sigma_r(r)$ and $\beta(r)$	75
3.9	Mass and density vs. time	77

3.10	Axis ratio vs. time	78
3.11	Kinetics energy and mean square length vs. time	80
4.1	The lopsided potential of spherical density models	89
4.2	Circular orbital time vs. radius	92
4.3	The integrated contributions of different orbit families (without and with smoothed solutions)	93
4.4	Evolution of the virial ratio	97
4.5	The evolution of radii enclosing certain fraction of mass	99
4.6	The evolution of $\sigma_r(r)$ and $\beta(r)$	100
4.7	The evolution of kinetic energy and v_{rms}	103
4.8	Time evolution of the mean square length and angular momentum components	106
4.9	The evolution of lopsidedness $r^- : r^+$ of Models 1 and 3	107
4.10	Lopsided isopotentials	110
4.11	Color maps (centroid details) of xz-projected density	112
4.12	Color maps of xz-projected density on the scale of 10 kpc	113
4.13	Centroids offset of dwarf ellipticals in Virgo cluster	113
A.1	The radial density distributions of baryonic matter and dynamical matter .	125
A.2	Isodensity contours of the dynamical mass of model 1	127
A.3	Isodensity contours of the dynamical mass of model 2	128
A.4	Isodensity contours of the dynamical mass of model 3	128
A.5	Isodensity contours of the dynamical mass of model 4	129

List of Tables

2.1	Parameters of density model of NGC1560	30
2.2	NFW Profile Parameters for Milky Way	35
2.3	Velocities and Positions of Magellanic Clouds	44
2.4	Observed 3D velocity and escape velocity of the LMC	46
3.1	Model self-consistency	66
3.2	Total simulation times for isolated models	68
4.1	Parameters of the galaxy models	87
4.2	Galaxy model and Schwarzschild parameters	90
4.3	Model self-consistency and equilibrium	91
A.1	Models and parameters for studying offsets of phantom dark matter	126

1

The MODified Newtonian Dynamics

Newtonian dynamics predicts that the circular velocities v_{cir} at large radii in a galaxy follow a $v_{cir} \propto r^{-1/2}$ law. However the observations of the flat rotation curves of many spiral galaxies (Sofue & Rubin 2001, Sanders & McGaugh 2002) imply that there is a large amount of invisible mass which provides the additional gravity in the outer parts of galaxies (Bosma 1981b,a, Guhathakurta et al. 1988, Begeman 1989). It is logically necessary to introduce Dark Matter (DM) to the Newtonian dynamics to explain the problem of missing mass beyond the well examined scale of the solar system.

The current best Λ Cold Dark Matter (Λ CDM) model has yet to explain some most puzzling conspiracies of Dark Matter (DM) and baryons in galaxies, though it works very well on the large scale topics. One of the most famous puzzles is the baryonic Tully-Fisher relation, which is an empirical relation between galaxy luminosity and rotational velocity (Tully & Fisher 1977). Luminosity is proportional to stellar mass. The left panel of Fig. 1.1 shows the distribution of MOND fitting stellar mass-to-light ratio M_d/L_K in the K-Band (near infrared), for a sample of 30 Ursa Major spiral galaxies. Here, M_d is the

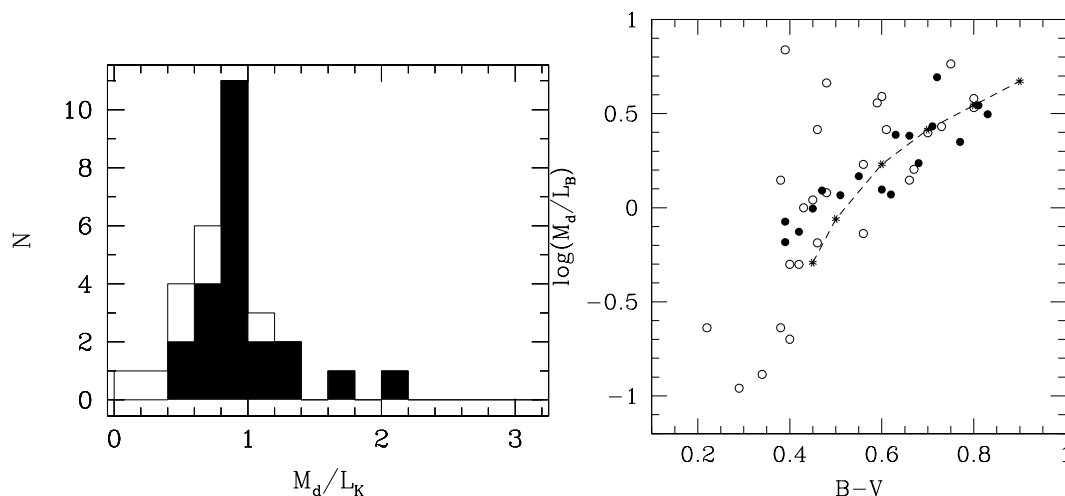


Figure 1.1: The **left panel** is the histogram of mass-to-light ratio in the near infrared M_d/L_K , for 30 (white + black histogram) Ursa Major galaxies, and the black histogram is a sub-sample of 23 objects without obvious disturbances in the velocity fields (Sanders & Verheijen 1998). The M_d is the mass of the stellar disc, which is determined from MOND. The histogram of mass-to-light ratio has a peak between 0.8 and 1.0. **right panel** (Sanders & Verheijen 1998) shows the mass-to-light ratio of 17 Ursa Major galaxies (solid circles) versus the reddening-corrected B-V colour index. The empty circles are another sample of 33 field galaxies in Sanders (1996), and the dashed line is the prediction of mass-to-light (blue) ratio versus B-V colours from population synthesis models of Larson & Tinsley (1978).

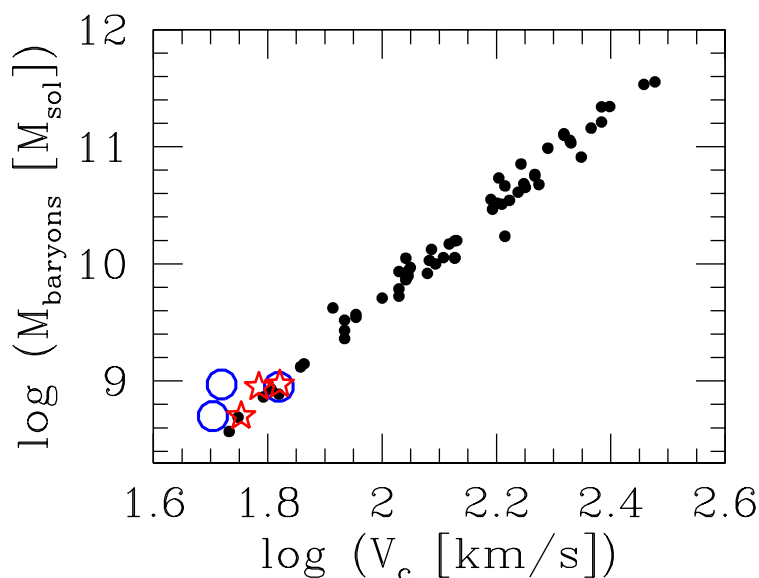


Figure 1.2: The baryonic Tully-Fisher relation, figure is from Gentile et al. (2007a). The solid circles are the data from disc galaxies (McGaugh 2005), the blue empty circles and red empty stars are tidal dwarf galaxies (Gentile et al. 2007a) with inclination angles $i = 45^\circ$ and $i = \text{free parameter}$.

stellar disc mass and L_K is the K-band luminosity. The only free parameter is the stellar mass M_d . Obviously, the histogram of M_d/L_K has a peak between 0.8 – 1.0. The right panel of Fig. 1.1 shows the relation between the MOND fitting mass-to-light ratio M/L_B and the B-V colour index for 17 Ursa Major galaxies (solid circles), which is compared with another sample of 33 field galaxies (empty circles Sanders & Verheijen 1998, Sanders 1996). The solid line is the prediction of mass-to-blue light ratio versus B-V made in the work of Larson & Tinsley (1978). The trends of M/L_B fitted within MOND for two samples agree well with the theoretical prediction in Larson & Tinsley (1978): the bluer the galaxies are, the smaller the M/L_B is; the redder the galaxies are, the larger the M/L_B is. In McGaugh et al. (2000), they found that it is more fundamental to study a relation between the rotation curve and total baryonic mass, including stars and gas. Fig. 1.2 shows the baryonic Tully-Fisher relation Gentile et al. (2007a), where the total baryonic mass M is proportional to v_{cir}^4 , v_{cir} being the circular velocity, for galaxies with $10^{8.5} - 10^{12} M_\odot$.

The mass-to-light ratio is determined by the Initial Mass Function (IMF) and the age of galaxy:

$$\frac{M}{L}(t) = \frac{\int_0^t \int (\mu(m, \tau) dN/dm) dm S(t - \tau) d\tau}{\int_0^t \int (l(m, \tau) dN/dm) dm S(t - \tau) d\tau}. \quad (1.1)$$

Where t is time now, $S(t - \tau)$ is the star formation rate in solar mass per year at an earlier time τ , $\mu(m, \tau)$ and $l(m, \tau)$ are the mass and luminosity, respectively, of a star of initial mass m after an age τ . The IMF is defined as (Salpeter 1955)

$$\frac{dN}{dm} \propto m^{-\alpha}, \quad (1.2)$$

where N is the number of stars and m is the mass of a star. The constant $\alpha = 2.35$ for mass m in the range $0.4 \rightarrow 10 M_\odot$, as discussed in Salpeter (1955). After integrating out the mass variable, one can obtain the mass-to-light ratio. The work Kroupa (2001) suggested a universal multi-part power-law IMF, with the following values of α :

$$\begin{aligned} \alpha &= 0.3 \pm 0.7, & 0.01 M_\odot \leq m \leq 0.08 M_\odot, \\ \alpha &= 1.3 \pm 0.5, & 0.08 M_\odot \leq m \leq 0.50 M_\odot, \\ \alpha &= 2.3 \pm 0.3, & 0.50 M_\odot \leq m \leq 1.00 M_\odot, \\ \alpha &= 2.3 \pm 0.7, & 1.00 M_\odot \leq m. \end{aligned} \quad (1.3)$$

Apart from the baryonic Tully-Fisher relation etc., new observations reveal that:

(1) Dark Matter effects are present even in the newly formed tidal dwarf galaxies (Gentile et al. 2007), while the DM density is expected to be very low in the tidal arms of merging galaxies in the CDM framework. However, any galaxies formed in tidal arms must be mostly baryonic, like star clusters.

(2) A universal scale sets the baryonic gravity at the edge of the dark matter core in galaxies (Gentile et al. 2009, Milgrom 2009c). At this scale, the so-called core radii of dark matter halos, the surface density of baryons is also a constant, which implies a strong correlation between the surface density of baryons and dark matter. This is a scale that does not exist naturally in the classical CDM framework.

It is hard for CDM to solve these coincidence problems even in the improved simulations of the baryonic physics since the fore-mentioned scales do not naturally exist. It is thus important to study alternative gravity theories, among which the MODified Newtonian Dynamics (MOND) is the most advanced one.

1.1 Basic ideas of MOND

Indeed, without resorting to the galactic dark matter, the simple prescription of MOND is amazingly successful. It leads to excellent predictions of the rotation curves for galaxies with mass ranging over five decades (see, e.g., Sanders & McGaugh 2002 for a review), including our own Milky Way (Famaey & Binney 2005, Famaey et al. 2007a). MOND successfully matches the observations made on a wide range of scales in different types of galaxies, including dwarfs and giants, spirals and ellipticals (Milgrom 2007, Gentile et al. 2007b, Milgrom & Sanders 2007, Famaey & Binney 2005, Sanders & Noordermeer 2007, Angus 2008). It can also perfectly explain the vertical kinetics of disk galaxies in the absence of CDM, which has recently been done by Bienaymé et al. (2009). Furthermore, the development of different covariant theories incorporating the dynamics of MOND (e.g., Bekenstein 2004a, Zlosnik et al. 2007a, Bruneton & Esposito-Farèse 2007a, Zhao 2007, Sanders 2005a, Skordis 2008) (see also the most recent review of Ferreira & Starkman 2009) allows to apply MOND theory to other fields such as cosmology (e.g., Skordis et al. 2006a, Dodelson & Liguori 2006a, Schmidt et al. 2007, Zhang et al. 2007) and gravitational lensing (e.g., Chiu et al. 2006, Qin et al. 1995, Zhao et al. 2006a, Angus

et al. 2007a, Takahashi & Chiba 2007, Feix et al. 2008a,b).

1.1.1 Empirical MOND formula

Although there are several versions of MOND, (e.g. Milgrom 1983c,a,b, Bekenstein 2006, Milgrom 2008a, Zhao 2008), they all postulate that the Newtonian gravitational acceleration g_N is replaced by $g \sim \sqrt{g_N a_0}$ when the gravitational acceleration is much smaller than the acceleration constant $a_0 = 1.2 \times 10^{-10} \text{ms}^{-2} = 3700 (\text{km s}^{-1})^2 \text{kpc}^{-1}$, which is a rather weak field and is about 11 orders of magnitude smaller than the acceleration of gravity on the Earth's surface. This value comes from the rotation curves of 10 nearby galaxies (Begeman et al. 1991, Sanders & McGaugh 2002). The original formula proposed by Milgrom (1983c) is:

$$\mu\left(\frac{|\vec{g}|}{a_0}\right) \vec{g} = \vec{g}_N, \quad (1.4)$$

To produce both the Newtonian and MONDian limits, the interpolating function $\mu(x)$ has to be of the following form ($x = |\vec{g}|/a_0$):

$$\mu(x) \sim x \quad |\vec{g}| \ll a_0, \quad (1.5)$$

$$\mu(x) \sim 1 \quad |\vec{g}| \gg a_0. \quad (1.6)$$

In the weak field limit, we have $\sqrt{\frac{GMa_0}{r^2}} = \frac{v_{cir}^2}{r}$ with M being the total mass of baryons in the system, hence the circular velocity $v_{cir} \propto M^{1/4}$ is a constant and the rotation curve is flat at large radius. If the mass-to-light ratio M/L is a constant, then $v_{cir} \propto L^{1/4}$, which is the baryonic Tully-Fisher relation (Sanders & McGaugh 2002).

MOND can be understood as an effective dark matter theory if we assume that *the dark matter distribution is 100% correlated to the distribution of baryons* although such effective DM could even be negative (see Fig. 2.5 in §2.2.2). Hence MOND has less freedom than the CDM models. However, it does have several important freedoms: the mass-to-light ratio (M/L) of the system, the interpolating function μ , and the environment in which the galaxy is situated. There are a number of popular forms of the μ function satisfying the asymptotic behavior, such as the ‘Standard μ ’ proposed by Milgrom (1983a), Bekenstein’s toy μ -function, and the ‘simple μ ’ suggested by Famaey &

Binney (2005), which are:

$$\mu(x) = \frac{x}{\sqrt{1+x^2}}, \quad \textit{Standard} \quad (1.7)$$

$$\mu(x) = \frac{\sqrt{1+4x}-1}{\sqrt{1+4x}+1}, \quad \textit{Bekenstein} \quad (1.8)$$

$$\mu(x) = \frac{x}{(1+x)}, \quad \textit{Simple} \quad (1.9)$$

The ‘standard μ function’ is usually used in fitting the rotation curves, see e.g. Begeman et al. (1991), Sanders & Verheijen (1998). However, from the investigation within Bekenstein’s Tensor-Vector-Scalar theory (i.e. relativistic MOND, see §1.1.4 by Zhao & Famaey (2006)), it is known that in the presence of an external field the scalar field is distorted by a factor of $\frac{1}{\sqrt{\Delta_1}}$ along the external field direction, at the meanwhile the ‘standard’ μ function makes the scalar field \vec{g}_s change non-monotonically with the Newtonian gravity \vec{g}_N . The dilation factor $\Delta_1 = 1 + \frac{d \ln \mu_s(s)}{d \ln |g_s|}$. As a result, there are two values of $|\vec{g}_N|$ at the same $|\vec{g}_s|$. The non-relativistic spherical MOND acceleration \vec{g} has a one-to-one relation to \vec{g}_N (see Eq. 1.4), and the interpolation function in non-relativistic MOND $\mu(x)$ is determined by $x \equiv |\vec{g}|/a_0$. Therefore, the TeVeS’ scalar function $\mu_s(s) \equiv \frac{\mu(x)}{1-\mu(x)}$ (here $s \equiv |\vec{g}_s|/a_0$) has two values for the same scalar field \vec{g}_s , which leads to the dilation factor Δ_1 could be negative. This is unphysical since the distortion factor is $\frac{1}{\sqrt{\Delta_1}}$.

The μ -function used in Bekenstein’s TeVeS theory (Bekenstein 2004b) is more successful in producing lensing signal than the other popular μ -functions. However, it does not work well in fitting the rotation curves of galaxies (Zhao et al. 2006b).

The ‘simple’ μ function in Eq.1.9 was proposed in Famaey & Binney (2005). Using this μ function, MOND fits better the terminal velocity of the Milky Way and NGC3198. Zhao & Famaey (2006) further showed that the ‘simple’ μ works better in both very weak and very strong gravities (see Fig. 1.3 for the best fit to the Rotation Curves of galaxies with simple μ). Besides, there is a monotonically increasing TeVeS’ scalar function $\mu(g_s)$ versus g_N when using this μ function. In Figure 1.4, we present different forms of popular μ functions transiting from deep MOND to Newtonian gravities. Apparently, the ‘standard’ μ goes to the Newtonian dynamics most rapidly, while the Bekenstein μ goes most gradually. Because of the excellent behavior of the ‘simple’ μ function on the galactic scale, we shall use it in all chapters of this thesis to test the MONDian gravity.

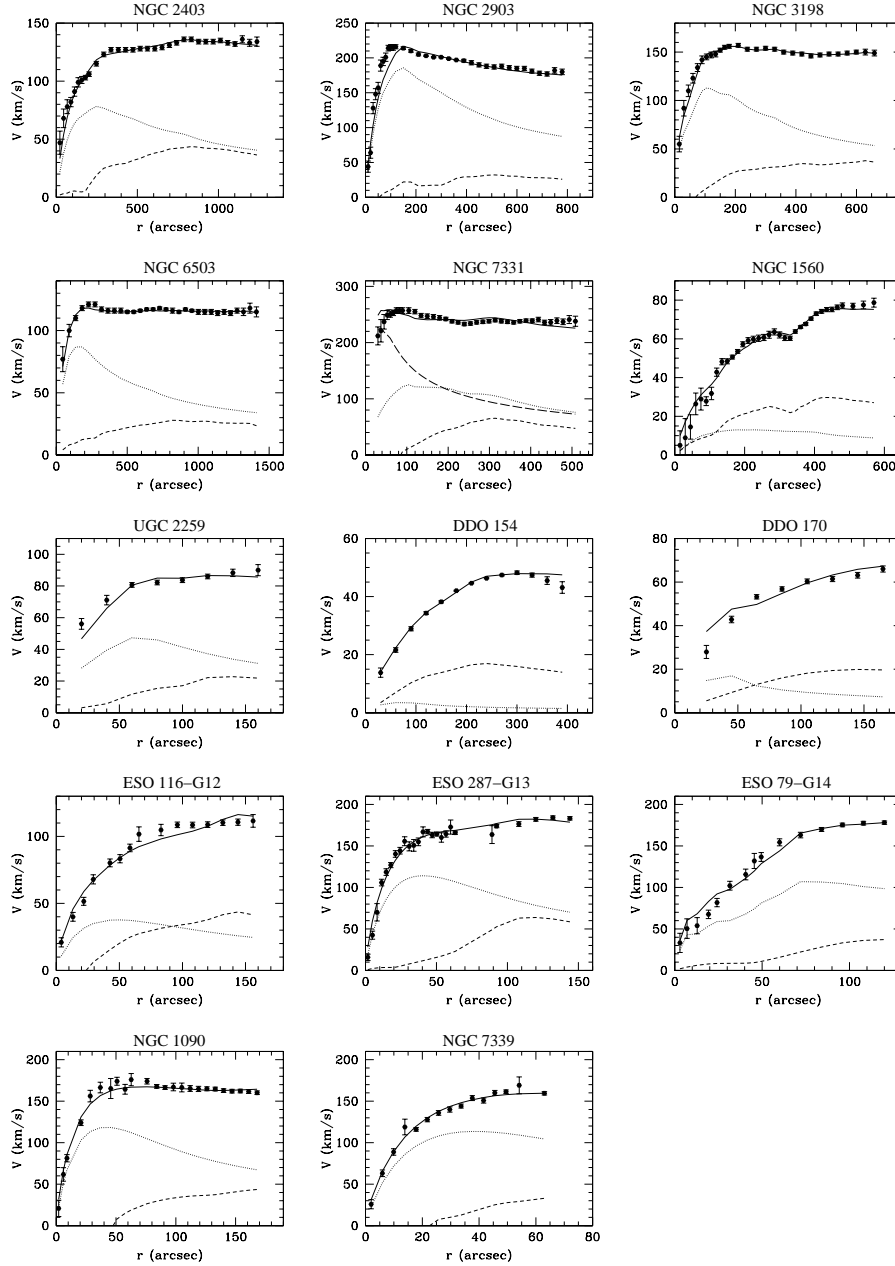


Figure 1.3: Rotation curves of various galaxies with the “simple” μ function (Eq. 1.9): The line types are : MOND fitting (solid line), Newtonian fitting for disc (dotted), gas component (dashed) and bulge (long-dashed). (Famaey et al. 2007a)

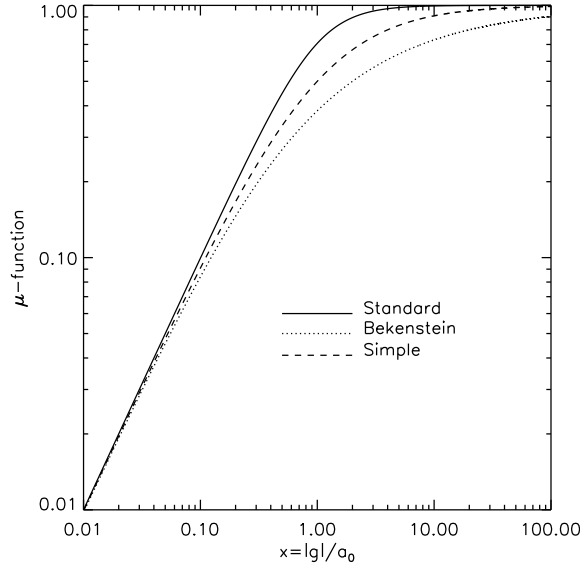


Figure 1.4: Different forms of μ -function versus $x \equiv |\vec{g}|/a_0$.

1.1.2 Conservation laws and Modified Gravity

Although the empirical MOND formula, i.e, Eq. 1.4 explains well the phenomena of Tully-Fisher relation for many spiral galaxies, it breaks the momentum conservation, especially in N-body systems. In order to propose a more promising MOND theory, Bekenstein & Milgrom (1984, hereater BM84) suggested a modified Lagrangian of gravity

$$L = - \int \left[\frac{a_0^2}{8\pi G} \mathcal{F} \left(\frac{|\nabla\Phi|^2}{a_0^2} \right) + \rho\Phi \right] d^3X. \quad (1.10)$$

Here \mathcal{F} is an arbitrary positive function, ρ is the baryonic mass density, Φ is the modified gravitational potential, and the MONDian acceleration $\mathbf{g} = -\nabla\Phi$. This Aquadratic Lagrangian (AQUAL) gives the Newtonian dynamics in the limit of

$$L = - \int \left[\frac{|\nabla\Phi|^2}{8\pi G} + \rho\Phi \right] d^3X, \quad (1.11)$$

while $\mathcal{F}(x^2) \rightarrow x^2$, $x = \frac{|\nabla\Phi|}{a_0}$, and the Eq. 1.11 gives the Newtonian linear Poisson equation $\nabla^2\Phi = 4\pi G\rho$. When $\mathcal{F}(x^2) = x^3$, it is the deep MOND limit. The variation of action S

with respect to Φ with the boundary condition $\Phi_\infty = 0$ is:

$$\frac{\delta S}{\delta \Phi} = 0, \quad (1.12)$$

$$S = \int \mathcal{L} dX^4 = \int \left[\frac{a_0^2}{8\pi G} \mathcal{F} \left(\frac{|\nabla \Phi|^2}{a_0^2} \right) + \rho \Phi \right] d^4 X, \quad (1.13)$$

where \mathcal{L} is the Lagrangian density. One can obtain the Euler-Lagrange equation from the variation principle of Eq. 1.12:

$$\frac{\partial \mathcal{L}}{\partial \Phi} = \nabla \left(\frac{\partial \mathcal{L}}{\partial (\nabla \Phi)} \right). \quad (1.14)$$

Since

$$\frac{\partial \mathcal{L}}{\partial \Phi} = \rho; \quad (1.15)$$

$$\begin{aligned} \nabla \left(\frac{\partial \mathcal{L}}{\partial (\nabla \Phi)} \right) &= \nabla \left(\frac{a_0^2}{8\pi G} \frac{\partial \mathcal{F}}{\partial (\nabla \Phi)} \frac{2(\nabla \Phi)}{a_0^2} \right) \\ &= \frac{1}{4\pi G} \nabla \left(\frac{\partial \mathcal{F}}{\partial (\nabla \Phi)} (\nabla \Phi) \right) \\ &= \frac{1}{4\pi G} \nabla (\mu \nabla \Phi) \end{aligned} \quad (1.16)$$

Here we obtain the MOND Poisson Equation:

$$\nabla \cdot [\mu(|\nabla \Phi|/\mathbf{a}_0) \nabla \Phi] = 4\pi \mathbf{G} \rho, \quad (1.17)$$

where μ function is derived from

$$\mu(\sqrt{y}) = d\mathcal{F}(y)/d(y), \quad y = x^2. \quad (1.18)$$

In BM84 the Newtonian gravity Φ_N and modified gravity Φ (i.e. dynamical gravity) has the following relation:

$$\mu(|\nabla \Phi|/\mathbf{a}_0) \nabla \Phi = \nabla \Phi_N + \nabla \times \mathbf{h}. \quad (1.19)$$

The curl term $\nabla \times \mathbf{h}$ makes MOND gravity a curl-free gravity, i.e., one can define a potential independent of the path, (direction etc.), hence the new Poisson equation (Eq. 1.17) is ensured to keep the conservation laws. In systems with high symmetry, such as spherical, cylindrical, or axis-symmetric systems, the curl term is equal to zero and the formula goes

to the empirical MOND Eq. 1.4. The Lagrangian density in Eq. 1.10 is regardless to time, space and how it is oriented in space. Due to Noether's theorem, the momentum, angular momentum and energy of a self-gravitating system are all conserved. The curl term makes a correction of 5% – 10% to MOND (see Fig.3 in Brada & Milgrom 1995). However the curl correction can become large in the intermediate gravity regions by choosing the μ functions in the non-relativistic approximation of multi-field TeVeS gravity (Angus et al. 2006).

BM84 is consistent with the weak equivalence principle. It predicts that the center of mass of a small system (with mass m) will follow the orbit of $\mathbf{g} = -\nabla\Phi_{\text{ext}}$, where Φ_{ext} is external potential (with mass M) from the equation 1.19. The tidal effects can be neglected when $m \ll M$ and the orbit has nothing to do with material composition of the small mass m , and its internal density. More details about the external field effect and its application will be discussed in §2.2.3.

For a binary system with masses m_1, m_2 and distance r , the modified force in the weak field (deep MOND) limit between them predicted by BM84 is (Milgrom 1994b)

$$\mathcal{F}(m_1, m_2, r) = (2/3)(Ga_0)^{1/2}r^{-1}[(m_1 + m_2)^{3/2} - m_1^{3/2} - m_2^{3/2}]. \quad (1.20)$$

Milgrom further gave the similar force equation in an N-body system. The N-body simulations based on the equation of BM84 have been carried out on various topics:

In Tiret & Combes (2007) MOND was shown to produce stronger bars than CDM, and hydrodynamical simulations of spherical bulges indicated that there are tight correlations between bulge mass, central black hole and stellar velocity dispersion in MOND (Zhao et al. 2008). The dissipationless collapses were studied in Nipoti et al. (2006) and Nipoti et al. (2007a), where the end-products were found to be consistent with several observations. Nipoti et al. (2007b) found that the phase mixing is less effective and the timescale of galaxy mergers is longer in MOND than in CDM. Wu et al. (2009) and Wu et al. 2010 (submitted) studied the stability of cuspy, triaxial systems in MOND for both the isolated galaxies and the galaxies in a constant external field. Jordi et al. (2009) and Haghi et al. (2009) applied the external fields and studied the internal dynamics of distant star clusters.

Moreover, in Ciotti & Binney (2004), it was found that the two body relaxation is faster in the framework of BM84 than in Newtonian dynamics. At the same time, the dynamical friction is also speeded up in the deep MOND region.

1.1.3 MOND as a Modified Inertia

Milgrom also suggested that the MOND effect may arise from the interaction of baryonic matter with the vacuum (Milgrom 1994a, 1999) and behave as a modification of the particle inertia. In this argument, the kinetic action of a particle in Newtonian $\int dt v^2(t)/2$ is modified to $A_m S[a_0, \{\mathbf{r}_i(t)\}]$. Here, A_m can be identified as the particle mass. S is a functional of the particle trajectory $\{\mathbf{r}_i(t)\}$ and is also a function of a_0 . Hence the Newtonian Poisson equation does not change, while the equation of motion of the particle becomes

$$\mathbf{A}[\{\mathbf{r}(t)\}, \mathbf{a}_0] = -\tilde{\nabla}\phi. \quad (1.21)$$

Here \mathbf{A} is a functional of $\{\mathbf{r}_i(t)\}$, and a function of a_0 . The action satisfies:

$$S \rightarrow \int dt \frac{v^2}{2} \quad (\text{Newtonian}) \quad a_0 \rightarrow 0; \quad (1.22)$$

$$S \rightarrow a_0^{-1} s[\mathbf{r}(t)] \quad (\text{MOND}) \quad a_0 \rightarrow \infty. \quad (1.23)$$

At the above limit, Milgrom (1994a) showed that if the action $S[a_0, \{\mathbf{r}_i(t)\}]$ is Galilei invariant, it must be strongly non-local, i.e, the motion of the particle depends on the past trajectory, as well as non-linear. Milgrom (1994a) also found that for an axisymmetric system, the dynamics of circular motion is as simple as the empirical MOND formula (Eq. 1.4), although not exactly true for other generic systems.

The coincidence of $a_0 \approx cH_0$ implies that MOND is an effective theory whose cosmology could possibly change dynamics. However, cosmology does not necessarily affect the motion of the particle directly, and it is possible that the vacuum affects both cosmology and dynamics, considering the coincidence of $a_0 \approx c\sqrt{\Lambda}$, where c is the speed of light and Λ is the cosmological constant.

Observable Differences

There are some observable differences between Modified Gravity and Modified Inertia, as follows (Milgrom 1994a):

1. The dynamics is different when there are other interactions. One can design an experiment to distinguish them: placing a probe in a strong external gravitational field $g_{ext} \gg a_0$, and then balancing the gravity with an electric force. The Modified Gravity predicts that the dynamics is at the Newtonian limit due to the strong gravitational field, while the Modified Inertia predicts modified equation of motion since the total acceleration (gravity and electric force) is very weak on the probe.
2. Conserved quantities such as energy, momentum and angular momentum are different in the two approaches: these quantities are modified in the Modified Inertia but not in the Modified Gravity, since they are derived from the kinetic actions. The studies on galaxy formation, mergers, accretion and relaxation predict different values of conserved quantities.¹
3. In the non-relativistic regime, one can have a relation that acceleration $\mathbf{g} \equiv -\nabla\Phi$ in the Modified Gravity approach, however there are no such simple relations for general orbits in Modified Inertia approach except those circular orbits in axis-symmetric potentials. This is due to the acceleration depending on both position and details of the trajectory, which also leads to the lack of a simple relation between Modified Inertia and Newtonian dynamics.

1.1.4 Relativistic MOND - Tensor-Vector-Scalar (TeVeS)

Actions of fields

There are several proposals for the relativistic version of MOND (Bekenstein & Milgrom 1984, Bekenstein & Sanders 1994, Sanders 1997), but none of them is very successful. Bekenstein (2004b) proposed the first Tensor-Vector-Scalar field theory to overcome the problems that appeared in the previous relativistic MOND proposals. TeVeS is based on three dynamical fields : a tensor field $g_{\mu\nu}$, a vector field A_μ and a scalar field ϕ . The gravitational metric $g_{\mu\nu}$ and the physical metric $\tilde{g}_{\mu\nu}$ are related by

$$\tilde{g}_{\mu\nu} = e^{-2\phi/c^2} g_{\mu\nu} - (e^{2\phi/c^2} - e^{-2\phi/c^2}) A_\mu A_\nu, \quad (1.24)$$

¹Milgrom argues that in a stationary system the two approaches can also have different predictions. For instance, the rotation curve, Modified Inertia predicts $\mu(g/a_0)g = g_N$, while Modified Gravity predicts $\mu(g/a_0)g = g_N + \nabla \times \mathbf{h}$, with a 5% – 10% correction. However we note that the empirical MOND relation is also valid on the rotational symmetric plane of an axis-symmetric potential in Modified Gravity. I.e., the system satisfies the simple relation in Modified Inertia should give the same relation in Modified gravity approach.

where A_μ is a timelike dynamical normalized vector field, and $g^{\mu\nu}A_\mu A_\nu = -1$. The dynamics of $g_{\mu\nu}$ is given by the conventional Einstein-Hilbert Lagrangian.

The basic equation of TeVeS is obtained by varying the total action, $S = S_g + S_\phi + S_A + S_m$, with respect to the fields $g_{\mu\nu}$, ϕ , a non-dynamical field σ and A_μ . The four components of the total action are :

$$S_g = \frac{1}{16\pi G} \int d^4x g^{\mu\nu} R_{\mu\nu} \sqrt{-g} \quad (1.25)$$

$$S_A = \frac{-K}{32\pi G} \int d^4x [g^{\mu\nu} g^{\alpha\beta} A_{[\mu,\alpha]} A_{[\nu,\beta]} - 2(\lambda/K)(g^{\alpha\beta} A_\alpha A_\beta + 1)] \sqrt{-g} \quad (1.26)$$

$$S_\phi = \frac{-1}{2} \int d^4x [\sigma^2 (g^{\mu\nu} - A^\mu A^\nu) \phi_{,\mu} \phi_{,\nu} + \frac{1}{2} G l^{-2} \sigma^4 \mathcal{F}(kG\sigma^2)] \sqrt{-g} \quad (1.27)$$

$$S_m = \int d^4x \mathcal{L}[\tilde{g}_{\alpha\beta}, f^\mu, \partial_\alpha f^\mu, \dots] e^{-2\phi} \sqrt{-g}. \quad (1.28)$$

In the equations above, g and $R_{\mu\nu}$ are Einstein-Hilbert determinant of $g_{\mu\nu}$ and Ricci tensor, G is the bare gravitational constant, not the measured gravitational constant on Earth which has a coupling effect with the measure, and λ is a spacetime-dependent Lagrange multiplier to enforce the normalization of $g^{\mu\nu}A_\mu A_\nu = -1$. There are three free parameters K , k , l and one free function \mathcal{F} in TeVeS. K is a dimensionless parameter setting the strength of the vector field A_μ , k is a dimensionless parameter which can be absorbed into the function \mathcal{F} , and l is a constant length setting the strength of potential. \mathcal{F} is a free dimensionless function determining the shape of potential-like term. The acceleration scale is $a_0 = \frac{\sqrt{3}kc^2}{4\pi l}$. In the matter action S_m , the $\mathcal{L}[\tilde{g}_{\alpha\beta}, f^\mu, \partial_\alpha f^\mu, \dots]$ is the flat spacetime Lagrangian. At the limit of $\{k \rightarrow 0, K \propto k, l \propto k^{-3/2}\}$, TeVeS is approaching GR (Bekenstein 2004b, 2006, 2009).

The non-relativistic limit of TeVeS equations are

$$\Phi = \Xi \Phi_N + \phi, \quad (1.29)$$

$$\Xi \equiv (1 - K/2)^{-1} e^{-2\phi_c/c^2}, \quad (1.30)$$

where ϕ_c is the value of scalar field ϕ in the cosmology model and Φ is the potential. When the parameters satisfy $\{0 < K \ll 1, |\phi_c| \ll c^2\}$, one has the Eq.1.29 approaching

$$\Phi = \Phi_N + \Phi_{effDM}. \quad (1.31)$$

Here the Φ_{effDM} is the potential of effective dark matter. By choosing the suitable \mathcal{F} function one can reproduce the μ -function ($\mu(x) = \frac{d\mathcal{F}(x)}{dx}$), hence reproduce the BM84 non-relativistic MOND equation from TeVeS. Later, Sanders (2005b) proposed a variant of TeVeS, with three free functions and one free parameter, and it works better than the original TeVeS on generating the cosmology evolution of a_0 . Due to the coincidence of $a_0 \sim cH_0$, people often argue that the a_0 should be determined by cosmology. Zlosnik et al. (2007b) also proposed another variant of TeVeS, which has a tensor-vector field, and the timelike vector is normalized by the metric $\tilde{g}_{\mu\nu}$. There are four parameters in their theory and the cosmology built on their theory has an inflation period at early stage and an accelerated expanding at late stage.

TeVes Lensing

The light rays in TeVeS are observables of the metric $\tilde{g}_{\mu\nu}$. In an isotropic TeVeS cosmological model, the metric $\tilde{g}_{\mu\nu}$ is only slightly different from the metric in General Relativity, hence the gravitational lensing is very similar to that in GR. The time independent line element is:

$$d\tilde{s}^2 = -(1 + 2\Phi/c^2)dt^2 + (1 - 2\Phi/c^2)(dx^2 + dy^2 + dz^2). \quad (1.32)$$

where the physical gravitational potential Φ is governed by Eq. 1.29. The metric (Eq. 1.32) is used in GR (with Φ replaced by Φ_N) when studying both dynamics and gravitational lensing. Note that in Eq. 1.32 the potential Φ appears in both terms on the right hand side, the acceleration discrepancy can be measured equally through the dynamics, which is sensitive to the first term, and the gravitational lensing, which is sensitive to both terms.

The first study of gravitational lensing, based on a point-like mass distribution, in TeVeS was by Chiu et al. (2006), who worked out the TeVeS lens equation, which controls the magnification of various images in strong lensing. They pointed out that for double-image lensing systems, the difference in magnifications is not as well defined as in GR. Later Zhao et al. (2006b) studied a Hernquist profile to model the baryonic mass distribution of galaxies for a large sample of double-image quasars. The masses of lenses are well estimated in two ways: by comparing the observations with predictions for both, image positions and magnification ratios. The mass estimates and the luminosity are well correlated, and the two methods are consistent. In Chen & Zhao (2006), Shan et al. (2008) the probability of double-image strong lensing occurring as a function of separation was studied by modeling

the spherical (Chen & Zhao 2006) and axis-symmetric (Chen & Zhao 2006) Hernquist profiles for elliptical galaxies in TeVeS.

The weak lensing of the “bullet cluster”, galaxy clusters 1E0657-56, also has been modeled in empirical MOND, BM84 and TeVeS in Angus et al. (2006, 2007b), Feix et al. (2008a), and they showed that pure baryons are not enough to generate the lensing signals, hence dark matter is needed even in MOND. Angus et al. (2007b) suggested that 2eV neutrinos can be the dark matter candidate instead of Cold Dark Matter, which is consistent with the MOND predictions on galactic scales. Later studies of lensing in cluster CL0024+17 (Jee et al. 2007, Famaey et al. 2008) showed that invisible mass (2eV neutrinos as the best candidate in Famaey et al. 2008) is needed. However Milgrom & Sanders (2008) argued that the additional dynamical density structures are actually expected in MOND, happening in the regions where MOND goes into Newtonian. In a later study by Knebe et al. (2009) they numerically showed that there are additional peaks of dynamical mass distribution in MOND, which could lead to the lensing signal of separation of visible mass and “dark matter”.

MOND Cosmology

Skordis et al. (2006b), Skordis (2006) has derived the formulae for the evolution of cosmological perturbations in TeVeS. They showed that without cold dark matter, TeVeS can predict perfectly the spatial distribution of galaxies and the spectrum of the cosmic microwave background radiation, under the existence of massive neutrinos and cosmology constant Λ . Dodelson & Liguori (2006b) further showed that it is the vector field that is responsible for the growth of large scale structure in the absence of dark matter. The relative velocity of the bullet cluster 1E0657-56 is about 4700 km s^{-1} , and it is difficult in Dark Matter simulations to produce such a high speed. Llinares et al. (2009) numerically showed that MOND cosmology simulations can generate higher speeds of clusters compared to CDM simulations.

Besides the dark matter puzzle, another mystery in cosmology is the dark energy which is responsible for the acceleration of Hubble expansion. Diaz-Rivera et al. (2006), Hao & Akhoury (2005), Zhao (2006), Zhao & Famaey (2006) studied the TeVeS cosmology. By choosing a suitable \mathcal{F} -function in TeVeS, they obtained cosmology models with an inflationary start, and an acceleration of Hubble expansion at the later time, without any

dark matter or dark energy. Hence TeVeS provides a possible unification to all the dark sectors in cosmology.

1.1.5 Dark Fluid: four-vector's covariant framework for MOND

At present, there are several covariant frameworks for MOND (see, e.g., Bekenstein 2004b, Sanders 2005b, Bruneton & Esposito-Farèse 2007b, Skordis 2008, Halle et al. 2008, Li & Zhao 2009, Milgrom 2009a, and references therein). In the quasi-static and weak field limits of these theories, the slightly bent metric for a galaxy is given by

$$g_{\alpha\beta}dx^\alpha dx^\beta = -(1 + \frac{2\Phi}{c^2})d(ct)^2 + (1 - \frac{2\Psi}{c^2})dl^2 \quad (1.33)$$

where $dl^2 = (dx^2 + dy^2 + dz^2)$ is the Euclidean distance in cartesian coordinates, and the Newtonian gauge is adopted with the potentials being $\Phi(x, y, z)$ and $\Psi(x, y, z)$.

As one of the simplest frameworks, one can adopt the $\nu\Lambda$ co-variant formulation of Zhao (2007) and Halle et al. (2008). The $\nu\Lambda$ model works as GR, except that the space-time is filled with a **Non-uniform** Dark Energy fluid described by a four-vector ν^α , with unit norm and parallel to the local time direction. If we define a dimensionless co-variant vector

$$E^\beta \equiv \frac{c^2 \nabla_{\parallel} \nu^\beta}{a_0} \sim (0, -\frac{\partial_x \Phi}{a_0}, -\frac{\partial_y \Phi}{a_0}, -\frac{\partial_z \Phi}{a_0}) \text{ near galaxies,} \quad (1.34)$$

where $\nabla_{\parallel} \nu = \nu^\alpha \nabla_\alpha \nu$ is the four-vector's covariant derivative projected along the local time direction, we can consider the model with a vector field Lagrangian density given by $\mathcal{L} = \mathcal{F}(|E|^2)a_0^2/16\pi G$, where \mathcal{F} is a dimensionless funtion of $|E|^2 \equiv g_{\alpha\beta}E^\alpha E^\beta$. We then minimize against the total action which contains this $\nu\Lambda$ fluid action plus the the usual Einstein-Hilbert action and the usual matter action. The equation of motion of the vector field then sets the vector field to be $\nu^\alpha \sim (1 - \Phi c^{-2}, 0, 0, 0)$ in the weak-field quasi-static limit, while the ij-cross-term of the Einstein equation requires the Newtonian potentials Φ and Ψ to be equal in the absence of anisotropic stress. The tt-term and the ii-terms of the Einstein equations can thus be combined to yield:

$$-\nabla \cdot [(1 - \mathcal{F}')(-\nabla\Phi)] - Q/2 = 4\pi G \left(\rho + \frac{P}{c^2} \right), \quad (1.35)$$

where Q is a function of $\dot{\Phi}$ and of scalar mode perturbations of the four-vector ν^α , and is negligible near collapsed quasi-static systems, as is the pressure term. The function $1 - \mathcal{F}'$ is a dielectric-like scalar free function of the covariant scalar quantity $|E| = |\nabla\Phi|/a_0$. This dielectric-like function is thus the analogue of the μ -function of MOND (Bekenstein & Milgrom 1984). To recover the MOND phenomenology, a specific choice of the function can be

$$\mathcal{F}' \equiv \frac{d\mathcal{F}}{d|E|^2} = \left(1 + \frac{|E|}{n}\right)^{-n}. \quad (1.36)$$

Zhao (2007) prefers the parameter $n \sim 3$ to best explain the amplitude of the cosmological constant. Here we rather choose $n = 1$ corresponding to the ‘simple’ μ -function of MOND (Famaey & Binney 2005, Zhao & Famaey 2006, Famaey et al. 2007b, Sanders & Noordermeer 2007). Note finally that, when a galaxy is embedded in an external field \mathbf{g}_{ext} , we have that the *total* gravitational force $-\nabla\Phi \equiv \mathbf{g}_{\text{ext}} - \nabla\Phi_{\text{int}}$, where Φ_{int} is the internal potential of the galaxy.

1.2 External Field Effects

The CDM and MOND interpretations of the galaxy kinematics can sometimes be viewed as degenerate, at the price of accepting some mysterious conspiracy between the distribution of baryons and dark matter at all radii in the CDM context (see e.g. McGaugh 2005). There are, however, some fundamental differences, one of which is the role of dynamical friction (e.g. Sánchez-Salcedo et al. 2006, Nipoti et al. 2008). Another one is the fact that the Strong Equivalence Principle is violated in MOND when considering the external field in which a system is embedded (e.g. Bekenstein & Milgrom 1984, Zhao & Tian 2006, Famaey et al. 2007a, Sánchez-Salcedo et al. 2008), even if the external field is constant and uniform. Hence, it is also important to study the effects of the environment in MOND: unlike in CDM, the rotation curves and the morphology of galaxies depend on both the background and self-gravity acceleration (Wu et al. 2007). The escape velocity at any location in a galaxy is also dependent on this external field (Famaey et al. 2007a, Wu et al. 2007). In addition to the escape and circular speeds, the influence of external fields has been studied for a variety of different situations, including the motion of probes in the inner solar system (Milgrom 2009b), the Roche lobe of binary stars (Zhao & Tian 2006), the kinetics of stars in globular clusters (Milgrom 1983c, Perets et al. 2009), and satellites

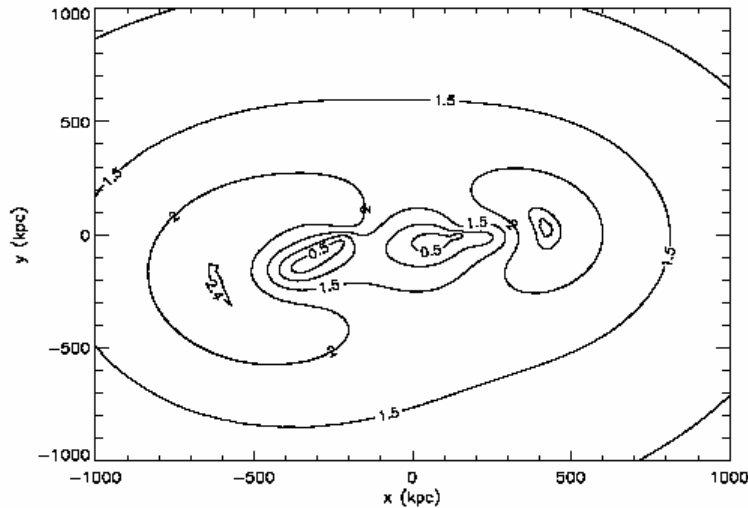


Figure 1.5: The gravity contour of the “bullet cluster” 1E0657-56, in units of a_0 .

surrounding a host galaxy (Brada & Milgrom 2000, Tirit et al. 2007, Angus 2008).

MOND-based theories generate different degrees of dark matter-like effects depending on the absolute acceleration. Most galaxies are, like the Milky Way, in the field, where they accelerate slowly with respect to the Cosmic Microwave Background, typically at a rate of $0.01a_0$ to $0.03a_0$ (Famaey et al. 2007a, Milgrom 2002, Angus & McGaugh 2008, Wu et al. 2007). For Milky Way, it is impossible to precisely calculate the value of the external field at the location of the Milky Way without describing the Local Group formation in the context of a MOND N-body simulation. Nevertheless, one can estimate its order of magnitude from the acceleration endured during a Hubble time in order to attain a peculiar velocity of 600 km s^{-1} with respect to the CMB, $g_{\text{ext}} \simeq H_0 \times 600 \text{ km s}^{-1} \simeq 0.01a_0$. The Milky Way is accelerated toward the Great Attractor, which is lying at $\sim 46 \text{ Mpc}$ far away, in the direction of the Hydra Centaurus supercluster. This value is also *roughly* the one produced by the M31 galaxy, as well as the one produced by the Virgo and Coma clusters (Famaey et al. 2007a). But in X-ray clusters, galaxies accelerate much faster, from $0.3a_0$ to $3a_0$ (Pointecouteau et al. 2005, Wu et al. 2007). We show here the gravitational acceleration contours inside the “bullet cluster” (Fig. 1.5) which represents the MONDian potential of Angus et al. (2007b).

This external gravitational field has wider and more subtle implications for the internal system in MOND than in Newton-Einstein gravity, for the very reason that MOND breaks

the Strong Equivalence Principle.

1.2.1 Binding energy of an accelerating Milky Way

Galaxies free-fall, but with slowly-changing systemic (center-of-mass) velocity $\mathbf{v}_m(t)$. Their present non-zero systemic velocity is mainly the accumulation of the acceleration by the gravity from neighbouring galaxies over a Hubble time. Consider, as a first approximation, that a galaxy is stationary in a non-inertial frame (in the Galilean sense), which free-falls with a “uniform” systemic acceleration $\dot{\mathbf{v}}_m = g_{\text{ext}}\hat{X} = cst$ due to an external linear potential, say, $-g_{\text{ext}}X$ along the X -direction, where the over-dot means time-derivatives. Let $\dot{\mathbf{v}}_{\text{int}} = (\ddot{X}, \ddot{Y}, \ddot{Z})$ be the peculiar acceleration of a star-like test particle in the coordinates relative to the center of a non-evolving galaxy internal mass density $\rho(X, Y, Z)$, then

$$\dot{\mathbf{v}}_{\text{int}} = \mathbf{g} - \dot{\mathbf{v}}_m = -\nabla\Phi_{\text{int}}(X, Y, Z), \quad (1.37)$$

where \mathbf{g} is the absolute acceleration \mathbf{g} satisfying the MOND Poisson’s equation

$$-\nabla \cdot [\mu(x)\mathbf{g}] = 4\pi G\rho(X, Y, Z), \quad x \equiv \frac{|\mathbf{g}|}{a_0}. \quad (1.38)$$

One can define an “effective potential” $\Phi_{\text{int}}(X, Y, Z)$ (called “internal” potential) and an “effective energy” $E_{\text{eff}} \equiv \frac{v_{\text{int}}^2}{2} + \Phi_{\text{int}}(X, Y, Z)$, where E_{eff} is conserved along the orbit of the test particle effectively moving in a force field $-\nabla\Phi_{\text{int}}(X, Y, Z)$, which is curl-free and time-independent because the absolute gravity \mathbf{g} is curl-free, center-of-mass acceleration $\dot{\mathbf{v}}_m$ is assumed a constant, and the galaxy density $\rho(X, Y, Z)$ is assumed time-independent.

Far away from the center of the free-falling system, we have $|\dot{\mathbf{v}}_{\text{int}}| \ll |\dot{\mathbf{v}}_m|$, hence $\mu \rightarrow \mu_m \equiv \mu(\dot{\mathbf{v}}_m/a_0) = cst$, and the equation 1.38 reads (BM1984; Milgrom1986; Zhao & Tian 2005; Zhao & Famaey 2006):

$$\nabla^2\Phi_{\text{int}} + \Delta\frac{\partial^2}{\partial X^2}\Phi_{\text{int}} \rightarrow 4\pi G\rho/\mu_m, \quad (1.39)$$

where Y, Z denote the directions perpendicular to the external field X -direction, and $\Delta = [\text{dln}\mu/\text{dln}x]_{x=|\dot{\mathbf{v}}_m|/a_0}$ is a dilation factor (note that $0 \leq \Delta \leq 1$). So at large radii where the external field dominates and the equation is linearizable, the potential satisfies

a mildly anisotropic Poisson equation and the solution at large radii² goes to

$$\Phi_{\text{int}}^{\infty}(X, Y, Z) = -\frac{GM_{\text{int}}}{\mu_m \sqrt{(1 + \Delta)(Y^2 + Z^2) + X^2 + s^2}}, \quad (1.40)$$

where we included a softening radius s , comparable to the half-light radius of a galaxy. Hence the internal potential Φ_{int} is finite, and approaches zero at large radii.

The escape speed at any location \mathbf{r} in the system can then be meaningfully defined by

$$0 = E_{\text{eff}} = \frac{v_{\text{esc}}^2(X, Y, Z)}{2} + \Phi_{\text{int}}(X, Y, Z). \quad (1.41)$$

Such escape speed is a scalar independent of "the path to escape" because the "effective energy" E_{eff} is conserved, and a particle with E_{eff} equal zero (the maximum value of Φ_{int}) will reach infinite distance from the system, and never return, hence will be lost into the MOND potential of the background (from which it cannot escape). However, equal escape speed contours across a disk galaxy are generally not axisymmetric, meaning that the escape speed differs on opposite symmetric locations of the Galaxy (Wu et al. 2007).

In summary, MOND potentials are logarithmic for isolated distributions of finite mass, and consequently infinitely deep, but that the internal potential becomes "polarized" Keplerian with a dilation factor $1 + \Delta$ at large distances (see Eq. 1.40) when an external field is applied.

1.3 Predictions of MOND

In summary, MOND has the following predictions in addition to the MONDian basis such as the Tully-Fisher relation and the Rotation Curves (Sanders & McGaugh 2002, Milgrom 2008b):

1. In a compact system with mass M , the radius scale of $r_t \equiv \sqrt{GM/a_0}$ is the transition radius between the MOND ($r > r_t$) and Newtonian ($r < r_t$) regimes. Milgrom & Sanders (2008) showed that there is an additional shell of dynamical "dark matter" at this radius.
2. The disc of High Surface Brightness galaxies (HSBs) is in the Newtonian regime, thus

²throughout the thesis, by "large radii" we mean a distance large enough to neglect the internal field $g_{\text{int}} \ll \dot{v}_m = g_{\text{ext}}$ but small enough that the external field g_{ext} can be treated as constant

the rotation curve of HSBs should decline to a quasi-Keplerian fall to the asymptotic flat constant. While for LSBs, the rotation curves rises to the final asymptotic flat constant. The rotation curves are different in LSBs and HSBs as shown in Fig. 1.6.

3. In Newtonian dynamics, pressure-supported systems are approaching isothermal and do not have a cutoff of the radius and mass. However, in MOND, isothermal systems have a truncation of mass and density at large radius following $\rho \propto r^{-4}$ (see Fig. 3.8 of §3). The hydrostatic equilibrium equation for an isotropic isothermal system is $\sigma_r^2 \frac{d\rho}{dr} = -\rho g$, where σ_r is radial velocity dispersion, and in the outer region where $g = \sqrt{GMa_0}/r$, the density decreases fast, one has

$$\begin{aligned} \sigma_r^2 \frac{d\rho}{dr} &= -\rho \sqrt{GM(r)a_0}/r, \\ \Rightarrow \sigma_r^2 d \ln \rho &= -\sqrt{GM(r)a_0} d \ln r. \end{aligned}$$

Since in outer region $M(r) = M = \text{constant}$, one can easily have

$$\sigma_r^4 = GMa_0 \left(\frac{d \ln(\rho)}{d \ln(r)} \right)^{-2}. \quad (1.42)$$

The $M-\sigma$ relation (Eq.1.42) predicts that when σ_r is in the range of $100-300 \text{ km s}^{-1}$, the mass of system should be on the order of galaxy mass.

4. The effective radius of an isothermal system is $r_e \approx r_t$. Inside this radius the MONDian effect is truncated. This implies that inside this radius the surface density is a constant, σ_m . This is a universal scale of the baryonic gravity at the edge of the dark matter core in galaxies (Gentile et al. 2009, Milgrom 2009c), since MOND can be considered as an effective dark matter theory. In this scale (the so called core radii of dark matter halos r_e) the surface density of baryons is also a constant, which implies a strong correlation between the surface density of baryons and dark matter inside r_e . The observations confirm this prediction (Gentile et al. 2009).
5. Predictions of external field effects, discussed in §1.2.
6. Predictions of negative phantom dark matter where external and internal fields are comparable, more details are discussed in §2.2.2.

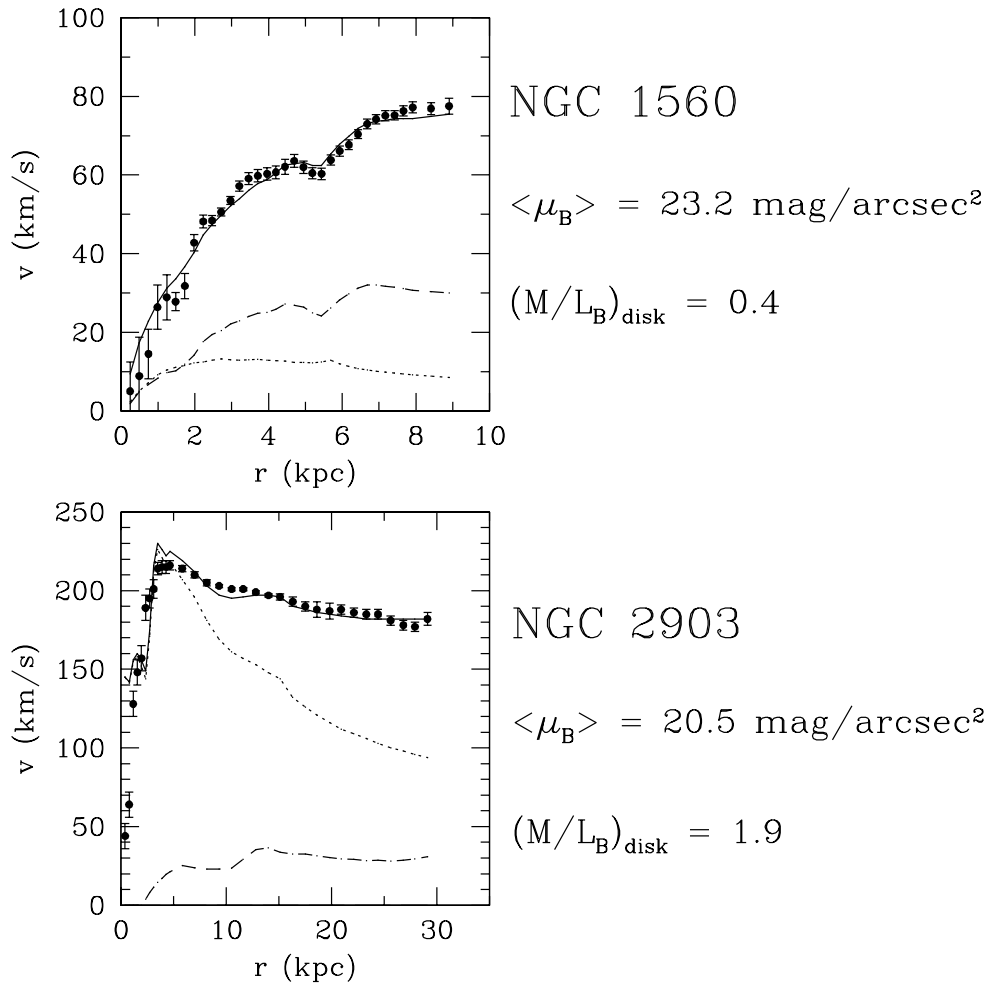


Figure 1.6: Different shapes of rotation curves of LSB(NGC1560) and HSB (NGC2903) galaxies: Keplerian velocity falls in strong gravity and rises to flat constant in weak gravity. The points are 21-cm line circular velocities. The line types are : MOND fitting (solid line), Newtonian fitting for stars (dotted), gas component (dashed) and bulge (long-dashed). Horizontal axis is radius in unit of kpc, and vertical axis is circular velocities in unit of km s^{-1} . (Sanders & McGaugh 2002)

The thesis is organized as follows: In §1, we briefly reviewed the basic idea and recent developments of MOND. In §2.1 we shall study stability of galaxies embedded in the external fields and the escape speeds of those galaxies in the framework of MOND. As an application, we shall compare the escape speeds of the Large Magellanic Cloud (LMC) in the frameworks of MOND and CDM in §2.2 and the effective dark matter effects in the external fields in §A. We shall briefly review the method of Schwarzschild in §3, and apply the technique to construct the first MONDian isolated galaxy, and test the stability and evolution of the obtained systems by N-body simulations. Finally, in §4 we shall apply the Schwarzschild's technique to construct galaxies embedded in a uniform external field and study their stability and evolution by N-body simulations.

2

External Fields and Escape Speeds

In §1.2 we generally discussed about the External Field Effects (EFE) in MOND that: The external field makes the potential well shallower and enables stars to escape from self-bound systems. Thus an essential question arises: can systems be kept stable in the presence of an external field?

To study the stability of the MONDian galaxies, in §2.1, we *numerically* solve the MOND Poisson equation for systems embedded in several different environments, ranging from the field to galaxy clusters, and show that

1. for the Milky way (embedded in a weak gravitational field), the local escape speed is numerically compatible with the observations as analytically predicted in (Famaey et al. 2007a),
2. rotation curves of Milky Way-like galaxies would have a Keplerian falloff when residing close to the center of clusters while there is no falloff in field galaxies,

3. usual Low Surface Brightness discs should not exist in clusters in MOND.

The new observations by Kallivayalil et al. (2006a,b) showed that the 3D velocity of the LMC is up to $\sim 378 \text{ km s}^{-1} \pm 18 \text{ km s}^{-1}$, which is larger than the escape speed in the CDM model of the Milky Way. Can MOND explain the high 3D velocity of the LMC? Is the Large Magellanic Cloud (LMC) bound to the Milky Way?

In §2.2 we further describe the Milky Way with different CDM-based models, and compare them with the MOND framework with a small external field. We then calculate numerically the circular and escape velocities from the Galaxy as a function of position in both MOND and CDM models. We show that

1. among models fitting the observed rotation curve MOND predicts deeper potentials than CDM at large radii ($r > 50 \text{ kpc}$). As a matter of fact, with the newly-measured value of the 3D velocity, the LMC is barely bound at the one-sigma level in our four CDM models. If the LMC is unbound, it leads to difficulty on the formation of the Magellanic Stream.
2. MOND is equivalent to an effective phantom dark matter density, but this density can become negative in a fat disc perpendicular to the external field. The profile of the fat disc on the $x - z$ plane of the Milky Way has a cone-shape. The peak of the cone is at the saddle point where external field cancels internal field (Fig. 2.5, also see Milgrom 1986). A negative convergence parameter could thus in principle be observed in the gravitational lensing generated by Milky Way-like galaxies.

2.1 Loss of Mass and Stability of Galaxies in MODified Newtonian Dynamics

The self-binding energy and stability of a galaxy in MOND-based gravity are curiously decreasing functions of its center of mass acceleration of $10^{-12} - 10^{-10} \text{ m/s}^2$ towards neighbouring mass concentrations. A tentative indication of this breaking of the Strong Equivalence Principle in field galaxies is the RAVE-observed escape speed ($550 \pm 50 \text{ km s}^{-1}$) in the Milky Way. But the consequences of an environment-sensitive gravity are severe in clusters, where member galaxies accelerate fast: no more do we expect to find a dark halo-like potential to support galaxies, especially extended axisymmetric discs of gas and stars

with flat or rising circular velocity curve. This predicted “disappearance of stereotype galaxies” makes MOND falsifiable with targeted surveys.

Hereafter, we *numerically* solve Eq. 1.38 using the MOND Poisson solver developed by the Bologna group (Ciotti et al. 2006); the results based on spherical grids are also confirmed with the cartesian grid-based code of the Paris group (Tiret & Combes 2007) with very different spatial resolutions. In order to solve the modified Poisson equation 1.38, they mapped the infinite radial coordinate in a spherical grid:

$$r(\beta) = \tan^\alpha \beta, \quad (0 \leq \beta < \pi/2), \quad (2.1)$$

where α can be chosen 1 or 2. Thus they mapped the infinity radial grid on the the finite interval, ranging in $[0, \pi/2)$. The partial differential operator $\frac{\partial}{\partial r} = \frac{\cos^2 \beta}{\alpha \tan^{\alpha-1} \beta} \frac{\partial}{\partial \theta}$, and the boundary conditions are exact boundary conditions

$$\Phi_{r \rightarrow \infty} \rightarrow 0, \quad (2.2)$$

$$\nabla \Phi_{r \rightarrow \infty} \rightarrow 0 \quad (2.3)$$

at infinity where $\beta = \pi/2$. In our simulations, we include an external field. We program in the mass density of the internal system, solving the MOND Poisson equation as if it were isolated, except for requiring a boundary condition on the total gravity as

$$-\mathbf{g} \rightarrow g_{\text{ext}} \hat{\mathbf{X}} - \nabla \Phi_{\text{int}}^\infty(X, Y, Z) \quad (2.4)$$

on the last grid point (X, Y, Z) . The external field is along the X direction. The internal gravity at infinity derived from the internal potential (i.e., Eq. 1.40) is proportional to $1/r'$, where $r' = \sqrt{(1 + \Delta)(Y^2 + Z^2) + X^2}$ is the elliptical radius with the dilation factor Δ defined in §1.2.1. Hence the consideration of $-\nabla \Phi_{\text{int}}^\infty(X, Y, Z) \rightarrow 0$ is reasonable. And the total gravity at the boundary equals to the external gravity.

Note finally that in our models hereafter, we use the parametric μ -function $\mu(x) = x/(1 + x)$, which fits extremely well the rotation curve of the Milky Way (Famaey & Binney 2005), as well as external galaxies (Famaey et al. 2007b, Sanders & Noordermeer 2007).

2.1.1 Models for HSBs and LSBs

Milky Way model as HSB galaxy

We use the Besançon Milky Way Model (Robin et al. 2003) to simulate High Surface Brightness (HSB) galaxies. This model is a realistic representation of the Galaxy, explaining currently available observations of different types (photometry, astrometry, spectroscopy) at different wavelengths. The stellar populations included in the model are: a thin disc made of seven isothermal layers each having a different age between 0.1 and 10 Gyr; an 11-Gyr-old thick disc with a modified exponential density law, a spheroid with a power law density, slightly flattened, a prolate old bulge modeled by a triaxial density law. We remove the dark matter halo for our simulations. We then apply the MOND Poisson solver using $512 \times 64 \times 128$ grid points where the grid points in the radial direction are chosen as $r_i = 50.0 \tan \left[(i + 0.5) \frac{0.5\pi}{512+1} \right]$ kpc.

As a first application, the RAVE solar neighborhood escape speed 544_{-46}^{+64} km/s is well-reproduced by our fully numerical model galaxy (Fig. 2.1 for a typical external field of $0.01a_0$), as analytically anticipated in (Famaey et al. 2007a). When the direction of the external gravity changes, the escape speed varies in a narrow range $[545, 558]$ km s⁻¹ in the solar neighborhood.

NGC1560 density model as LSB galaxy

We also model NGC 1560, which is a benchmark Low Surface Brightness (LSB) disc galaxy (Broeils 1992). We use an exponential stellar disc of $1.97 \times 10^8 M_\odot$ and a multi-Gaussian gaseous component of $1.07 \times 10^9 M_\odot$ to match the observed baryon distribution (Broeils 1992):

$$\rho_* = \frac{\sigma_{*0}}{2z_{*0}} \exp \left[-\left(\frac{R}{R_0} + \frac{|z|}{z_{*0}} \right) \right], \quad (2.5)$$

$$\rho_{gas} = \Sigma_{gas0} \cdot \sum_{i=1}^7 a_i \exp \left[-\frac{(R - R_i)^2}{2\sigma_i^2} \right] \exp \left(-\frac{z^2}{2z_0^2} \right), \quad (2.6)$$

where $R_0 = 1.3$ kpc is the scale-length, $z_{*0} = 0.18$ kpc is the scale-height for the stellar component, and $\Sigma_{gas0} = 6.158 M_\odot pc^{-2}$ is the central projected surface density of NGC1560. R_i are the central radii of the Gaussians and a_i are normalization constants for fitting observational projected surface density data (Table 2.1), and $z_0 = 0.69$ kpc for

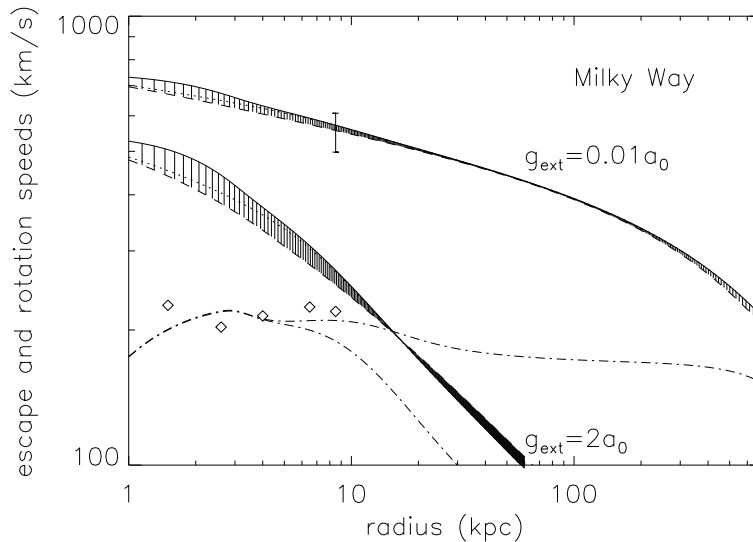


Figure 2.1: Model of a Milky Way-like galaxy in weak ($0.01a_0$) and strong ($2a_0$) external fields. Escape speeds in the disc plane for various field directions (solid and dotted) are compared with the error bar for the local escape speed measured from the RAVE survey (Smith et al. 2007). The predicted circular speed curves (dot-dashed lines) are also compared with data (diamonds) (Caldwell & Ostriker 1981).

the gas component.

A MOND Poisson solver (Ciotti et al. 2006) with $256 \times 64 \times 64$ grid points is applied, the radial grid being $r_i = 10.0 \tan \left[(i + 0.5) \frac{0.5\pi}{256+1} \right]$ kpc. Again it is found that an external acceleration of $0.01a_0$ is compatible with the rotation curve of NGC1560, which is not in a cluster environment (Fig. 2.2).

2.1.2 Fast-accelerating galaxies in clusters

Now consider boosting the Milky Way’s systemic acceleration *suddenly* to match the environment in a galaxy cluster. Fig. 2.1 shows that for an external field of $2a_0$ the escape speed of stars is strongly reduced, falling Keplerian-like $300\sqrt{5 \text{ kpc}/r} \text{ km s}^{-1}$ outside 5 kpc, where r is the half mass radius of the stars and gas of the Milky Way. All dwarf satellites of the Milky Way and the outer disc rotating with 200km/s would become unbound.

In fact, the instantaneous hypothetical circular speed must also be lowered by the sudden boost of acceleration and the outer galaxy should then exhibit a Keplerian falling rotation curve (Fig. 2.1). Outer disc stars and gas should enter the elliptical or parabolic orbits of the same angular momentum if allowed to respond to a suddenly reduced gravity, and precess with a preferred direction of instantaneous systemic acceleration which thick-

Table 2.1: Parameters of density model of NGC1560

i	1	2	3	4	5	6	7
$a_i(M_\odot \text{ pc}^{-1})$	11.0	1.2	8.6	4.6	2.0	1.9	1.4
$R_i(kpc)$	0.0	1.0	1.97	3.7	5.3	6.0	7.0
$\sigma_i(kpc)$	1.5	0.2	0.8	0.95	0.3	0.4	2.0

ens the disc. In any case, observing asymptotically flat rotation curves for purely baryonic Milky Way-like galaxies residing in such environments would falsify MOND. A galaxy of the same luminosity would have lower velocities, consistent with the observed trend with cluster Tully-Fisher relation (Sanders & McGaugh 2002).

Now consider suddenly boosting the acceleration of our benchmark LSB galaxy to $\dot{v}_m = 0.3a_0$ or $\dot{v}_m = 2a_0$ (typical of the outer and inner parts of galaxy clusters. The real orbit of a member galaxy would pass both regions at apocenter and pericenter respectively).

The circular speed (Fig. 2.2 lowest dot-dashed curve) of a fast-accelerating LSB is significantly reduced. We see that all previous disrupting effects are even more severe on a LSB galaxy with the escape speed falling to as low as 50 km/s. Outer stars with original circular speed 50 – 80 km/s would enter parabolic orbits, and inner stars move outwards on severely elongated non-planar orbits. Actually, the dynamics resembles a purely Newtonian disc without a round stabilizing dark halo, indicating that the galaxy would become extremely bar-unstable (Mihos et al. 1997). Such a LSB would lose its MOND support and would be subject to strong distortions, even before the traditional tidal effect becomes important.

2.1.3 Conclusion and discussion

The external field effect is a generic prediction of the modified gravity theory of (Bekenstein & Milgrom 1984, Zlosnik et al. 2007b) with a preferred frame. This effect is helpful for high velocity stars to escape from the Milky Way-like field galaxies. On the other hand, the internal dynamical structure of a field galaxy would transform when entering a cluster. Such relations of field galaxies as the asymptotic flat rotation curves, Tully-Fisher relation, galaxy luminosity functions, and Hubble type distribution are expected to be modified strongly in clusters. The effects are most destructive for classical the LSB galaxies; curiously their field counterparts have been a legendary success for MOND in terms of well-fitted rotation curves.

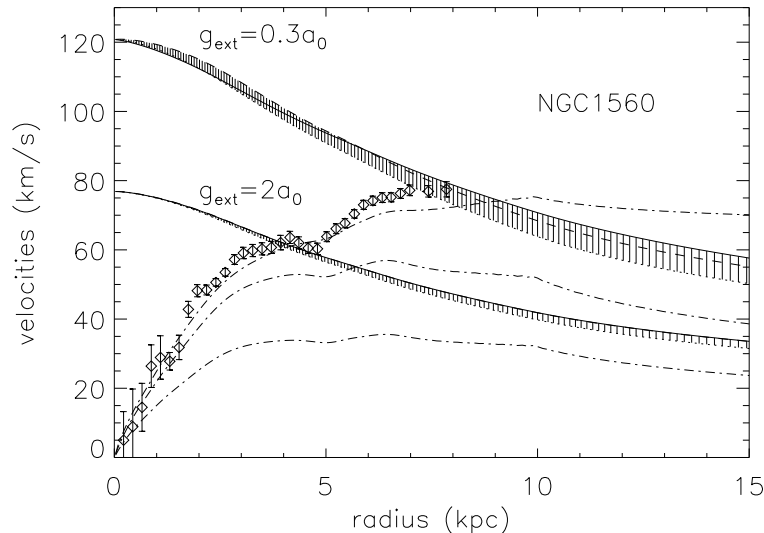


Figure 2.2: Similar to Fig.2.1, but for models of a NGC 1560-like LSB galaxy. Circular speed curves for $g_{\text{ext}} = 0$ (no escape), $g_{\text{ext}} = 0.3a_0$ (middle) and $g_{\text{ext}} = 2a_0$ (bottom) are compared with the observed rotation curve of NGC 1560.

We thus argue that it would be extremely valuable to analyse the kinematics of a *sample* of HSB galaxies and search for LSB galaxies in nearby clusters using deep HI surveys. The study of a sample of galaxies would be needed because of the uncertainty of the determination of the real distance (as opposed to projected distance) of a galaxy from the cluster center. An obvious difficulty will be that cluster galaxies are HI-deficient (Solanes et al. 2001). An example of such an HI database is the VIVA survey (VLA Imaging of Virgo in Atomic Gas (Chung et al. 2007)). We also predict that a future detection of any un-distorted HSB late type disc galaxy near the center of a galaxy cluster would be extremely surprising in the context of MOND. A null-detection of thin LSB discs is predicted in clusters because they most probably have been turned into gas-poor dwarf ellipticals if not fully disrupted. The low surface density gas in galaxies also suffers ram pressure stripping while moving in the gaseous clusters; gas is easily stripped in the reduced MONDian internal gravity, further reducing the available mass for self-gravity.

Surely similar effects happen in the context of cored Dark Halos. Some simulations show that the LSB discs and dwarf irregulars get harassed (Moore 1999) and transformed into dwarf ellipticals or ultra-compact dwarf ellipticals (Evstigneeva et al. 2007, Cortese et al. 2007) in the densest part of the cluster coinciding with the region where the external field is the highest. To our knowledge, the properties of cluster disc galaxies (such as their

Tully-Fisher relation) have not been extensively simulated. The important assumption of the existing simulations is a large core for the CDM halo of the LSB; the harassment becomes much less effective if the cluster member LSB starts with a dense CDM cusp density (Lucio Mayer 2007, private communications).

As for the gas-poor non-rotating dwarf spheroidals (e.g., Sextans), they are expected to have a central CDM density of $\sim 0.1M_{\odot} \text{pc}^{-3}$, a factor of 100 denser than the galaxy cluster, hence might survive the tidal harassment in CDM. In MOND, if a spheroidal of $M = 2 \times 10^5 M_{\odot}$ and half mass radius of $s \sim 500 \text{pc}$ is suddenly introduced inside a galaxy cluster, it would have a central binding energy of only $\sim \frac{GM}{s}(1 + \Delta)^{-2/3} \mu_m^{-1} \sim (5 \text{ km s}^{-1})^2$, much less than its initial internal random motion energy $\frac{3 \times (10 \text{ km s}^{-1})^2}{2}$, and hence is quickly dispersed (perhaps anisotropically). The symbols are defined in §1.2.1: M is mass, $\mu_m \equiv \mu(\dot{\mathbf{v}}_m/a_0) = \text{cst}$, and $\Delta = [\text{dln}\mu/\text{dln}x]_{x=|\dot{v}_m|/a_0}$ is a dilation factor of the internal potential.¹ In short, any discovery of a sample of classical LSB galaxies in clusters would favor cuspy CDM, and falsify MOND or cored Dark Halos.

Tidal harassment effects exist in MOND as well. In addition, the cluster galaxies are double-whammed (even more important) by the external field effect. An even more curious distortion on the MONDian LSB or HSB disc happens when the disc is mis-aligned by an angle θ_m with the instantaneous direction of the external field, which generally changes amplitude and direction along the orbit of a LSB on time scales of 0.2-1Gyr. The elliptical potential of Eq. 1.41 creates a differential force with a component normal to the disc, hence a specific torque $-\mathbf{r} \times \nabla\Phi$. This causes differential precession of the disc angular momentum vector with an angular speed proportional to $\mu_m^{-1} \sqrt{GM/r^3} \Delta \sin(2\theta_m)$; an LSB disc is likely shredded by one precession and a HSB disc is thickened. The *precession, asymmetric dilation and reduction of inner circular velocity curves* (cf. Fig. 2.2) are confirmed by N-body simulations using the code of the Paris group (Tiret & Combes 2007) in MOND, but are generally forbidden by Newtonian laws in the Dark Matter framework.

¹For similar reasons open clusters in the solar neighbourhood are predicted to be unbound in MOND.

2.2 Milky Way potentials in cold dark matter and MOdified Newtonian Dynamics - Is the Large Magellanic Cloud on a bound orbit?

The classical problem of modelling the mass distribution and the corresponding gravitational potential of our Galaxy carries with it the key to our understanding of the elusive dark matter. Nowadays, the dominant paradigm is that dark matter is actually made of non-baryonic weakly interacting massive particles, the so-called cold dark matter (CDM). Many models of the Milky Way have been devised in this context (e.g. Wilkinson & Evans 1999, Olling & Merrifield 2001, Klypin et al. 2002).

In this section, we model the Milky Way with different CDM-based models, and compare them with the MOND framework, allowing for various values of the external field. We show that while the CDM models have a spherical potential in the outer regions of the Galaxy ($r > 50$ kpc), the MOND potential is more ellipsoidal. We then also numerically calculate the circular and escape velocities from the Galaxy as a function of position in both MOND and CDM models. This could be useful in comparing with future data from planned or already-underway kinematic surveys (RAVE, SDSS, SEGUE, SIM, GAIA or the hypervelocity stars survey). In addition, we finally apply this to the case of the large Magellanic cloud (LMC) in order to see which models allow it to be bound to the Milky Way. We conclude that, in MOND, an external field of less than $0.03a_0$ is needed, an upper limit strikingly similar to that needed to explain the local escape speed from the solar neighbourhood (see §2.1 and Famaey et al. 2007a, Wu et al. 2007).

2.2.1 Potential of the Milky Way

MOND

We model the Milky Way in MOND following §2.1, where the Besançon baryons model (Robin et al. 2003) is used. This model contains a thin stellar disc with mass of $2.15 \times 10^{10} M_\odot$, a thick stellar disc of $3.91 \times 10^9 M_\odot$, a bar/bulge of $2.03 \times 10^{10} M_\odot$, an interstellar gaseous matter component of $4.95 \times 10^9 M_\odot$, and a stellar halo of $2.64 \times 10^8 M_\odot$. We first choose an external field $g_{\text{ext}} = 0.01a_0$: this is presumably due to the local gravitational attraction of Large Scale Structure, and mainly from the so-called Great Attractor region

(see Radburn-Smith et al. 2006 in the Sun-Galactic Centre direction. We then let the external field vary, in order to investigate the effect of its value on the MOND model. Indeed, the effect of M31, and of the Coma and Virgo clusters, makes the value of the external field extremely uncertain. For instance, the baryonic mass of M31 is estimated to lie between $7 \times 10^{10} M_{\odot}$ and $2 \times 10^{11} M_{\odot}$ (Seigar et al. 2008, Tempel et al. 2007, Geehan et al. 2006, Carignan et al. 2006), and sits at 800 kpc from the Milky Way center, thus exerting an external field in the range $0.01a_0 - 0.02a_0$, a value roughly similar to the one exerted by Large Scale Structure. Note however that the external field from M31 is a varying one, and that if one *only* considered the external field from M31, no star could ever escape from the MW-M31 system because the external field from M31 would *never* dominate over the internal one from the MW in the direction opposite to M31. A star from the solar neighbourhood leaving in this direction would thus never escape in this direction. However, it could bounce back in and escape in the other direction, falling into the potential well of M31, if its speed is larger than the escape speed in the other direction: this is why the external field from Large Scale Structure is also important. In any case, we consider hereafter the external field as a parameter that can be constrained by data (such as the proper motion of the LMC, see Sect. 5.2).

Once the external field is chosen, we solve for the internal gravitational acceleration, $-\nabla\Phi_{\text{int}}$, the modified Poisson equation of MOND (see also Eq. 1.35) Eq. 1.38. As stated above, we choose the ‘simple’ μ -function of the form $\mu(x) = x/(1+x)$ (i.e., Eq. 1.9), corresponding to $n = 1$ in Eq. 1.36. We use the Poisson solver developed by the Bologna group (Ciotti et al. 2006) with $512 \times 64 \times 128$ grid points, the radial grid points being $r_i = 50.0 \tan [(i + 0.5)0.5\pi/512 + 1]$ kpc. Notice that, even though it has fewer degrees of freedom than the CDM models presented hereafter, the MOND model has, contrary to common wisdom, some freedom: the choice of the μ -function could have been different, the value of a_0 has an error bar that we ignored here, the mass-to-light ratio of the stellar component can vary, the presence of unseen baryons can have a big influence (see Sect. 5.4), and the value of the external field is not known a priori.

We note that, in such a MOND model, the escape velocity v_{esc} of a test particle at an arbitrary position (x, y, z) can be defined as Eq. 1.41. This means that for a zero effective internal energy of the particle ($E_{\text{eff}} = 0$), it can escape from the internal system and never return.

Table 2.2: NFW Profile Parameters for Milky Way

<i>NFW</i>	<i>c</i>	$M_{vir}(10^{12}M_{\odot})$	$r_{vir}(\text{kpc})$	δ_{th}	$H_0(\text{km s}^{-1} \text{Mpc}^{-1})$	Ω_0	$r_{\odot}(\text{kpc})$
<i>KZSB1</i>	12	1.0	258	340	70	0.3	8.5
<i>RAVE1</i>	24.3	1.89	257	340	65	0.3	7.5

CDM

We now compare the MOND model described above with various CDM models of the Galaxy. Unfortunately, CDM-based models are far from unique. Nevertheless, we limit ourselves to four models: two based on the work of Klypin et al. (2002, hereafter KZS), and two based on the recent work of the RAVE collaboration on the local escape speed from the Solar Neighbourhood (Smith et al. 2007).

First we explore the model labelled B1 in KZS, composed of a double-exponential disc for the baryons and a NFW profile (Navarro et al. 1997) for the dark matter halo. We then explore another model in which we replace the KZS baryons with the Besançon model, but use the same CDM component as in KZS B1. We call this second model the Bsc CDM model.

The NFW profile is the most widely used CDM-halo model, it is described as (Navarro et al. 1997):

$$\rho_{halo}(r) = \frac{\rho_s}{x(1+x)^2}, x = r/r_s, \quad (2.7)$$

$$M_{vir} = \frac{4\pi}{3}\rho_{cr}\Omega_0\delta_{th}r_s^3c^3, \quad (2.8)$$

$$\rho_s = \frac{\rho_{cr}\Omega_0\delta_{th}}{3} \frac{c^3}{\ln(1+c) - \frac{c}{(1+c)}}. \quad (2.9)$$

Where ρ_s is the characteristic density parameter, r_s is the radius parameter, $\rho_{cr} = 3H_0^2/8\pi G$ is the critical density of the Universe determined by the Hubble constant at redshift $z = 0$, Ω_0 is the fraction of matter (including baryons and dark matter) to the critical density, δ_{th} is the critical overdensity of the virialized system, and c is the concentration parameter. In the inner part of the dark halo, $\rho_{halo} \propto r^{-1}$ and in the outer part $\rho_{halo} \propto r^{-3}$.

The NFW profile parameters of the KZS B1 model are listed in Table 2.2. Both angular

momentum exchange between the baryons and dark matter and adiabatic contraction are considered. The angular momentum of baryons is lost and deposited into the dark halo, hence the centre of the dark halo becomes more scattered. During the evolution of the galaxy, the fall of baryons into the galactic centre makes the gravity potential deeper, and more dark matter particles are trapped in this deeper potential well. The adiabatic contraction thus makes the dark halo become denser. These two conflicting effects have been shown to make the CDM halo approximately similar to the original NFW-profile. For baryons, the KZS B1 model has a double-exponential disc. The density of nucleus, bulge and disc are then described by ² (Kent et al. 1991, Zhao 1996):

$$\rho_b = \rho_1 + \rho_2 + \rho_3, \quad (2.10)$$

$$\rho_1 = \rho_{1,0} \left(\frac{0.36(x^2 + y^2) + z^2}{z_0^2} \right)^{-1.85/2} \exp \left(-\sqrt{\frac{0.36(x^2 + y^2) + z^2}{z_0^2}} \right), \quad (2.11)$$

$$\rho_2 = \rho_{2,0} \exp \left(-\frac{\sqrt{[(0.26x)^2 + (0.69y)^2]^2 + z^4}}{2z_0^2} \right), \quad (2.12)$$

$$\rho_3 = \rho_{3,0} \exp \left(-\frac{\sqrt{x^2 + y^2} + 12|z|}{r_d} \right) \quad (2.13)$$

where $z_0 = 0.4$ kpc, $r_d = 3$ kpc, $M_1 + M_2 = 1 \times 10^{10} M_\odot$, $M_1/(M_1 + M_2) = 0.15$, $M_3 = 5 \times 10^{10} M_\odot$, and $\rho_{1,0}, \rho_{2,0}, \rho_{3,0}$ are characteristic parameters for the density required in order to reproduce the bar/bulge from COBE, and the disc of Kent et al. (1991). The three densities ρ_1, ρ_2, ρ_3 are convenient for describing the global shape of the Galaxy rather than real separate components of the MW. This is why we also set up the Bsc model as explained above.

As we aim to predict the escape velocity as a function of position, we explore additional models used by the RAVE collaboration to reproduce the local escape velocity from the Solar Neighbourhood (Smith et al. 2007). We choose two of their models, the uncontracted NFW (RAVE 1) and the Wilkinson-Evans (WE) profile (RAVE 3) for the dark halo.

Model RAVE 1 is described by the combination of a NFW halo (Parameters in Table 1), a baryonic disc with a Hernquist bulge of $1.5 \times 10^{10} M_\odot$ and a scale radius of 0.6 kpc, and a Miyamoto-Nagai disc of $5.0 \times 10^{10} M_\odot$ with scale height 0.3 kpc and scale length of 4 kpc.

²Eq. 6 of KZS had a typo

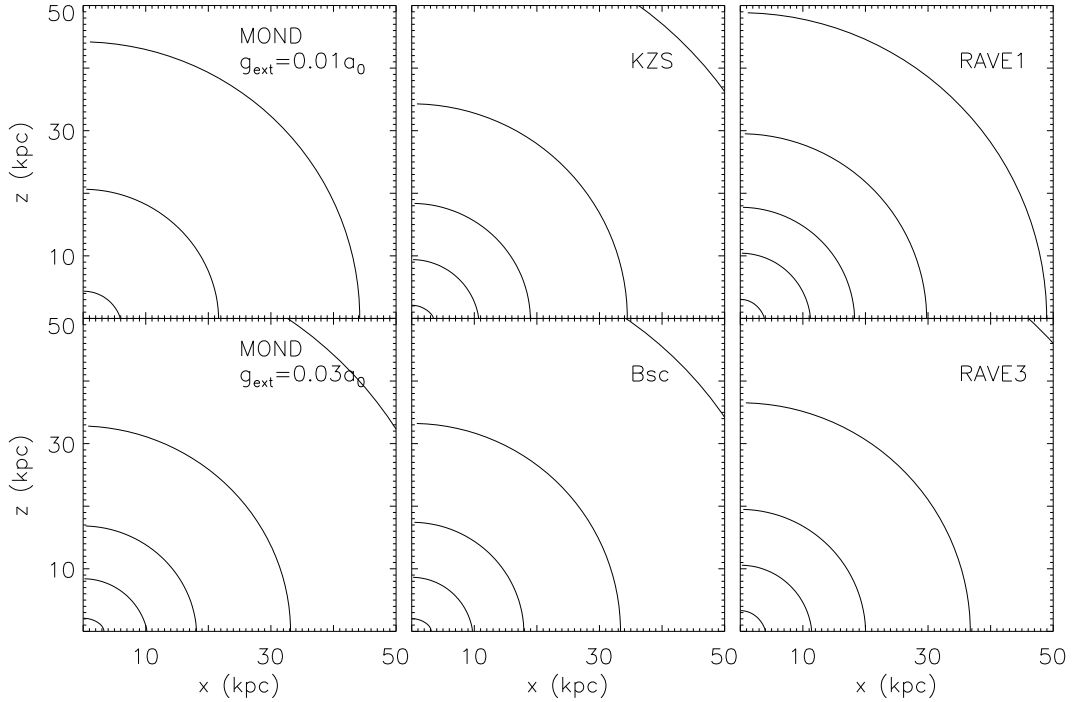


Figure 2.3: Isopotentials on the $x - z$ plane. The x -axis is sun-the centre direction and the z -axis is perpendicular to the disc plane. The isopotentials correspond to escape velocities of 600 km/s, 500 km/s, 450 km/s, 400 km/s and 350 km/s (starting from 600 km/s in the center).

In the RAVE 3 model the dark matter halo density profile is more cuspy in the centre, $\rho \sim r^{-2}$, and has a cut-off in the density distribution at the outer parts of the Galaxy, $\rho \sim r^{-5}$. The halo density is given by (Wilkinson & Evans 1999):

$$\rho(r) = \frac{M}{4\pi} \frac{a_s^2}{r^2(r^2 + a_s^2)^{3/2}}, \quad (2.14)$$

where $M = 1.89 \times 10^{12} M_\odot$ is the total mass of the halo, and $a_s = 314$ kpc. This profile keeps the rotation curve approximately flat up to the radius a_s .

2.2.2 Axis ratios and Phantom dark matter

To investigate the intrinsic differences between the MOND and CDM potentials, we compute and plot the isopotential contours of the MOND model with an external field of $0.01a_0$ and $0.03a_0$, and similar contours of the four CDM models on Fig 2.3. The MOND potential always yields slightly more ellipsoidal (oblate) isopotential contours. This is mainly because the MOND potential is produced by baryons and the flattened/non-axisymmetric density distribution of the disc/bar in the Besançon model dominates the shape of the

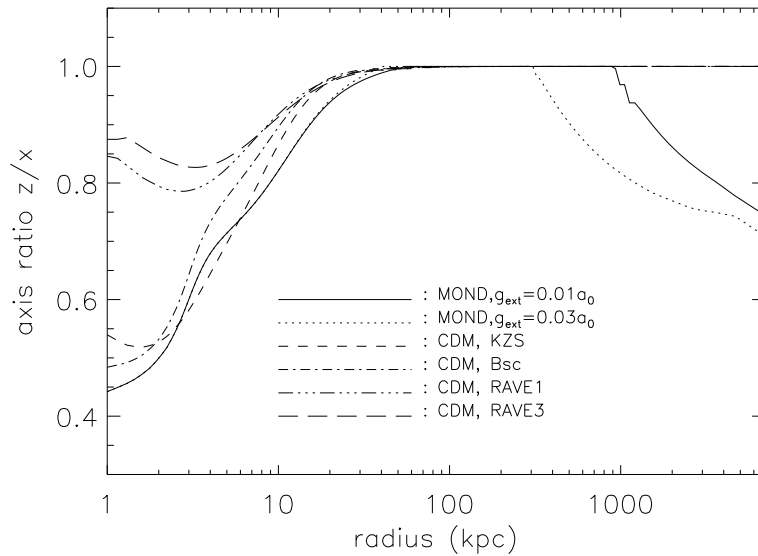


Figure 2.4: $z - x$ potential axis ratio. The x -direction is the galactic centre to sun direction, and z is perpendicular to the disc plane. The predictions for $r > 500$ kpc are only qualitative because they should be perturbed by variations of the external field and covariant corrections.

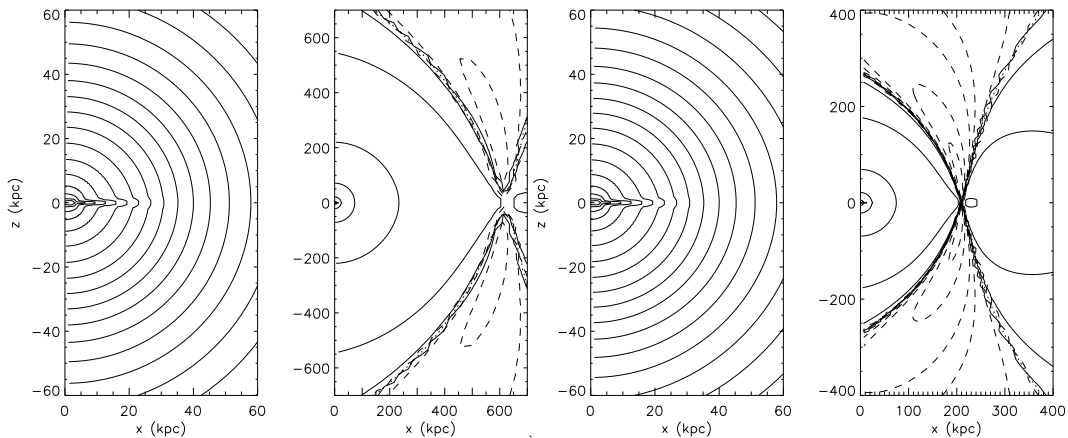


Figure 2.5: Isodensity of phantom dark matter in a MOND Milky Way embedded in an external field of $0.01a_0$ (panels a and b) and $0.03a_0$ (panels c and d). The panels a and c are on Galactic scale, and they show a disc-like distribution of the phantom dark matter inside 20 kpc. The panels b and d are on larger scale of several hundreds of kpc. The solid and dashed contours are isodensity for positive and negative density respectively, and the dotted line is the watershed with zero-density.

potential at small radii. Moreover, we note that when an external field is applied in a random direction (here it has been applied in the x -direction), even an axisymmetric baryonic density distribution yields a triaxial/non-axisymmetric potential³. Here, the external field in the x -direction actually makes the MOND potential oblate again at very large radii (see Eq. 1.40) asymptoting to a $z - x$ axis ratio of 0.7 at infinity (see Fig. 2.4). The MOND potentials have thus a flattened oblate shape at the very edge of the Galaxy too. Note that our predictions at large radii ($r > 500$ kpc) on Fig. 2.4 are only qualitative since the MOND potential at extremely large radii can of course become dominated by other local structures in certain directions, and there can also be variations of the Large Scale Structure-external field on scales larger than 1000 kpc. Here, we only considered a constant external field. In the CDM models the situation is slightly different: the potential becomes spherical quite quickly as the radius increases (since it is dominated by the spherical profile of dark matter). All the CDM models have a larger $z - x$ axis ratio than the MOND ones when $r > 5$ kpc. This is due only to the flattened baryonic distribution in MOND, and not to the external field effect, which becomes effective in this context only at very large radii ($r \sim 200$ kpc in the case of a $0.03a_0$ external field, see Fig. 2.4). Of course, assuming some flattening of the CDM halo could also yield a more oblate or more prolate CDM potential (Jing & Suto 2002, Bailin & Steinmetz 2005, Allgood et al. 2006, Macciò et al. 2007), again adding to the high degree of freedom in CDM models. The MOND prediction is much more constrained.

To investigate further the intrinsic differences between the MOND and dark matter models, it is useful to think of MOND in dark matter terms. Once the MOND potential is known, one can use the Newtonian Poisson equation to derive the corresponding density of matter that would be needed in the Newtonian context. Then, subtracting the visible matter, one obtains the “virtual” dark matter, or “phantom dark matter” distribution predicted by MOND. We now take the liberty to interpret this internal potential Φ_{int} within the context of Newtonian gravity

$$\nabla^2 \Phi_{\text{int}} = 4\pi G(\rho + \rho_{\text{PDM}}), \quad (2.15)$$

where the $(\rho + \rho_{\text{PDM}})$ is the total dynamical mass of the system, and ρ_{PDM} is the so called “phantom dark matter” (hereafter PDM), which can be held responsible for the “extra

³This inherent triaxiality of the internal potential in MOND is also mentioned in Wang et al. (2008)

gravity beyond the baryonic matter”. This is plotted on Fig. 2.5: clearly one sees that at small radii, the phantom dark matter tracks the baryons and effectively creates a dark matter disk (see also Nipoti et al. 2007c). Moreover, fat discs of *negative* phantom dark matter densities perpendicular to the external field direction are predicted at large radii, when the internal and external gravitational fields are of the same order of magnitude (see also Milgrom 1986). The profiles of these fat discs on the $x - z$ plane is very similar to the profiles of cones. The peaks of the cones sit at the saddle point where the external field cancels the internal field. That is one of the most important differences between MOND and CDM, since CDM of course never predicts negative mass densities. Note that this is very different from a simple change of the direction of the force felt by a test particle: here, it really means that the *divergence* of the force field can be locally positive, or that the flux of the force field through an infinitesimal volume is locally positive. In standard gravity, the divergence of the force field is zero outside of matter and is always negative inside the matter, through the Poisson equation. A locally positive divergence of the force field is thus inconceivable in standard gravity without resorting to negative dark matter. For $g_{\text{ext}} = 0.01a_0$, the negative phantom dark matter region is around $r = 600$ kpc while for $g_{\text{ext}} = 0.03a_0$ it is around $r = 200$ kpc. Let us however note once again that the situation here is quite idealised since we only took into account a constant external field. The varying external field of M31 and the LMC could create other pockets of negative phantom densities not seen here. Moreover there could also be significant covariant corrections to MOND (cf. Q in Eq. 1.35), and variations of the LSS-external field, on scales larger than 1000 kpc, where the predictions should thus be treated as qualitative only. We cannot observe such negative dark matter effects through satellite orbits, since the global shape of the MOND potential keeps the gravity tightly fitting the observations. However indeed MOND and CDM predict different shapes of Milky Way potential, which can be confirmed by further study on the satellite orbits. One of the more directly related quantities is the gravitational lensing. Since the potentials of galaxies not only constrains the motion of stars, but also the distant photons. The convergence of gravitational lensing κ is proportional to the projected dynamical density in Einstein’s theory. Therefore one would naturally consider about whether the weak gravitational lensing is influenced by the projected density of the ‘phantom dark matter’. In covariant MOND theories such as TeVeS (Bekenstein 2004b) and the $\nu\mathbf{A}$ formulation (Zhao 2007, Halle et al. 2008), lensing has been shown to work

exactly as in General Relativity, notably for the relation between the potential and the convergence. The only difference lies in the relation between the potential and the true underlying matter density (see Bekenstein 2004b, Zhao 2007; and Angus et al. 2007b for an application). This means that, if interpreting the MOND potential in terms of dark matter as an observer believing to live in a CDM Universe would do, the phantom surface density can directly be translated into convergence: the projected negative dark matter density would thus produce a negative convergence κ . If we placed the Milky Way far away, say $z = 0.3$, then we could in principle observe the negative κ ; we estimate it to be of the order of

$$-\kappa \sim 0.01 \frac{1000 \text{ kpc}}{R}. \quad (2.16)$$

It is not impossible to detect such an amplitude by weak lensing observations. The statistics results should be different with the other cosmological models which do not produce negative κ . In Feix et al. (2008b) they simulated the MONDian weak lensing for an ideal cylindrical filament (which is more massive than a galaxy) in the cosmological background, and estimated the order of magnitude of the difference between MOND (TeVes) and CDM. They showed that there is ~ 0.01 difference for the κ field. Also the amplitude of negative κ can be much bigger in other models (as those considered in Appendix A.2), or in the case of the PDM of a non-spherical cluster, for instance, the “bullet cluster” 1E0657-56.

Besides the prediction of negative $-\kappa$, the MOND also predicts that the distribution of effective dark matter on the Galactic disc follows the baryonic distribution (see panels a and c of Fig. 2.5), which is different from the spherical distribution of CDM. This fact should lead to some observable effects. We will discuss the physical effects of phantom dark matter on the Galactic disc in §A.1.

We finally note that, apart from these subtle (but important) differences, the amplitude of the total potential in the MOND model with an external field of $0.03a_0$ is very similar to the ones in the CDM models (see Fig. 2.3). This is especially true for the Bsc CDM model, which shares the same baryonic distribution as the MOND models. With an external field of $0.03a_0$, the ratio of total baryonic mass to total phantom mass created by MOND is about 0.03 at large radii, which is similar to the ratio of baryonic mass to virial mass of 0.04 in the Bsc model. This similarity will be even more apparent when comparing the corresponding circular and escape velocity curves in these models. Note, however, that as

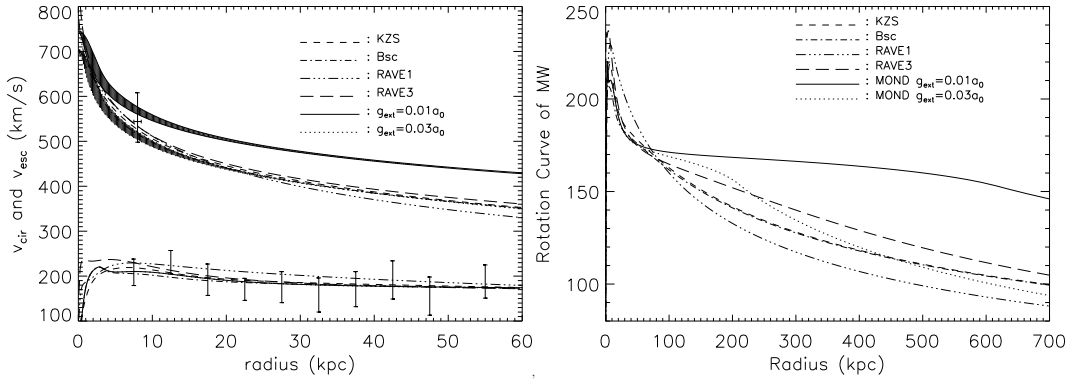


Figure 2.6: Left panel: the circular and escape velocities in the Galaxy calculated in the different models. The two shaded areas are the escape velocity in MOND within an external field of $0.01a_0$ and $0.03a_0$. The other upper curves are the CDM predictions for the escape velocity, as shown in the label. The error bar at 7.5-8.5kpc is the RAVE escape velocity. The data below are the circular speed measured by Xue et al. (2008) from SDSS field stars data. The circular speed curves in all our models are overplotted. Right panel: The rotation curve is plotted on a very large scale, showing the return to a Keplerian behaviour at large radii,

a consequence of the inherently flattened/triaxial potential at large radii in MOND, the escape velocity in MOND (see next subsection) is not completely the same at different positions on a spherical shell or cylinder of a given radius.

We further study the phantom dark matter disc of the Milky Way Galaxy in Appendix A, and we find that the dynamical surface density predicted by MOND fits well with the observations. A series of simulations have been carried out to study the negative phantom dark matter effects here, and those models are with Plummer sphere models. The negative phantom dark matter effect is weak. In addition, we found additional dynamical density peaks in binary systems (see Appendix A.2), as well as those systems embedded in external fields. The strength of this effect is about 1% of the baryonic peak of the satellite. Since these external field effects are faint, they are more of theoretical interest rather than having a prospect of being observed.

2.2.3 Circular and escape velocities

Prediction for galactic surveys

We can now compare the predicted circular and escape velocities as a function of position in the Galaxy in both the MOND and CDM context.

The rotation curve of the Milky Way at large radii is very poorly known (see e.g.

Binney & Dehnen 1997). However, in the CDM context, Xue et al. (2008) have recently used a set of halo stars from the Sloan Digital Sky Survey (SDSS) as kinematic tracers to estimate the rotation curve of the Galaxy out to 60 kpc. This estimated rotation curve is plotted on Fig. 2.6 together with the circular speed predicted in our different models. Clearly, it cannot be used to discriminate between CDM and MOND models: the escape velocity is a better discriminating test.

The MOND escape velocity as a function of radius is also plotted as shaded areas in Fig. 2.6 for a weak external field of $0.01a_0$ and for an external field of $0.03a_0$. This prediction is unique once the modulus and direction of the external field are fixed. However, the escape velocity is slightly different when considering it along different axes, which explains the use of shaded areas. Apart from the estimate based on the peculiar velocity of the Milky Way with respect to the CMB (see §1.2), the only real observational constraint we have on the external field modulus is the escape velocity from the Solar Neighbourhood as measured by Smith et al. (2007) with the high velocity stars from the RAVE survey. This local escape velocity was measured to be in the range $498 - 608 \text{ km s}^{-1}$ with 90% confidence, and a median of 544 km s^{-1} . This is consistent with all four CDM models presented above (by construction in the case of the two RAVE models) as can be seen on Fig. 2.6. To be consistent with the forementioned Besançon MOND model, the maximum allowed modulus of the external field is $0.03a_0$ (see also § 2.1 and Famaey et al. 2007a, Wu et al. 2007).

Very clearly, a higher escape velocity than the one of CDM models can actually be achieved at all radii in the most natural MOND model where the external field is $H_0 \times 600 \text{ km s}^{-1} \simeq 0.01a_0$, pointing to the direction of sun-Galactic center (the Milky Way is accelerated by the external fields from Great Attractor, which is lying off at a distance of around 46 Mpc, and pointing to the Hydra Centaurus supercluster). Despite their many degrees of freedom, the CDM-based models cannot achieve such high escape velocity as the MOND low external field model. Another striking prediction is that the circular and escape velocity in the MOND model with an external field of $0.03a_0$ are extremely similar to CDM, and especially to the Bsc model. Consequently, this MOND potential effectively mimicks the NFW potential advocated by KZS as far as circular and escape velocities are concerned (but it is not strictly identical since it tracks the baryons at small radii, and is flattened by the external field at large radii, where it also predicts negative convergence

Table 2.3: Velocities and Positions of Magellanic Clouds

<i>Parameters</i>	<i>Radius</i> (x, y, z)(<i>kpc</i>)	$ r $ (<i>kpc</i>)	<i>3D - Velocity</i> (v_x, v_y, v_z)(km s^{-1})	$ v $ (km s^{-1})
<i>LMC</i>	(-0.8,-41.5,-26.9)	49.5	($-86 \pm 12, -268 \pm 11, 252 \pm 16$)	378 ± 18
<i>SMC</i>	(15.3, -36.9, -43.3)	58.9	($-87 \pm 48, -247 \pm 42, 149 \pm 37$)	302 ± 52

for gravitational lensing).

The prediction for the escape velocity as a function of position could be highly interesting when compared with the inferred escape velocities that would be determined at various distances with planned or already-underway surveys such as RAVE, SDSS, SEGUE, SIM or GAIA. Similarly, future observations of hypervelocity stars (Hills 1988, Brown et al. 2007a,b) in the Galactic halo could also constrain the Galactic potential (Gnedin et al. 2005, Yu & Madau 2007) at these large distances. High enough escape velocities inferred from such surveys could ultimately rule out the four CDM models explored here, as well as the MOND model with an external field of $0.03a_0$.

In fact, an indication that the escape velocity might actually be higher than predicted by CDM at large radii is already suggested from the recently measured 3D velocity of the Large Magellanic Cloud (Kallivayalil et al. 2006a). As we shall see in the following, under the assumption that the LMC is bound to the Galaxy, the four CDM models presented here are only marginally viable (although not excluded).

Escape velocity of the LMC

The LMC is one of the nearest satellites of the Milky Way, located in galactocentric coordinates at $(x, y, z) = (-0.8 \text{ kpc}, -41.5 \text{ kpc}, -26.9 \text{ kpc})$ (Murai & Fujimoto 1980, Kallivayalil et al. 2006a,b, Besla et al. 2007). Recent measurements of the proper motion of the LMC with the Hubble Space Telescope have shown that its velocity is as fast as $378 \pm 18 \text{ km s}^{-1}$ (Kallivayalil et al. 2006a). Previous observations suggested the 3D velocity was ranging from 249.3 km s^{-1} to 367.83 km s^{-1} (Mastropietro et al. 2005, van der Marel et al. 2002, Murai & Fujimoto 1980, Gardiner et al. 1994, Heller & Rohlfs 1994). These previous values of the LMC's proper motion velocity were consistent with it being bound to the Galaxy in CDM models. However, with its newly measured velocity, Besla et al. (2007) already pointed out that it is difficult for the LMC to be a bound satellite, especially if one assumes CDM-based halos rather than an isothermal one (Hernández et al. 2001),

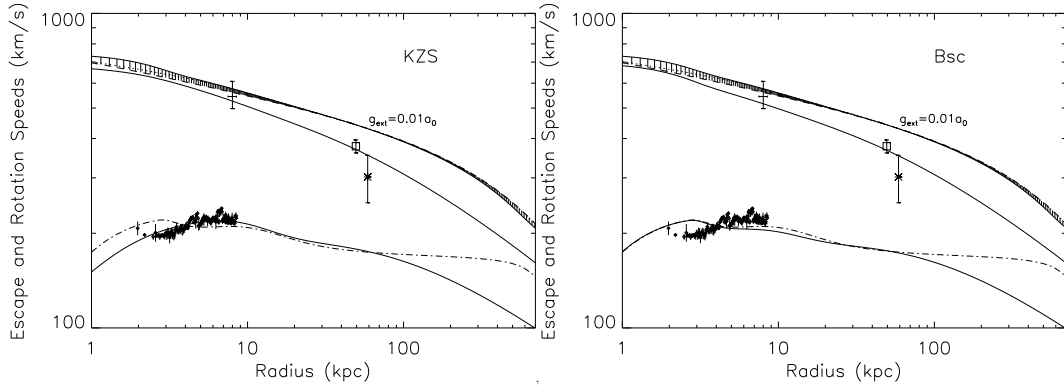


Figure 2.7: The solid lines on the left panel are the escape and circular speeds for the KZS B1 model (top solid line: escape velocity for MOND in the x -direction with external field of $0.01a_0$; Middle solid line: escape velocity of the KZS B1 model; Bottom solid line: circular speed of the KZS B1 model), and the solid lines on the right panel are the same for the Besançon model combined with the same NFW profile. The dot-dashed lines are the Besançon MOND (with low external field of $0.01a_0$) circular speed, and the shaded area is the escape velocity in MOND (with low external field of $0.01a_0$). The solid, dotted, dashed lines in the shaded area are the escape velocities in respectively the x (sun to galactic centre), y and z (perpendicular to the disc plane) directions. Black dots with error bars are the observed circular velocity (Clemens 1985) and the error bar at 8.0 ± 0.5 kpc is the escape velocity in the solar neighbourhood measured from the RAVE survey. The square with error bar is the newly measured LMC speed (Kallivayalil et al. 2006a), while the star with error bar is the SMC speed (Kallivayalil et al. 2006b). Note that, as seen on Fig. 2.6, all rotation curves are also in accordance with the rotation curve of Xue et al. (2008), not plotted in order not to overcrowd the figure.

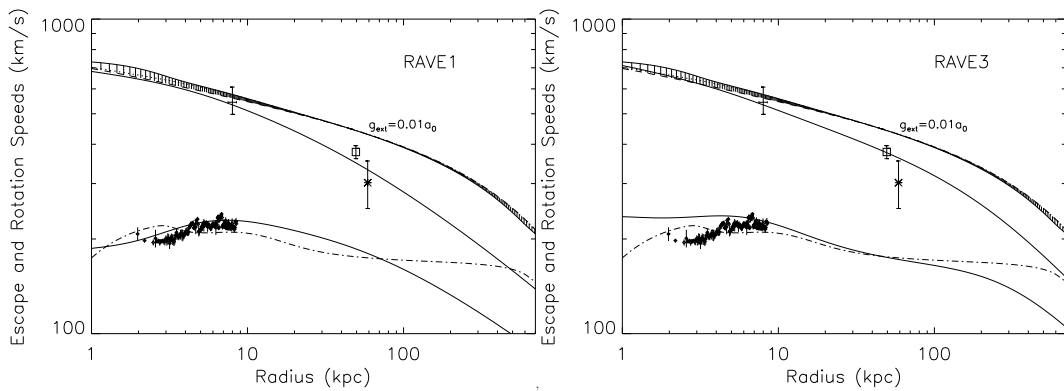


Figure 2.8: RAVE models of the Milky Way. The left and right panels are figures for the NFW and WE halos respectively. The symbols are the same as in Fig 2.7.

Table 2.4: Observed 3D velocity and escape velocity at the position of the LMC (in unit of km s^{-1})

Observation	MOND(EF=0.01 a_0)	MOND(EF=0.03 a_0)	KZS	Besançon	RAVE1	RAVE3
378 ± 18	(441.8, 442.8, 442.0)	(366.0, 367.8, 366.9)	368.9	366.9	348.6	375.7

unnatural in the CDM framework (and actually resembling the MOND potential, the external field defining the truncation). The positions and velocities of the Magellanic Cloud system are listed in Table 2.3, while the escape velocity at the position of the LMC in our different CDM and MOND models are listed in Table 2.4. It can be directly seen that the CDM models can only weakly bind the LMC, the huge velocity of the LMC being in the critical range of escaping. However, we see that a MOND model with a weak external field of $0.01a_0$ provides a much deeper potential at the galactocentric radius of the LMC and strongly binds the Magellanic Clouds. The SMC is bound in both the MOND and CDM frameworks, but in CDM it leaves open the question of why the brother galaxy LMC is close to escape. Note, however, that within one sigma-error, the SMC could also be unbound to the MW in all four CDM models, and that the LMC can still be bound at the one-sigma level in three of our four CDM models.

The first panel of Fig 2.7 shows the circular and escape velocity curves (on a logarithmic scale) of the KZS B1 model compared with the MOND (low external field) model. This logarithmic abscissa allows us to have a clearer view of the large-scale behavior of the circular and escape velocity curves. For the CDM model to be consistent with the observed circular velocities and RAVE-inferred escape velocity, the escape velocity at the position of the LMC must be smaller than (or equal to) the newly measured mean-value of the 3D velocity. Besla et al. (2007) have shown that an escape velocity of 552 km s^{-1} at 50 kpc could still be consistent with the rotation curve of the inner Galaxy, if the virial mass within 200 kpc is increased to $2 \times 10^{12} M_\odot$ and the concentration is decreased to $c = 9$. However, this model is in direct contradiction with the local escape velocity from the Solar neighbourhood measured by Smith et al. (2007). As for the KZS B1 in which the CDM halo could still bind the LMC, such a case is marginal and the LMC is only weakly bound. In contrast, the MOND potential with an external field of $0.01a_0$ is significantly deeper. Therefore, the LMC is undoubtedly captured by the Galaxy in this MOND potential.

The escape velocity as a function of radius (on a logarithmic scale) for the Bsc model

is shown in the second panel of Fig. 2.7. Again, the LMC speed is in the critical escape velocity range in the NFW CDM framework. On the two panels of Fig. 2.7, the CDM escape velocities are nearly the same, especially at large radii, due to the fact that they have the same CDM halo profile. The baryons affect the rotation curve in the central regions, but have little contribution to the escape velocity in the CDM framework.

Finally, we compare the escape velocity in the two RAVE models with the MOND (low-external field) model in Fig. 2.8. The problem of binding the LMC to the Galaxy is even more severe in this case; the NFW halo cannot bind the LMC anymore. The RAVE 3 model also overestimates the circular velocity because the central region of the Wilkinson-Evans profile is much too dense. However, even in this RAVE 3 model, the escape velocity at the LMC position is predicted to be similar to the actual velocity of the LMC, which means that the LMC is only bound at the one-sigma level.

If more precise measurements of the 3D velocity of the LMC in the future imply that the LMC is truly unbound to the Galaxy in the CDM models, it could be a serious problem to explain the formation of the Magellanic stream by tidal stripping and ram pressure stripping. As already advocated by (Besla et al. 2007), the LMC would be on a parabolic orbit and would not have suffered any pericentric passage or crossed the disk before. In MOND with a low external field the LMC could then still be on a bound orbit, but the problem might be that this orbit would have a very long period (approximately 3 Gyr), and might not cross the disk often enough. However, the effect of the external field of the Galaxy on the self-gravity of the LMC might make it easier for ram pressure stripping to take place. A detailed study of the orbit and evolution of the internal structure of the LMC in MOND is however beyond the scope of this thesis, and will be the subject of further studies.

Constraining MOND and CDM potentials with Hypervelocity stars

Measurements of the LMC velocity thus provide a unique quantitative observational tool for studying the Galactic potential at large distances. However, an additional observational measure, which is independent of the LMC velocity, may become accessible in the near future through the observations of Hypervelocity Stars (HVSs) .

In recent years several HVSs have been observed at large distances in the Galactic

halo (up to 100 kpc; Brown et al. 2007a). These stars are escaping stars with extremely high peculiar velocity. Most of them are main-sequence B stars (with mass of $3 - 4M_{\odot}$), and some of them are Blue Horizontal Stars. The orbits of the HVSs are highly radial. It is important and easy to distinguish the high velocity stars (runaway stars) and the HVSs. The former stars are more massive (with mass of $1.5 - 6M_{\odot}$), and their velocities are smaller (with a velocity dispersion of 30 km s^{-1} to the local standard of rest, which is about three times of the velocity dispersion of normal stars). The velocity dispersion of the HVSs could be $100 - 110 \text{ km s}^{-1}$. The runaway stars can be bound to the Galaxy, while the HVSs are mostly unbound (Bromley et al. 2009). The heliocentric distances of the HVSs are in the outer part of the Galaxy, ranging from several tens to several hundreds of kpc. There are several popular proposals for the origin of the extremely high speeds of the HVSs: (i) they are from the ejection by the central massive black hole, probably following binary disruption by the massive black hole in the Galactic centre (Hills 1988, Yu & Tremaine 2003, Perets et al. 2007); (ii) they are from the interactions of a single star with an immediate-mass black hole; (iii) they are scattered by a stellar-mass black hole. Here we adopt the first proposal to study the velocity of the HVSs (Perets 2009, Bromley et al. 2009, Lu et al. 2010).

Some of these HVSs have velocities extending much beyond the escape velocity from the Galaxy, where others are still bound to the Galaxy (Brown et al. 2007a). Recently Gnedin et al. (2005) and Yu & Madau (2007) suggested to use the kinematics of HVSs in order to probe the galactic potential using the position and velocity vectors of HVSs at large Galactocentric distances. Under the assumption that HVSs were ejected from the galactic centre they suggest to measure the departure from purely radial orbits of these HVSs, due to the (possible) triaxiality of the galactic potential. The slight perturbations from radial orbits are then used in order to estimate the level of triaxiality of the Galaxy. Both Gnedin et al. and Yu & Madau have focused on measuring the triaxiality of the galactic potential in the context of CDM models. However, given the large deviation of MOND potentials from spherical symmetry (relative to CDM potentials), these methods could be even more useful for excluding or confirming MOND models for the Galaxy. In addition, studies of propagation times and especially the return times of bound hypervelocity stars (Perets et al. 2009) could be highly valuable in constraining MOND potentials such as discussed here up to very large distances ($>100 \text{ kpc}$). More measurements of HVSs velocities,

especially at large galactocentric distances are expected to be obtained in the few coming years, and could much better constrain our knowledge on the galactic potential.

Note that for an isolated model of the Milky Way, MOND permits no escape. Fortunately the Milky Way is embedded in an external field, in the order of $0.01a_0$, hence no returning HVSs does not rule out MOND. Fig. 2.6 shows the escape velocity in different strength of external field for the Milky Way. If any of the returning HVSs is observed with a velocity above the predicted escape velocity curves of the four CDM models and the MOND model with $0.03 a_0$ external field in Fig. 2.6, then the corresponding models are rule out. Hence the future observations will provide us more constraints on the Galactic potential. The escape speed in MOND within an external field is non-isotropic (see the shadows of Fig. 2.7 and Fig. 2.8). Hence the potential of the Galaxy is non-symmetric. HVSs can escape in the direction of external field, and more difficult to escape in the anti-direction of external field.

Escape velocity with a component of hot baryons

In the latest observations on X-ray O_{VII} absorption lines by Yao et al. (2008), they constrained the column density of the hot gas around the Milky Way to be $N_{O_{VII}} \leq 5 \times 10^{15} \text{ cm}^{-2}$, and the total mass of the hot gas in (10 – 250) kpc to be $\leq 6 \times 10^{10} M_{\odot}$. For completeness we explore the sensitivity of our predictions to the possibility of a small amount of uncooled, moderately hot baryons existing at large radii in the Galaxy. For this purpose, we added to the Besançon (cool) baryons model a Plummer sphere of $4 \times 10^{10} M_{\odot}$ with a Plummer scale-length of 100 kpc. In CDM models, this does not affect the prediction since the potential is completely dominated by the CDM halo. In MOND, however, the prediction becomes quite different. The rotation curve remains almost unchanged in both the $0.01a_0$ and $0.03a_0$ external field cases, but the escape velocity is boosted by about 30 km/s at the Sun’s position. In that case, the $0.01a_0$ external field model is only marginally compatible with the RAVE-measured local escape velocity, while the $0.03a_0$ model becomes more comparable to the original $0.01a_0$ model, and strongly binds the LMC while still being compatible with the local escape velocity (see Fig. 2.9). This again demonstrates that MOND models are not unique as is commonly assumed.

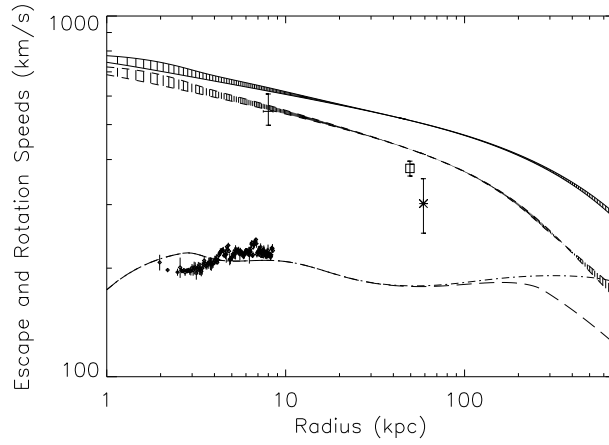


Figure 2.9: Circular and escape velocities in Besançon MW baryon model + hot, diffused gas around MW. A Plummer model for the hot gas component is used, with mass of $4 \times 10^{10} M_{\odot}$. The two shaded areas are the escape velocities within external field of $0.01a_0$ (upper) and $0.03a_0$ (lower), and the two bottom curves show the circular velocities. The dot-dashed line is the MOND rotation curve for the MW embedded in an external field of $0.01a_0$, and the long dashed line is for the $0.03a_0$ external field. The symbols of observations are the same as in Fig 2.7.

2.2.4 Conclusion & Discussion

In this chapter, we modelled the Milky Way with several different CDM-based models, and compared them with the MOND framework. We first showed that the isopotentials are more spherical in CDM, at small radii because the baryonic matter does not affect the potential as much as in MOND, and at large radii because the external field flattens the potential in MOND. In CDM, the halo dominates the shape of the potential at large radii, and consequently the escape velocity at different positions on a given spherical shell show only negligible differences. Note that all of our studied CDM halos were spherical, while recent studies on CDM found that the density profiles of massive halos should rather be triaxial (Jing & Suto 2002, Bailin & Steinmetz 2005, Allgood et al. 2006, Macciò et al. 2007). A mean axis ratio $\bar{q} = \frac{a_2 + a_3}{2a_1}$ is defined, where a_1 , a_2 and a_3 are the major, intermediate and minor axis. In Macciò et al. (2007), for a Milky Way-like dark halo with a virial mass of $10^{12} M_{\odot}$, one has $\bar{q} \sim 0.76_{-0.15}^{+0.1}$. Such triaxial dark halos would change the potential contours inside the virial radius: the potentials would be flattened as well. Nevertheless, when the radius is far larger than the virial radius (e.g. 10 times the virial radius), the potential contours would become spherical again.

We also showed that the effective, phantom dark matter densities predicted by MOND can be negative at large radii (where the internal and external acceleration are of the same

order of magnitude), in a fat disc perpendicular to the external field (see also Milgrom 1986). A negative convergence parameter could thus in principle be observed in the gravitational lensing generated by Milky Way-like galaxies, although it would be very sensitive to the detailed non-constant gravitational field of the environment.

In addition, we found the circular and escape velocity as a function of position in the different models. We showed that the rotation curves in all models are compatible with the inner rotation curve (Clemens 1985) as well as with the SDSS-measured rotation curve at large radii (Xue et al. 2008). This is true for various μ -functions in MOND (“standard” and “simple”), but the form adopted here fits best the rotation curve (the “simple” form of Famaey & Binney 2005). On the other hand, the prediction of escape velocity as a function of position will be very useful for comparison with inferred velocities from the data of planned or already-underway surveys such as RAVE, SDSS, SEGUE, SIM or GAIA or the hypervelocity stars survey. We stress that MOND models are far from unique, and that the freedom allowed for the modulus of the external field makes the MOND models actually more flexible than CDM-based ones with respect to the escape velocities that could be derived from the kinematic surveys. High escape velocities would rule out the four CDM models studied here, while any escape velocity between the two curves plotted on Fig. 2.6 would only represent a constraint on the external field in which the Milky Way is embedded in MOND. We also note that the MOND model with an external field of $0.03a_0$ mimicks the CDM ones in terms of both circular and escape velocity curves. Let us finally point out that we did not take into account any effect of the cosmic acceleration in either the CDM or MOND context, which could have some effect on both predicted escape speed curves.

We then note that the newly-measured value of the 3D velocity of the LMC (Kallivayalil et al. 2006a,b, Besla et al. 2007) could already be an indication that escape velocities in the outer Galaxy could actually be higher than that predicted by the CDM models (as well as by an external field of $0.03a_0$ in MOND), under the assumption that the LMC is bound to the Milky Way. More precise measurements of the 3D velocity of the LMC will be needed to disentangle this issue, but with its present value we found that the LMC is only bound at the one-sigma level in three of our four CDM models (and unbound at the one-sigma level in the fourth one). In this context, we note that the reanalysis of the LMC proper motion by Piatek et al. (2007) yields a smaller value of 358 km s^{-1} (radial

and tangential velocities then being 93.2 km s^{-1} and 346 km s^{-1}), which is consistent with the lower error bound of (Kallivayalil et al. 2006a). In the MOND context, the measured velocity of the LMC can be used as a constraint on the modulus of the external field in order to keep it bound: we found that an external field of less than $0.03a_0$ is needed, an upper limit strikingly similar to that needed to explain the local escape speed from the solar neighbourhood (Famaey et al. 2007a, Wu et al. 2007). We also suggest that future observations of hypervelocity stars could add additional independent constraints that could even better constrain the models studied here.

It is finally important to note that because of their cuspidity, it will always be difficult for the four CDM models explored in this chapter to reproduce the non-axisymmetric motions of gas in the longitude-velocity diagrams of the baryon-dominated inner Milky Way, as extensively discussed in Famaey & Binney (2005). It remains to be seen what the prediction of a MOND model is for these non-axisymmetric gas motions. Still, since we showed that the MOND potential (and phantom dark matter) tracks the baryonic distribution quite well at small radii, and since the best fit to these non-axisymmetric motions of the gas produced by the bar was obtained with a purely baryonic model (Bissantz et al. 2003), it is likely that they could be explained within the MOND context.

We thus conclude that the MOND model studied in this section, with an external field of modulus $0.01a_0$ directed in the Sun-Galactic centre direction (a combination of external field from M31 and from LSS), fits all the present observations of the Milky Way extremely well. If a component of unseen, moderately hot, baryons is added, the preferred value of the external field however becomes higher ($0.03a_0$).

3

Schwarzschild's method and MONDian field elliptical galaxies

Galaxies are generally non-spherical, and appear in all shapes and profiles. Apart from the beautiful disc galaxies, there are elliptical galaxies which are often axisymmetric or triaxial and appear stable. Since cuspy triaxial ellipticals in nature are purely bound by gravity, any mathematical theories of gravitation must allow such shapes to exist and be stable. A triaxial equilibrium is non-trivial to build dynamically especially for a system with a cuspy profile of the light and/or the dark halo. Schwarzschild's approach (Schwarzschild 1979) supplies a powerful way of constructing quasi-equilibrium models and is widely used to test the self-consistency of galaxies.

The main objective of this chapter is to test whether triaxial models of galaxies are stable in Modified Newtonian Dynamics (MOND, (Milgrom 1983c)). Extensive studies about the stability of triaxial models have been performed in standard Newtonian Gravity (see below), however, there is no literature on this topic in MOND.

In this chapter, we briefly introduce Schwarzschild's method (Schwarzschild 1979, 1982, Merritt & Fridman 1996, Zhao 1996), and then we perform a stability test of triaxial models in MODified Newtonian Dynamics (MOND) using N-body simulations. The triaxial models considered here have densities that vary as r^{-1} in the center and r^{-4} at large radii. The total mass of the model varies from $10^8 M_\odot$ to $10^{10} M_\odot$, representing the mass scale of dwarfs to medium-mass elliptical galaxies, respectively, from deep MOND to quasi-Newtonian Gravity. We find that the systems are stable once they reach the equilibrium state.

3.1 An introduction to Schwarzschild's approach

The approach of Schwarzschild can be divided into three steps (Schwarzschild 1979, 1982):

1. An analytic density distribution is chosen and the gravitational potential is obtained from Poisson's equation (or a modified Poisson's equation in MOND). The whole system is then segmented into many equal mass cells.
2. A full library of orbits within the previously calculated potential is computed, and the time spent in each cell is recorded.
3. A non-negative linear superposition of orbits reproducing the original density profile is determined. This step does not guarantee that people can always obtain the self-consistent solutions. Not all density profile models have self-consistent solutions even in Newtonian gravity Merritt & Fridman (1996).

For Newtonian physics, there have been three decades of studies on constructing a self-consistent model for triaxial galaxies since Schwarzschild numerically presented the triaxial Hubble profile in 1979 (Schwarzschild 1979, 1982). Despite its original application to a modified Hubble profile, the method of Schwarzschild (1979) is still widely used for testing the self-consistency of various models for the density distribution in galaxies. For instance, Statler (1987) showed that the perfect triaxial (Kuzmin 1973) profile and the de Zeeuw & Lynden-Bell (1985) profiles are also self-consistent. While those models have constant density cores, observations showed that elliptical galaxies have power-law "cusps" in the cores (Moller et al. 1995, Crane et al. 1993, Ferrarese et al. 1994, Lauer et al. 1995), i.e. the surface brightness increases quickly towards the central region of the galaxies. Almost all

elliptical galaxies have power-law cusps $\rho \sim r^{-\gamma}$. Low surface brightness galaxies (LSBs) have steeper centres, $\gamma \approx 2$, while high surface brightness galaxies (HSBs) have shallower cusps, $0 \leq \gamma \leq 1$. Tremblay & Merritt (1996) found that the intrinsic shapes of HSBs and LSBs are different: the short-long axis ratio of HSBs has a peak at 0.75, and of LSBs has a peak at 0.65. Spherical models with a fixed value of γ have been proposed, e.g. a $\gamma = 2$ model by Jaffe (1983) and a $\gamma = 1$ model by Hernquist (1990a).

Today such models are rather discussed within a family of density distributions with γ being a free parameter (Dehnen 1993), following $\rho \sim r^{-\gamma}$ at the cusp centre and $\rho \sim r^{-4}$ at distant radii:

$$\rho(r) = \frac{(3 - \gamma)M}{4\pi abc} \frac{1}{r^\gamma(1 + r)^{4-\gamma}}, \quad 0 \leq \gamma < 3, \quad (3.1)$$

where $r = \sqrt{(\frac{x}{a})^2 + (\frac{y}{b})^2 + (\frac{z}{c})^2}$, ($c \leq b \leq a$), a , b and c are the typical scale length of long, intermediate, and short axes of the ellipsoid. In this regard, Merritt & Fridman (1996) tested the Dehnen profile, and found self-consistent triaxial galaxies with central density cusps ($\gamma = 1, 2$) in Newtonian dynamics when some fraction of the chaotic orbits in the models are "unmixed". For instance, the self-consistent solutions of $\gamma = 1$ model can be found when the fully mixed chaotic orbits only existing in the inner six sectors (see the grid segmentation in §3.2.3), and the $\gamma = 2$ self-consistent model can include such orbits only in the inner two sectors. They also found that if their models are constructed by fully mixed chaotic orbits, there are no self-consistent solutions. The subsequent work by Capuzzo-Dolcetta et al. (2007) proved that a two-component triaxial Hernquist system, including a baryonic component plus a Cold Dark Matter (CDM) halo, can also be self-consistent.

Various topics of MOND have been studied through N-body simulations, as mentioned in §1.1.2. Those differences and similarities to CDM N-body simulations immediately lead to the question of the stability of triaxial systems in MOND, as realistic galaxies are not spherically symmetric objects. Wang et al. (2008) recently found that the self-consistency of a triaxial cuspy centre $\gamma = 1$ also exists for MOND. By extending the original Schwarzschild method and weighting the orbits during the generation of the Initial Conditions (ICs) for N-body simulations it is possible to study the stability and future evolution of these density models (Zhao 1996). This method proved successful in, for instance, creating equilibrium ICs for a fast-rotating, triaxial, double-exponential bar reminiscent of a steady-state Galactic bar (Zhao 1996) when evolved forward in time using

a Self-Consistent-Field code (Hernquist & Ostriker 1992).

Little is known about the MOND-solutions for elliptical galaxies, and even less about triaxial ellipticals or ellipticals with black holes. Do triaxial galaxies have equilibrium MOND solutions? Are they stable both in an isolated environment and in a cluster environment? Tests of the existence and stability of triaxial elliptical galaxies with cusps is a minimal requirement for a modified gravity theory.

3.2 Models, Schwarzschild technique, and ICs for N-body

3.2.1 MONDian Gravity

The MONDian Poisson's equation Eq. 1.19 is (Bekenstein & Milgrom 1984):

$$\nabla \cdot \left[\mu \left(\frac{|\nabla\Phi|}{a_0} \right) \nabla\Phi \right] = 4\pi G\rho, \quad (3.2)$$

where Φ is the MONDian potential generated by the matter density ρ . For the gravity acceleration constant, we use $a_0 = 3600 \text{ km}^2\text{s}^{-2}\text{kpc}^{-1}$, which is the same as that adopted by Milgrom (1983c,a), Sanders & McGaugh (2002), Bekenstein (2006). The so-called MONDian interpolation function μ is approaching 1 for $|\nabla\Phi| \gg a_0$ (Newtonian limit) and $\mu \rightarrow \frac{|\nabla\Phi|}{a_0}$ for $|\nabla\Phi| \ll a_0$ (deep MOND regime), and the gravity acceleration is then given by $\sqrt{a_0 g_N}$, taking the place of the Newtonian acceleration $g_N = \nabla\Phi_N$ at the same limit. For our simulations we chose the 'simple' μ -function in the form of (Famaey & Binney 2005, Zhao & Famaey 2006, Sanders & Noordermeer 2007):

$$\mu(x) = \frac{x}{1+x}. \quad (3.3)$$

Furthermore, we use the density distribution given by Eq. 3.1, choosing $\gamma = 1$, and M being the total mass of the system. Since the $a : c$ is peaked at 0.75 for bright galaxies and is peaked at 0.65 for faint galaxies, for our simulations, we choose the ratios $a : b : c = 1 : 1 : 0.7$ and $a : b : c = 1 : 0.86 : 0.7$, with $a = 1\text{kpc}$. The parameters of the models are listed in Table 3.1.

3.2.2 Initial Potential

A very important step in our calculation is to solve Poisson’s equation in MOND (cf. Eq. 3.2). This is achieved via numerical integration utilizing the N-body code NMODY (Ciotti et al. 2006, Nipoti et al. 2007a) on a grid of spherical coordinates (r, θ, ψ) . To this extent we applied a grid of $256 \times 64 \times 128$ cells. Note that we do not yet evolve the system forward in time; we simply extract the potential of our (static) density distribution and use it for the Schwarzschild method detailed below.

3.2.3 Schwarzschild technique

Schwarzschild (1979, 1982) proposed the orbit superposition method to reproduce the density distribution of galaxies and build triaxial galaxy models. The details of this method are discussed here. The basic idea is to compute a large library of orbits in a given potential, and determine the superposition of orbits that provides the best fit to the observational density distribution or the underlying density model. Let N_{orbits} be the number of the orbits in the library ($j \in N_{orbits}$) and N_{cells} the total number of grid cells segmenting space ($i \in N_{cells}$). Further, let O_{ij} denote the fraction of time spent by the j th orbit in the i th cell. The weight and mass of the j th orbit are defined by w_j and m_i , respectively, and they are related by the following set of linear equations:

$$\sum_{j=1}^{N_{orbits}} w_j O_{ij} = m_i \quad (3.4)$$

Schwarzschild’s method is widely used to build spherical, axisymmetric and triaxial models for galaxies (Richstone 1980, 1984, Pfenniger 1984, Richstone & Tremaine 1984, Zhao 1996, Rix et al. 1997, van der Marel et al. 1998, Binney 2005, Capuzzo-Dolcetta et al. 2007, Wu et al. 2009).

The O_{ij} array is obtained by outputting the superpositions of the j th orbit in equal time intervals $\Delta\tau_j$, and counting the number of output points ν_{ij} in the i th cell. After that the elements are determined according to

$$O_{ij} = \frac{\Delta\tau_j \times \nu_{ij}}{\Delta\tau_j \times \nu_j} = \frac{\nu_{ij}}{\nu_j}, \quad (3.5)$$

where ν_j is the total output number of the j th orbit.¹

There are now various choices of how to actually solve Eq. 3.4: liner programming (Schwarzschild 1979, 1982, 1993), Lucy's method (Lucy 1974, Statler 1987), maximum entropy methods (Richstone & Tremaine 1988, Statler 1991, Gebhardt et al. 2003), or least-square solvers (Lawson & Hanson 1974, Merritt & Fridman 1996, Capuzzo-Dolcetta et al. 2007). We chose the least-square method (cf. Wang et al. 2008).

Grid Segmentation

Because of the symmetry of the mass distribution specified by Eq. 3.1, it is sufficient to only consider mass cells in the first octant in our analysis. Following Merritt & Fridman (1996), we divide the first octant into many small cells (the smallest building blocks) of equal mass:

The first octant is divided into 21 radially separated equal mass sectors by 21 spheriods, at the radius of²

$$r_n = \frac{\sqrt{M_n(r_n)}}{\sqrt{M} - \sqrt{M_n(r_n)}} \times 1.0 \text{ kpc}, \quad M_n = \frac{n}{21}M, \quad n = 1, 2, \dots, 21. \quad (3.6)$$

Then each sector is further divided into 3 sub-sectors using the suitable half-planes $z = cx/a$, $y = bx/a$, and $z = cy/b$, respectively (see the left panel of Fig. 3.1. Again, each sub-sector is divided into 16 equal mass segments (cells) by an angular refinement defined by the planes $ay/bx = 1/5, 2/5, 2/3$ and $az/cx = 1/5, 2/5, 2/3$ for the sub-cell adjacent to the x -axis (middle panel), and in a similar way for the others. Thus we have in total $16 \times 3 \times 21 = 1008$ equal mass cells including the outermost sector ($r > r_{20}$ in Eq. 3.6). In this section, the outermost two sectors including $2 \times 48 = 96$ cells are not taken into account because the sector's boundaries extend to infinity. Since the density evolves as $\rho \sim r^{-4}$ at large radii, the orbits in this sector should contribute much less than all other orbits, and thus they are negligible.

¹Note that in Wang et al. (2008), Wu et al. (2009), when obtaining the O_{ij} array from Eq.3.5, we used non-equal time interval outputs, given by the variation of the gravitational field strength, $\Delta\tau'_j \sim 1/\sqrt{|\vec{\nabla} \cdot \vec{g}|}$. In this case, the real time intervals $\Delta\tau'_j$ of the j th orbit are not constant any more. However, in our previous stuides we neglected the unevenness of the time intervals between the outputed points along an orbit, and we calculated the O_{ij} array using $O_{ij} \approx \nu_{ij}/\nu_j$, which can cause systematically more output points in the cuspy centres. We rerun the simulations with equal time intervals and our present analysis in this thesis does not make this inaccurate approximation.

²The enclosed mass inside r is $M(r) = M \frac{r^2}{(r+A)^2}$ in Hernquist (1990a), and here we choose $A = 1$ kpc.

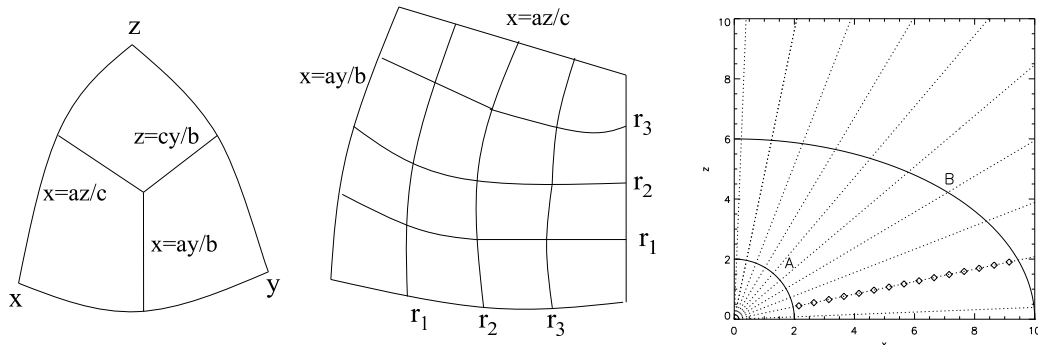


Figure 3.1: The first octant is divided by 21 ellipsoids into 21 sectors, and each sector is segmented by planes $z = cx/a$, $y = bx/a$ and $z = cy/b$ into three sub-sectors (left panel). Each sub-sector is subdivided by planes $ay/bx = 1/5, 2/5, 2/3$ and $az/cx = 1/5, 2/5, 2/3$ into 16 cells (middle panel). The right panel shows the initial ejecting positions for the non-zero initial velocity orbits. Curve A is the circle of the minimal radius of 1:1 resonant orbit at the energy E_k , curve B is the zero-velocity surface of the energy E_k . There are 10 dotted lines $x = z \tan \theta$ divide the values of θ from 2.25° to 87.75° . The 15 diamonds equally divide the radius into 16 parts. The diamonds are the initial positions from which the $x - z$ orbits are launched.

Integration of orbits

We followed Schwarzschild (1993) and Merritt & Fridman (1996) in assigning initial conditions from two sets of starting points (cf. also Wang et al. 2008):

1. stationary orbits with zero initial velocity,
2. orbits in the $x - z$ plane with $v_x = v_z = 0$, and $v_y = \sqrt{2(E - \Phi)} \neq 0$ in the first octant, where E is the total energy per unit mass, and Φ is the potential.

Note that there is quite a large number of non-symmetric orbits that will lead to artifacts in the procedure if only being considered in the first octant. To circumvent this problem and to keep the symmetry of the system, we reflect the orbits from the boundaries of each octant. Note that by our method the computational workload is not increased as would be the case when calculating eight octants.

As mentioned above, there are 16×3 cells in each sector. To obtain enough orbits for the library, we sub-divide the cells by the midplanes of the cells once again, i.e., the midlines of each grid as seen in the middle panel of Fig. 3.1; these midlines equally divide

the cell at $x = az/c$ and $x = ay/b$. Thus we have $4 \times 16 \times 3 = 192$ sub-cells in each sector. The central points on the outer shell surfaces of the sub-cells are the launching points. Hence there are 192 stationary starting orbits in each sector. There are $192 \times 20 = 3840$ free-falling orbits in the first octant. Since the initial conditions of these orbits do not have angular momentum, the orbits can cross the centre of the system and change its sign of angular momentum. Box orbits can be produced by the stationary initial conditions. We defined a velocity box

$$\text{box} = \frac{\max(3v_x^2) \cdot \max(3v_y^2) \cdot \max(3v_z^2)}{\max(v_x^2 + v_y^2 + v_z^2)^3} < 1, \quad (3.7)$$

when the velocity of an orbit satisfies the above inequality. The inequality 3.7 makes almost a rectangular box inside a maximum energy sphere (with a boundary of $\max(v_x^2 + v_y^2 + v_z^2)$) in the velocity space (v_x, v_y, v_z) . We classify this orbit as a box orbit. Note that the time-averaged angular momentum is zero.

The total energy on the k th sector is defined as the outer boundary shell E_k , and for the stationary orbits inside the k th sector this amounts to $E_k = \Phi(x, y, z)$. For the orbits launched from the $x - z$ plane the initial energy is $E_k = \Phi(x, 0, z)$, as shown in Fig. 3.1 (right panel). This figure further shows that the radius of the inner shell (marked as curve A) is the minimal radius of 1:1 resonant orbits (x:y), and the outer shell (marked as curve B) is the zero velocity surface where $E_k = \Phi$. We define 10 lines satisfying $x = z \tan \theta$ where θ lies within the range 2.25° to 87.75° . Along the radial direction, we equally divide the radius between two boundaries into 16 parts with 15 points. These 15 points are the initial positions for the orbits launched from the $x - z$ plane. Hence there are 150 $x - z$ plane starting orbits in each sector, and $150 \times 20 = 3000$ ejecting orbits in the first octant. The orbits ejected with initial velocity of $(0, \sqrt{2(E_k - \Phi)}, 0)$ have non-zero angular momentum. The orbits that conserve the angular momentum during the whole simulation are classified as loop orbits. There are two families of loop orbits since the initial L_x and L_z are not zero. We classify those orbits whose sign of the angular momentum around long-axis does not change during the whole simulation, i.e. $L_x = yv_x - zv_y > 0$, as the long-axis loop orbits. Or in other words,

$$\max(L_x) \times \min(L_x) > 0. \quad (3.8)$$

Similarly, the short-axis loop orbits are defined as

$$\max(L_z) \times \min(L_z) > 0. \quad (3.9)$$

These orbits cannot go across the centre of the system, because at this point the angular momentum is zero.

The other types of orbits, beyond the definition of boxes and loops, are classified as chaotic orbits.

In a spherical system, the total energy and the three components of the angular momentum are integrals-of-motion. However, in a triaxial system only the energy remains constant (Merritt 1980). We use an orbital integration code which adopts a 7/8 order Runge-Kutta method (Fehlberg 1968) to ensure the accuracy of the orbits (Wang et al. 2008). We integrate for 100 orbital times (see Section 3.3.1 for each orbit).

In summary, we have 192 stationary and 150 $x-z$ plane orbits in each sector amounting to a total of $N_{\text{orbits}} = 6840$ and we use $N_{\text{cells}} = 16 \times 3 \times 19 = 912$ cells for the generation of our orbit library. The energy in each sector is a constant which equals the potential energy on the outer shell surface. As a result, the energies for the systems can be considered ‘quantized’ with each system having 19 ‘energy levels’. There are four families of orbits in our classification: long-axis loop orbits, short axis loop orbits, box orbits and chaotic orbits.

In left panels of Fig. 3.2 we show the shapes of orbits from different families without regularization.

Obtaining weights

Once the orbit libraries are built and the O_{ij} array is recorded, we can calculate the orbital weights in Eq. 3.4. The right hand side of Eq. 3.4 denotes the mass of the i^{th} cell which we obtain from Monte-Carlo simulations using the analytic density distribution. The linear system is then solved by applying a non-negative least square (NNLS) method (the NNLS algorithm is introduced by Lawson & Hanson (1974)) which minimises the

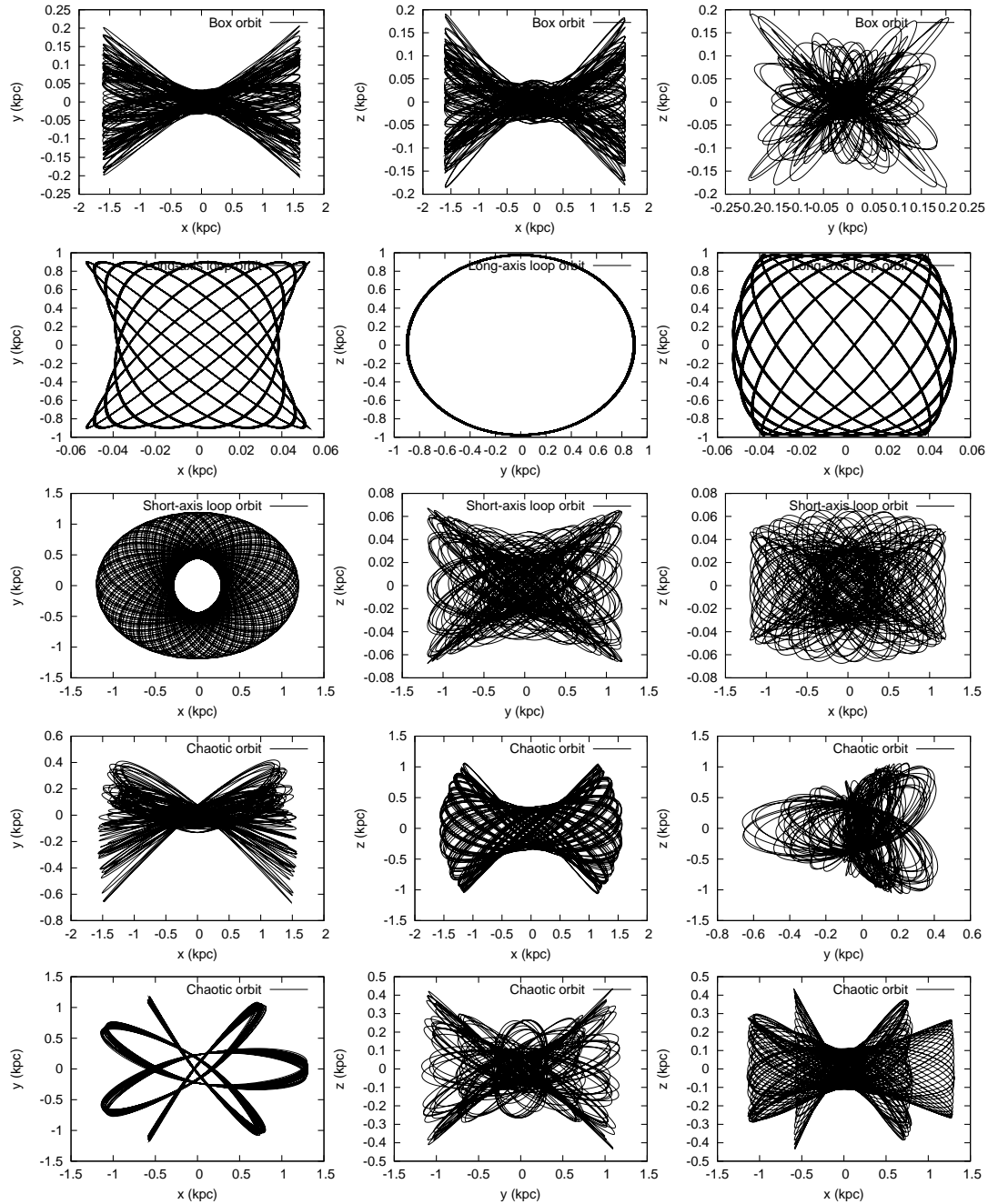


Figure 3.2: The above panels show the shape of orbits from different families. The spatial distribution of each orbit are projected on $x - y$ (**left panels**), $x - z$ (**middle panels**) and $y - z$ (**right panels**). We used an array T_{ij} to label the positions of the panels. The uppermost panels (T_{1j} , $j=1,2,3$) are the spatial distribution of a box orbit. Below the box orbit the panels show an long-axis loop orbit (T_{2j}) and a short-axis loop orbit T_{3j} . T_{4j} and T_{5j} panels are chaotic orbits.

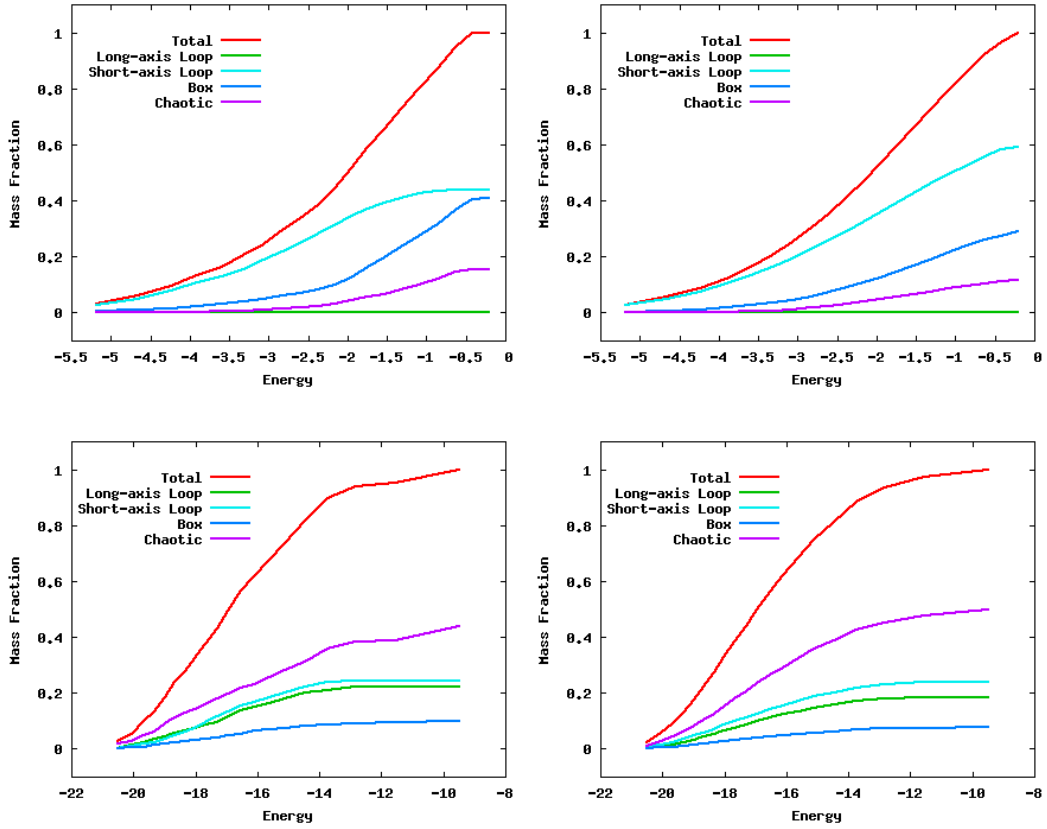


Figure 3.3: Left panel: The accumulated energy distribution of different orbit families in the intermediate model with a total mass of $M = 10^8 M_{\odot}$ (lower panels) and $M = 5 \times 10^{10}$ (upper panels). The orbital structure is obtained before any regularization to the weights applied. The horizontal axis is dimensionless energy of $\frac{E}{GM/1.0kpc}$, and vertical axis is the integration of mass as a function of energy. The right panel shows the same model applied the regularization of Eq. 3.12.

following quantity:

$$\chi^2 = \frac{1}{N_{cells}} \sum_{i=1}^{N_{cells}} \left(m_i - \sum_{j=1}^{N_{orbits}} w_j O_{ij} \right)^2, \quad \text{with the constraint } w_j \geq 0. \quad (3.10)$$

Furthermore, we introduce the self-consistency parameter δ (Merritt & Fridman 1996) by

$$\delta = \sqrt{\chi^2 / \bar{m}}, \quad (3.11)$$

where \bar{m} is the mean Monte-Carlo mass in cells, $\bar{m} \sim M/N_{cells}$. For a self-consistent model, δ should have a small value close to zero.

In the **left panels** of Fig. 3.3 we show the integration of mass as a function of energy for an axisymmetric model with a mass of $5 \times 10^{10} M_\odot$ (upper left panel) and a triaxial model with a mass of $10^8 M_\odot$ (lower left panel).

We find that for the axisymmetric model (upper left panel, Model 1 hereafter), the short-axis loop orbits make the most important contribution to mass at the low energy levels, and contributed over 40% to the total mass in the end. The box orbits make the second most important contributions at low energy levels and the fraction of mass made up of box orbits increases fast at higher energy, and ends up with 40% of total mass. The chaotic orbits are less important in the Model 1 and only contribute the rest of the mass. There are no long-axis loop orbits here because the model is axisymmetric. In the triaxial model (lower left panel, Model 2 hereafter), more than 40% of the mass stems from the chaotic orbits, while the short-axis and the long-axis loop orbits each contribute slight above 20% of the mass; the box orbits therefore do not play an important role ($\sim 10\%$) in the model. We further like to note that the self-consistency of the model in MOND has been examined in Wang et al. (2008). However, it is unknown whether or not the model is stable. The most direct way to check for the stability and to investigate the evolution N-body of the system is by means of N-body simulation to be elaborated upon in the following sub-section.

Smooth solutions

In order to construct a model where the self-consistency is satisfied accurately, one needs a large number of orbits, often far more than the number of cells N_{cells} where the self-consistency constraints are required (see Eq. 3.10). The best solutions are often NON-unique with a very noisy phase space distribution: $(N_{orbit} - N_{cell})$ zero-weight orbits, plus a N_{cell} orbits with non-zero weights (Merritt & Fridman 1996, Zhao 1996, Rix et al. 1997). However, the mass distributions given by Eq. 3.1 are smooth, and it is desirable to select orbits in a smooth way with less arbitrary weights, i.e. with little oscillations of weights among neighboring orbits in phase space. Introducing a regularisation mechanism allows one to construct a physically more plausible model. Zhao (1996) smoothed the orbits by averaging the weights of the nearest 26 neighbouring orbits when solving the NNLS.

Here we apply a simpler way of regularisation: We minimise the scatter of orbital weights by introducing a smoothing parameter λ , where $\lambda = N_{orbit}^{-2}$ is chosen as in Zhao (1996). The regularisation method used here is very similar to that of Merritt & Fridman (1996), and ensures the least number of orbits with zero weights. Hence the fluctuations of weights become smaller and the contribution of orbits to the mass distribution become smoother. To this end, Eq. 3.10 becomes

$$\chi_{smooth}^2 = \frac{1}{N_{cells}} \sum_{i=1}^{N_{cells}} \left(m_i - \sum_{j=1}^{N_{orbits}} w_j O_{ij} \right)^2 + \lambda \sum_{j=1}^{N_{orbits}} w_j^2. \quad (3.12)$$

The self-consistency parameter becomes

$$\delta_{smooth} = \sqrt{\chi_{smooth}^2 / \bar{m}}. \quad (3.13)$$

Due to the regularisation, the models end up with a larger χ_{smooth}^2 than before smoothing, and therefore the solution loses part of the self-consistency. In Table 3.1 we show the two models we test here: Model 1 is an axis-symmetric model and Model 2 is a generic triaxial model. The fifth line of Table 3.1 shows the self-consistency parameters for the smoothed models, and compared with second line, we find that the regularisation leads to an additional contribution of χ^2 which is on the order of 10^{-5} .

We show the new orbital structures (i.e. the contribution of each type of orbit to the

Table 3.1: Model self-consistency

Model	1	2
Mass (M_{\odot})	5×10^{10}	1×10^8
$a : b : c$	1 : 1 : 0.7	1 : 0.86 : 0.7
δ	1.894×10^{-15}	1.836×10^{-15}
δ_{smooth}	6.592×10^{-5}	7.031×10^{-5}
v_{rms} (km s $^{-1}$)	227.39	29.19
$-2K/W$	0.930	0.951

mass of the systems versus the energy E) in the right panels of Fig. 3.3 for Models 1 and 2. After the regularization, the short-axis loop orbits become even more important in the Model 1 (upper right panel), making an contribution up to 60% of the total mass. The box orbits are less important and contribute about 25% of the total mass. The fraction of mass from chaotic orbits is about 15%. In the triaxial model (lower right panel), the contribution from chaotic orbits and short-axis loop orbits increase slightly, contributing about 50% and 25% to the total mass. The long-axis loop orbits and box orbits become less important here. We can find that the contributions of different types of orbits to the mass ($M(E)$) are smoother in the right panels than those in the left panels.

3.2.4 ICs for N-body systems

In order to study the stability and evolution of the systems, we need to convert the orbits into an N-body model. According to Zhao (1996), the number of particles n_j on the j th orbit is proportional to the weight of the orbit, i.e., for an N particle system there are $w_j N$ particles on the j th orbit. Here we sample the particles on the j th orbit isochronously at $t_j = \frac{T_j}{n_j} \times (i + 0.5)$, $i = 0, 1, 2, \dots, n_j - 1$ where T_j is the total integration time of the j th orbit.³ To this extent we interpolate the positions and velocities from the 6-dimensional output data of the Schwarzschild orbits. We generate

$$n_j = w_j N \quad (3.14)$$

particles on the j th orbit and symmetrize the particles in phase-space: since the density of triaxial model has 8-fold symmetry, which means the density is exactly the same at the

³One can also randomly sample the particles on the j th orbit in a uniform distribution. Since most of the orbits have small positive weights in our simulations, the number of particles on j th are quite small. The random sampling might introduce a numerical noise $\propto \frac{1}{\sqrt{n_j}}$. Therefore the random sampling could have problems to reflect the real shape of the orbit if the weight is small. To be safer, we choose the isochronous sampling.

position (x, y, z) and $(-x, y, z)$, and the other 6 mirrors by changing the signs of x, y and z . We are studying non-rotational systems, hence the angular momentum is zero, and the velocity distribution has 8-fold symmetry as well. In summary, each orbit has $2^6 = 64$ mirrors for a combination of adding a negative sign to each superposition component. The 64 mirrors keep the Initial Conditions exactly symmetric on position and velocity, without rotation. By the symmetrisation the number of particles is $64N$. We then randomly, uniformly select 1×10^6 particles from the large number of particles and keep them as our Initial Conditions of the N-body system.

3.3 N-body simulations in MOND

We use the MONDian N-body code, called NMODY, that has been developed by the Bologna group (Ciotti et al. 2006, Nipoti et al. 2007b, Londrillo & Nipoti 2009). NMODY is a particle-mesh code assigning particles by cloud-in-cell, solving the Poisson's equation on spherical grid and using a second order leap-frog scheme for time integration. The code could be used for Newton simulations as well, by setting the μ function equal to 1. The code has been well tested in Nipoti et al. (2007a): they performed five simulations for a Plummer sphere density distribution for dissipation-less N-body simulations. There are one Newtonian control run (named N), one deep MOND (named D) and three generic (mild) MOND (named M1, M2, M3) simulations in their work. They checked the virial ratio of $2K/|W|$ (Eq. 3.6 in §3.3.2) and quantities K , W and $K + W$, and found that these quantities are conserved after the systems are relaxed, within 10 times of their simulation time unit. Here K is the kinetic energy and W is the Clausius integral (Eq. 3.16). They compared the velocity dispersion σ_r , anisotropic parameter β (Eq. 3.19), line-of-sight velocity dispersion and density distribution obtained in all these five models, and then compared their Newtonian simulation results with the de Vaucouleurs's law (de Vaucouleurs 1948) and other observational laws. The code is also well tested in Ciotti et al. (2006), Nipoti et al. (2007b), Sollima & Nipoti (2010). We will perform a test using other N-body code and compare their results in Appendix B.

3.3.1 Technical Details

In our simulations, we have $N = 1 \times 10^6$ particles for each model, and choose a grid for the numerical integration of Eq. 3.2 with $64 \times 32 \times 64$ cells in the spherical coordinates

Table 3.2: Total simulation times = $120 \times T_{\text{simu}}$.

Model	M	M_{simu}	N-body run duration T	unit time T_{simu}
1	$5 \times 10^{10} M_{\odot}$	$10^{10} M_{\odot}$	0.58 Gyrs	4.8 Myrs
2	$10^8 M_{\odot}$	$10^8 M_{\odot}$	5.8 Gyrs	48.0 Myrs

(r, θ, ψ) , where the radial grids are defined by $r_i = 2.0 \tan[(i + 0.5)0.5\pi / (256 + 1)] \text{kpc}$. The density is obtained via a quadratic particle-mesh interpolation and the time integration is performed by the classical 2_{nd} order leap-frog scheme. The Poisson solver at each time step is using the same algorithm introduced in §2.1. As our time unit for all subsequent plots we use the following definition (cf. Wang et al. 2008)

$$T_{\text{simu}} = \left(\frac{GM_{\text{simu}}}{a^3} \right)^{-1/2} = 4.7 \times 10^6 \text{yr} \left(\frac{M_{\text{simu}}}{10^{10} M_{\odot}} \right)^{-1/2} \left(\frac{a}{1 \text{kpc}} \right)^{3/2}. \quad (3.15)$$

which represents the Newtonian (or Keplerian) dynamical time at the radius of $r = a$ without the factor of 2π . Here we listed the simulation units in Table 3.2. We remind the reader that the parameter T_{simu} is neither the dynamical time nor the orbital time in general MOND simulations. The orbital time in our MONDian systems is defined as the period of the 1:1 resonant orbit in the $x - y$ plane (Wang et al. 2008). Fig. 3.4 shows the periods of circular orbits at different radii for the three models presented here. Fig. 3.4 as well as Eq. 3.15 imply that the MONDian dynamical time at the radius of 1 kpc is about $5T_{\text{simu}}$ for the two models whose masses are $M = 5 \times 10^{10} M_{\odot}$ and $M = 10^8 M_{\odot}$. The simulation mass unit here are $M_{\text{simu}} = 10^{10} M_{\odot}$ and $10^8 M_{\odot}$ for them. We note also that the internal time step used by the code NMODY to integrate the equations-of-motion is $\frac{0.3}{\sqrt{\max|\nabla \cdot \mathbf{g}|}}$, where the factor 0.3 is a typical number used in N-body simulations, and $-\nabla \cdot \mathbf{g} = 4\pi \mathbf{G} \rho_{\text{eff}}$, where ρ_{eff} is the effective dynamical density of the system, i.e. the sum of the baryon and (phantom) dark matter density in the Newtonian force law to produce the gravity or potential of baryons in MOND (see §2 in this thesis, or Wu et al. 2008). The time steps here are determined by the maximum values of $\nabla \cdot \mathbf{g}$, which means the densest dynamical region of the models, where gravity changes most sharply. Note that all particles share a common time step that typically is $(0.005 \sim 0.03)T_{\text{simu}}$.

A flowchart of the technical steps involved in the process prior to the analysis stage can be viewed in Fig. 3.5. This figure summarizes the methodology of how to generate and evolve the N -body systems. In Table 3.2 we present the total times for which each

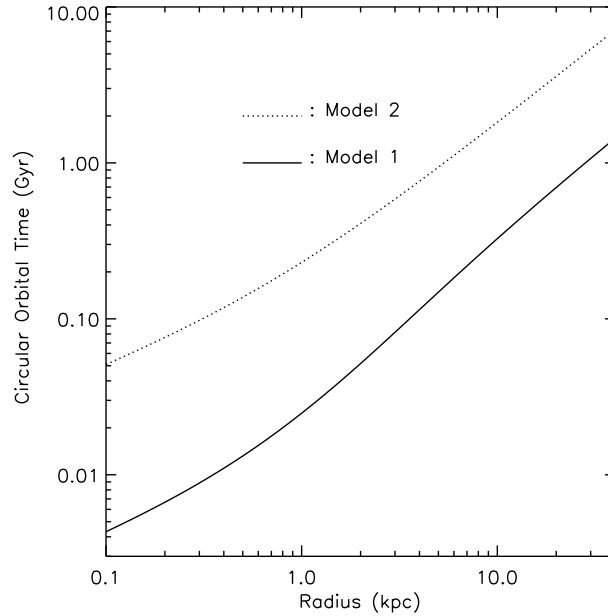


Figure 3.4: The period of circular orbits on the $x - y$ plane as a function of radius. The solid and dotted lines are for models with mass of $5 \times 10^{10} M_{\odot}$ and $10^8 M_{\odot}$, respectively.

system has been evolved.

3.3.2 Virial Theorem

The scalar Virial theorem, $W + 2K = 0$, is valid for systems in equilibrium. Here, W is the Clausius integral,

$$W = \int \rho \vec{x} \cdot \nabla \Phi d^3x, \quad (3.16)$$

and K is the kinetic energy of the system (Binney & Tremaine 1987). In the left panel of Fig. 3.6, we show that the evolution of $-2K/W$ for all models is always about unity, as expected for an equilibrium system. We note that during the first circa five Keplerian dynamical times (1.0 kpc) both systems are moving from a quasi-equilibrium state with $-2K/W \approx 0.93$ to that with $-2K/W = 1.0 \pm 0.07$ afterwards (marginally oscillating about unity). This figure demonstrates that our N -body ICs start off in quasi-equilibrium and then can be considered fully relaxed after approximately five Keplerian dynamical times (1.0 kpc). The Virial theorem is satisfied in our simulations.

These "cold, not fully relaxed" N -body ICs could be attributed to a number of reasons, including the resolution of the simulation and chaotic orbits. Regarding the latter, we need to mention that we compute the orbit library for 100 orbital times, which may not be long

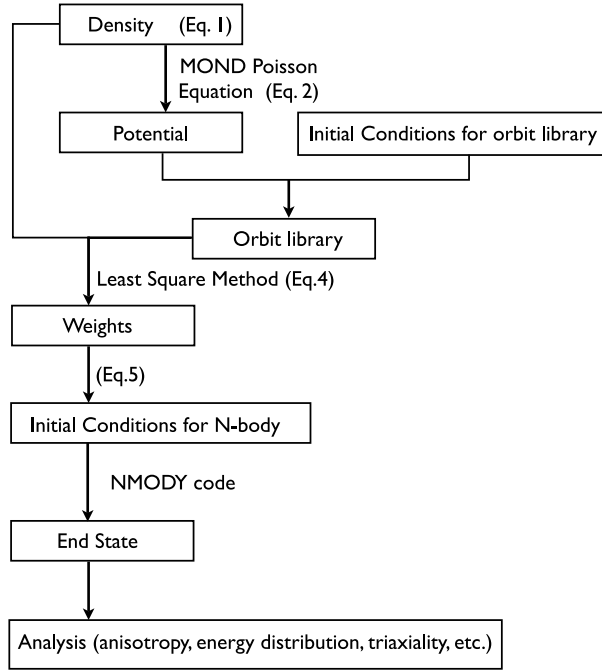


Figure 3.5: Flowchart of the simulations.

enough to ensure a relaxation of those chaotic orbits so as to make sure that they fill the full space. In this case, particles coming from the chaotic orbits could make the N-body system un-relaxed at the beginning.

In Fig. 3.6, we plot the velocity dispersion v_{rms} for both systems as a function of the simulation time unit. The plot indicates that each v_{rms} increases by less than one percent during the relaxation process (within $5 T_{\text{simu}}$) and stays constant afterwards (with tiny variations ($< 1\%$) though).⁴

Note that (as inferred from the right panel of Fig. 3.6) the kinetic energy of the systems increase less than 1% for the maximal evolved case after the relaxation.⁵ Thus, the absolute value of Clausius integral decreases after the relaxation time. That does *not* mean the energy conservation law is broken: $W + K$ is not the total energy of a MONDian system, and it is not conserved either. The total energy is still the conserved quantity, but for a MONDian system it is given by (Bekenstein & Milgrom 1984):

$$E = -L + K. \quad (3.17)$$

⁴There are typos in Wang et al. (2008) about the total mass of models and v_{rms} .

⁵The kinetic energy K is proportional to v_{rms}^2 .

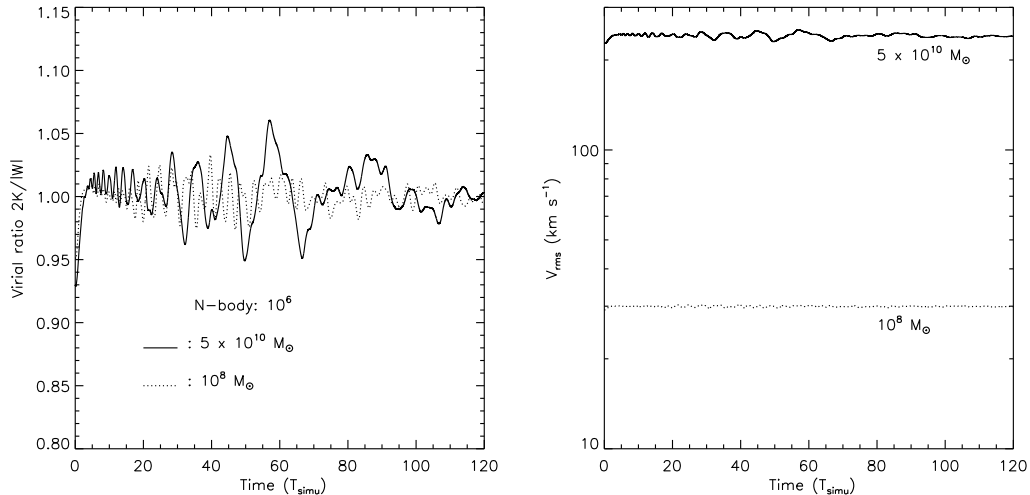


Figure 3.6: The evolution of $2K/|W|$ for all three systems. The solid and dotted lines are for models with mass of $5 \times 10^{10} M_{\odot}$ and $10^8 M_{\odot}$, respectively. The evolution is shown for 120 Keplerian dynamical times (1.0 kpc).

Here, L is the Lagrangian of the MONDian system, defined by (i.e. Eq. 1.10)

$$L = \int d^3r \left\{ \rho \Phi + \frac{1}{8\pi G} a_0^2 \mathcal{F} \left[\frac{(\nabla \Phi)^2}{a_0^2} \right] \right\}, \quad (3.18)$$

where $\mathcal{F}(x^2)$ is an arbitrary function with $\mu(x) = \mathcal{F}'(x^2)$. For an isolated system in MOND, the potential Φ is logarithmic and thus the potential energy is infinite. Therefore, the only meaningful quantity is the difference in energies between different systems (Bekensstein & Milgrom 1984, Nipoti et al. 2007a). However, the evident evolution of $W + K$ at the very beginning (i.e. the first 5 Keplerian dynamical times (1.0 kpc)) shows that the N -body ICs are not accurately in equilibrium, and hence referred to as quasi-equilibrium.

3.3.3 Energy Distribution

One of the characteristic quantities to describe relaxation processes is the so-called differential energy distribution, i.e. the quotient of mass dM over the energy band interval $[E, E + dE]$ (Binney & Tremaine 1987). The energy of a unit mass element is $E = \frac{1}{2}v^2 + \phi(\vec{x})$, where ϕ is logarithmically infinite in MOND and hence all particles are bound. But since the absolute value of potential energies is meaningless, we can define the zero point as the last point of the radial grid. Hence, there are positive relative energies for part of the particles though all of them are bound to the system.

The left panels of Fig. 3.7 show the evolution of $\frac{dM}{dE}$ over 120 Keplerian dynamical times (1.0 kpc) for two models (upper panel: Model 1; lower panel: Model 2) and we find that all distributions are rather similar. And the most pronounced evolution of the energy distribution is at the low- E end, where particles are most strongly bound to the system.

Both of the differential energy distributions have 19 peaks, as can be seen in left panels of Fig. 3.7. This is due to the energy definition of the Schwarzschild technique outlined in §3.2.3: Inside every sector, the energy (kinetic plus potential energy) is a constant, while the outer shell is the zero-velocity surface of this sector. The adjacent two sectors have energy jumps at the shell. Therefore there are 19 ‘quantized energy levels’ for our models. For each model, there are no mass distributions outside these 19 constant ‘energy levels’ and hence they appear as ‘valleys’ in the left panels of Fig. 3.7. That explains why the curves appear noisy.

We note that after the initial relaxation of about five Keplerian dynamical times (1.0 kpc)⁶ the low- E end of the distribution becomes devoid of particles, i.e., particles are leaving the central regions where the potential well is deepest. This actually hints at a possible flattening of the initially present density cusp $\gamma = 1$! We return to this issue later in sub-section 3.3.5.

Comparing the two left panels in Fig. 3.7, we observe that the system in the mild MOND regime (i.e. the model with a mass of $5 \times 10^{10} M_{\odot}$: upper-left panel) has the most significant evolution, whereas the model in deep MOND evolves less (lower-left panel). We therefore conclude that our ICs are most stable for the deep MOND regime.

As seen in the right panels of Figure 3.7, the cumulative energy distribution clearly confirms the previous conclusion from the differential distributions. For Model 1, after the relaxation, the mass in the inner region escapes to the outer, while the outer part is nearly unchanged. The mass distribution obviously does not evolve after relaxation.

⁶Even though we do not show the curves for 5 Keplerian dynamical times (1.0 kpc) we acknowledge that the drop happens during that initial relaxation phase. Here we care about the long-term evolution within 120 Keplerian dynamical times (1.0 kpc) and hence decided to rather focus on the late evolution of the systems.

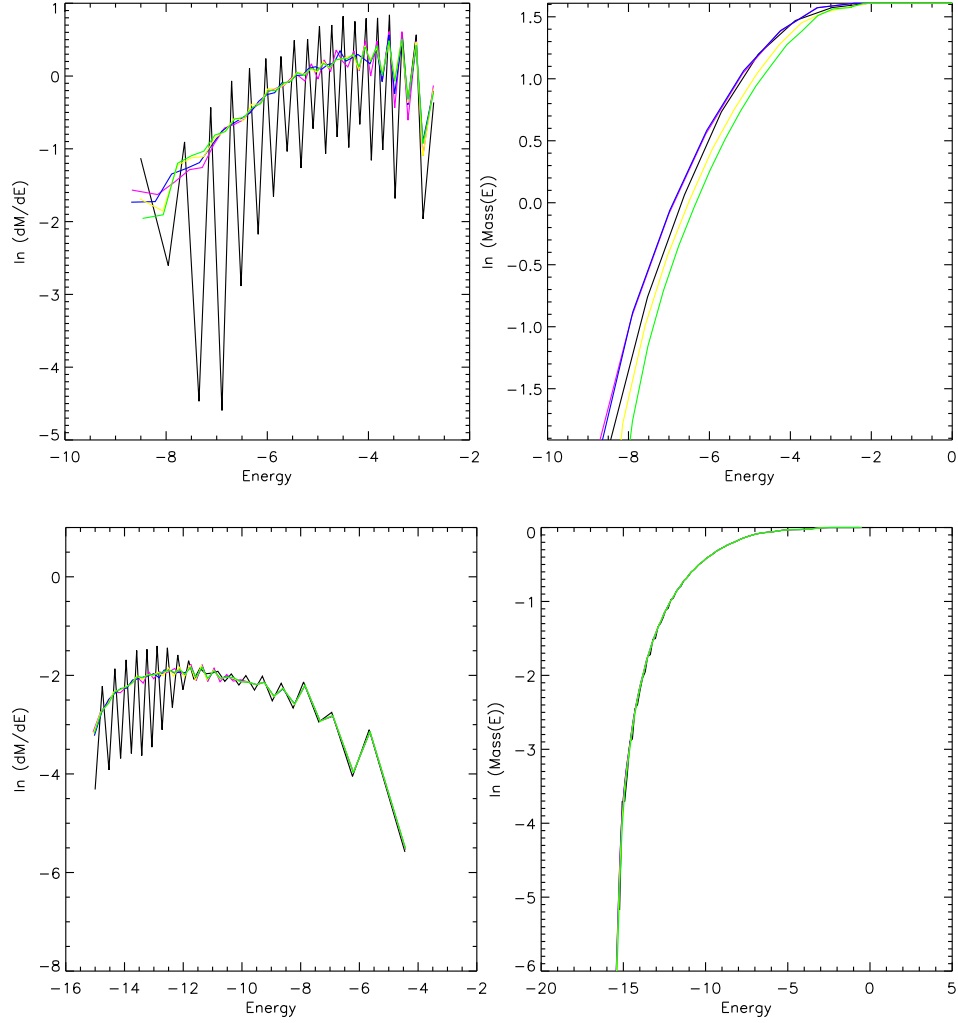


Figure 3.7: **Left panels:** Evolution of the differential energy distribution $\frac{dM}{dE}$. The panels (from upper to lower) correspond to our models with total mass of $5 \times 10^{10} M_{\odot}$ and $10^8 M_{\odot}$, respectively. **Right panels:** The cumulative energy distribution. The black lines denote the ICs, and the violet, blue, yellow and green lines show the differential energy after 30, 60, 90, 120 Keplerian dynamical times (1.0 kpc). Both $\frac{dM}{dE}$ and the Energy are given in units where $G=1$ and $M=1$.

3.3.4 Kinetics

To further check upon the stability of our systems, we calculate the radial velocity dispersion profiles $\sigma_r(r)$ as well as the anisotropy parameter

$$\beta(r) \equiv 1 - \frac{\sigma_\theta^2 + \sigma_\psi^2}{2\sigma_r^2}. \quad (3.19)$$

Here r is the spheroidal radius, as in Eq. 3.1, and $\sigma_\theta, \sigma_\psi$ are the tangential and azimuthal velocity dispersions.

The results can be viewed in the left panels of Fig. 3.8. We find that, for both models, σ_r increases approximately 5% from $r > 0.4$ kpc during the relaxation at the beginning of the simulation, i.e. the first five Keplerian dynamical times (1.0 kpc) (though not shown for clarity). Afterwards, there is only very little evolution noticeable. The majority of the galaxy ($0.4 \text{ kpc} < r < 10 \text{ kpc}$), the $\sigma_r(r)$ approximately has $\sigma_r(r) \propto r^{-0.25}$ relation for the mild-MOND model (Model 1), while for the deep MOND the trend is slowly decreasing, almost can be considered as a constant $\sigma_r(r)$ in $0.4 \text{ kpc} < r < 10 \text{ kpc}$. At large radii the $\sigma_r(r)$ is constant for Model 1, while it has big oscillations for Model 2. Looking at the $\sigma_r(r)$ of Model 2, if we consider that the decrease is also a slow oscillation of the velocity dispersion versus radius, the whole $\sigma_r(r)$ can be considered as a constant (with moderate oscillations). The slope of $\sigma_r(r)$ oscillates around a constant value of approximately 20 km/s.

The reduction of σ_r in the core means that the ICs are slightly colder in the radial direction to sustain equilibrium.

We also present the anisotropy parameter $\beta(r)$ in the right panels of Fig. 3.8. The evolution of β with time again confirms that the models are stable (after the relaxation). The mild-MOND model has a slowly increasing β , it is 0.2 at the centre and 0.4 at large radius (40 kpc). This means the regulation conditions in Eq. 3.12 prefer a more isotropic velocity dispersion. In the centre the model is more isotropic than in the outer parts. For the deep MOND model, it is even more isotropic at all radii. Although the β for model 2 has a different trend compared to Model 1, the anisotropy is quite small in overall, $\beta \leq 0.2$. In the centre of the model, the β is around 0.1, and has a peak of 0.2 nearby 1 kpc. Then the β turns down again, and at 10 kpc is around 0. On the lower left panel, the σ_r has

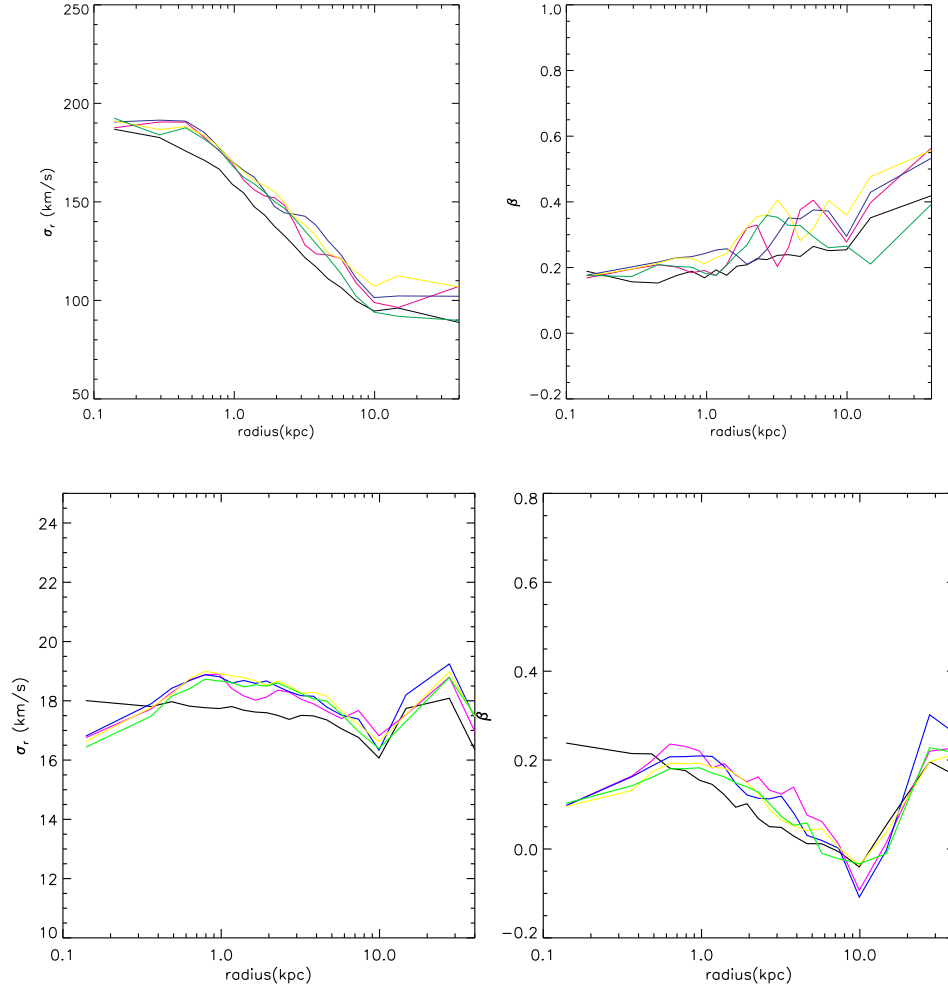


Figure 3.8: **Left panels:** Evolution of the radial velocity dispersion $\sigma_r(r)$. **Right panels:** Evolution of the velocity dispersion anisotropy $\beta(r)$. The **upper** and **lower panels** are corresponding to models of $M = 5.0 \times 10^{10} M_{\odot}$ and $M = 1.0 \times 10^8 M_{\odot}$. The ordering of the panels corresponds to Fig. 3.7 as does the colouring of the lines.

a valley, around 16 km s^{-1} at the same radius. The $\beta(r \sim 10 \text{ kpc}) \sim 0$ means at the luminous edge of the dwarf galaxy, the velocity dispersion is isotropic. It has a second peak at large radius of 40 kpc (This is more theoretically interesting than observable).

Compared with the Newtonian analytical Hernquist models (Baes & Dejonghe 2002), their velocity dispersion has a $\sigma_r \propto r^{-0.35}$ relation in $1 - 10 \text{ kpc}$ when $\beta = 0.25$. This trend shows that MOND models have different radial velocity distribution from that in Newton Gravity. The mild-MOND model has -0.25 power law while the deep MOND is almost $\sigma_r(r) \propto r^0 \sim \text{constant}$.

3.3.5 Mass distributions

Due to the stable quantities discussed above, we would expect that the mass densities are also stable at the same time. Indeed, we find this conclusion from the Fig. 3.9, where we show the densities along the major axis (**left panels**) and cumulative (**right panels**) mass distributions for our MOND models. With regards to the density panels, the two models show a similar behavior. It is clear that the mass and density are quite stable. The density curves are oscillating close to the initial analytical density (the smooth black line in left panels, the noisy black line is the initial numerical density) as given by Eq. 3.1 due to the numerical noise. We also note that the density becomes slightly smaller at large radii for Model 2, which means that some particles inflow to the centre. However this does not noticeably change the density distribution. Hence the density distribution remains stable after the system is in equilibrium, and there is no obvious evolution within 120 Keplerian Dynamical times (at the typical scale $a = 1.0 \text{ kpc}$).

The right panels of Figure 3.9 show the total mass inside the ellipsoid radius r . The black dashed straight lines in right panels are defined by $M_0 = \frac{a_0 r^2}{G}$, the mass to produce the gravity acceleration a_0 in a point mass approximation. M_0 is the watershed between the MOND and Newton regions. At a certain radius r , when the enclosed mass is smaller than M_0 , there occurs a transition to MONDian gravity. We find that in all of the three models MONDian effects cannot be ignored. Even for $5.0 \times 10^{10} M_\odot$, the MONDian gravity dominates the regions of $r > 7 \text{ kpc}$. Obviously, the model $M = 1.0 \times 10^8 M_\odot$ is in deep MOND region. The colours show the evolution of the systems. The accumulated mass versus radius is stable, which is consistent with the density distribution.

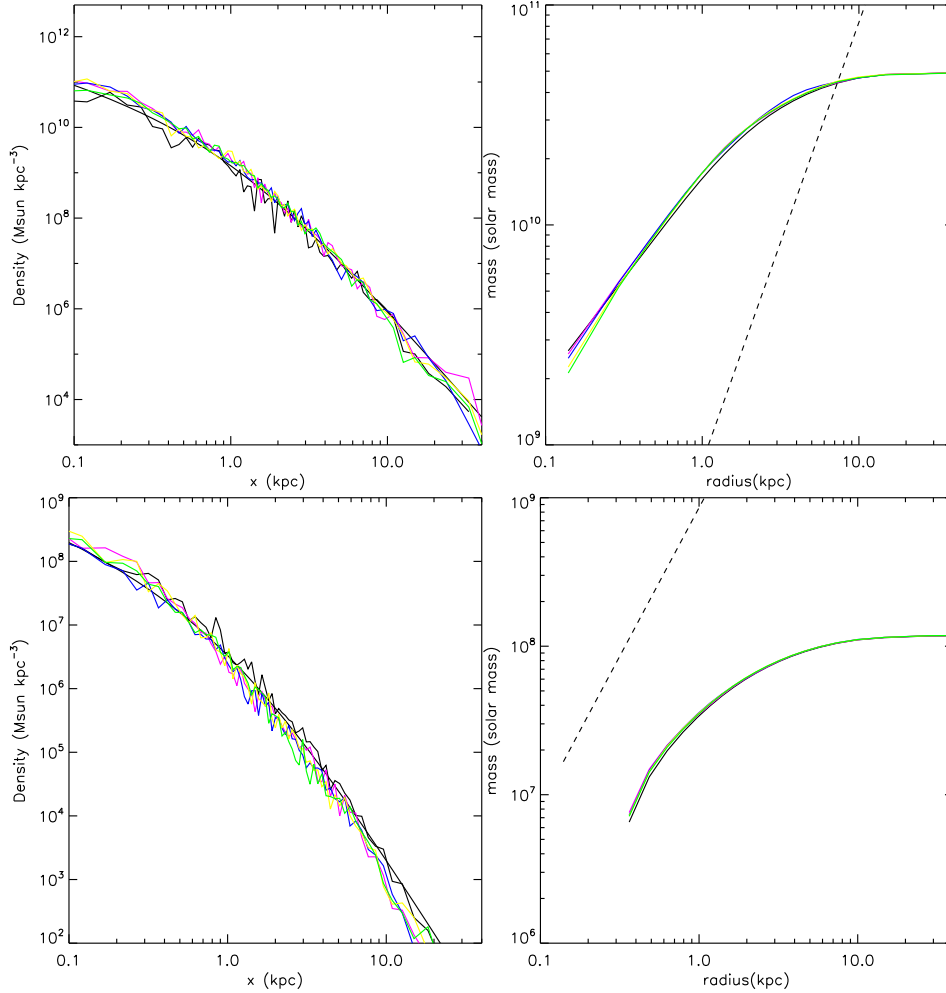


Figure 3.9: The evolution of the mass distribution for the models with $M = 5 \times 10^{10} M_{\odot}$ (upper) and $M = 10^8 M_{\odot}$ (lower). The **left panels** show the density distributions on the major axis the density information can be obtained from the axis ratios of Figure 3.10. The **right panels** show the accumulated mass inside the radius r . The dashed black lines in the **right panels** are defined as $\frac{a_0 r^2}{G}$, which are the watersheds of enclosed mass producing MONDian dominating gravity (below the lines) and Newtonian dominating gravity (upon the lines). The colouring of the lines is representative of the evolutionary stage of the model and corresponds to Fig. 3.7.

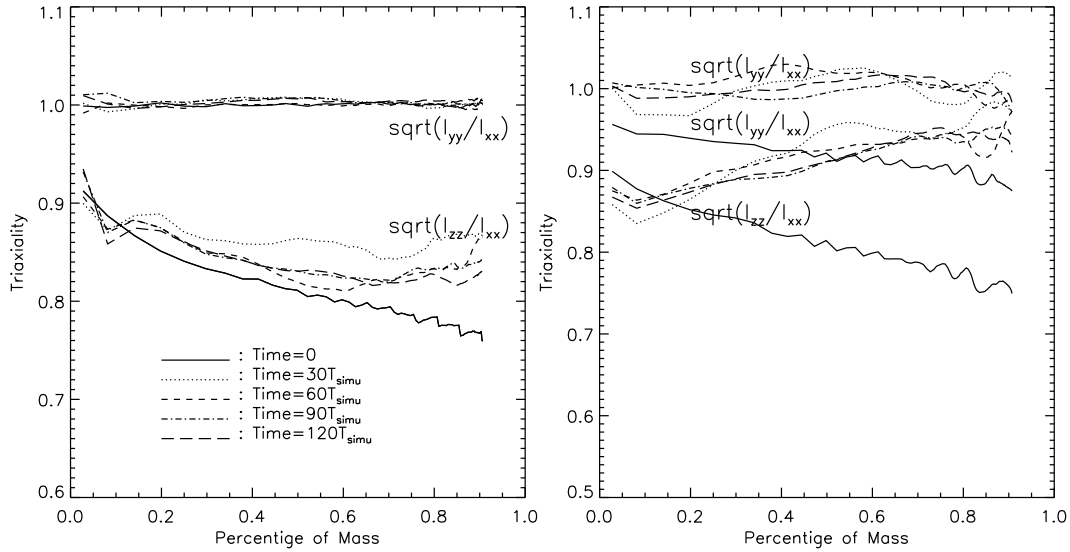


Figure 3.10: Evolution of axis ratios with the median model of a total mass of $5.0 \times 10^{10} M_{\odot}$ (left panel) and $1.0 \times 10^8 M_{\odot}$ (right panel). The lower and upper series of lines are for the ratios of minor : major axis and intermediate : major axis, i.e., $\sqrt{I_{zz}/I_{xx}}$ and $\sqrt{I_{yy}/I_{xx}}$. The different line symbols are defined the same as in the figure: solid, dotted, short dashed, dot-dashed and long dashed lines are for system evolving 0, 30, 60, 90 and 120 T_{simu} , where T_{simu} is the Newtonian orbital time at 1.0 kpc .

3.3.6 Shape

§3.3.5 shows that the density along x-axis and the accumulated mass do not evolve significantly. Another question arises whether the shape (i.e., the initial triaxiality) remains stable or changes. To address this, we show the evolution of the axis ratios of the diagonal components $\sqrt{I_{yy}/I_{xx}}$ and $\sqrt{I_{zz}/I_{xx}}$ of the Mean Square Length (MSL) where

$$\begin{aligned} I_{xx} &= \frac{1}{M} \int dx dy dz \rho(x, y, z) x^2, \\ &= \frac{1}{N_p} \times \sum_{i=1}^{N_p} x_i^2 \end{aligned} \quad (3.20)$$

in Fig. 3.10, and likewise for I_{yy} and I_{zz} . The MSLs are not exactly the real axis ratios (to be defined as the ratio of the semi-axes for the isodensity contours) of the systems, but they are among the quantities to describe the shapes of the models.

For the ICs of the N-body simulations, the initial MSL ratios (solid lines in Fig. 3.10) are not the same as the the initial axis ratio: $\sqrt{I_{xx}} : \sqrt{I_{yy}} : \sqrt{I_{zz}} = 1 : 1 : 0.76$ for the enclosed 90% of the total mass for Model 1, and $\sqrt{I_{xx}} : \sqrt{I_{yy}} : \sqrt{I_{zz}} = 1 : 0.88 : 0.75$ for the

enclosed 90% of total mass for Model 2. Note that the initial MSL ratios are not constants with radius (i.e. with the radius enclosing certain percent of the total mass). Except for the axisymmetric model, the $\sqrt{I_{xx}} : \sqrt{I_{yy}} = 1 : 1$ is exactly the axis ratio $a : b = 1$, for the other initial MSL ratios (solid lines in the figures), they have similar behaviour: the ratios are large in the centre (where enclosing small amount of mass) and they decrease to smaller values with the enclosing mass. However these ratios are not stable and they evolve quickly to their stable position: for model 1 the $\sqrt{I_{xx}} : \sqrt{I_{yy}} : \sqrt{I_{zz}} = 1 : 1 : 0.85$ and for Model 2 the $\sqrt{I_{xx}} : \sqrt{I_{yy}} : \sqrt{I_{zz}} = 1 : 1 : 0.95$ for 90% mass of the systems. It is clear that the MSLs prefer being more spherical. The MSLs quickly evolve to the above mentioned ratios and then they appear stable (no significant evolution with time afterwards). Note that their final ratios are not constants at all radii. In Model 1 the $\sqrt{I_{zz}} : \sqrt{I_{xx}}$ remains at the initial value (0.9) at small fraction of mass, and then decreases to 0.85. In Model 2 it is different: the $\sqrt{I_{xx}} : \sqrt{I_{yy}} = 1 : 1$ at all radii and the $\sqrt{I_{zz}} : \sqrt{I_{xx}}$ is 0.88 at the centre and increases to 0.95 at the 90% enclosing mass.

We also show the MSL components of the systems' enclosing 90 % of mass ($r < r_{90\%}$) versus time in left panels of Fig. 3.11. Here $r_{90\%}$ is the radius of the system containing 90% of the total mass. We find that there is a significant oscillation at $50T_{simu}$ for Model 1. For Model 2, the components of MSL imply that the shape of the model becomes oblate after $50 T_{simu}$.

A study of the tensor kinetic energies K_{xx} , K_{yy} and K_{zz} , defined as $K_{xx}(r < r_{90\%}) = 0.5 \langle v_x \cdot v_x \rangle$, shows a stable behaviour to the MSL analysis presented above (right panels of Fig. 3.10). Note that for Model 1, there is also an oscillation at $50T_{simu}$. Converted to the circular time of the system, it is the circular time for orbits at the typical length scale $r = 1$ kpc (Fig. 3.4) for this model. The bottom right panel shows that for Model 2, the kinetic energy $K_{xx} = K_{yy}$ which implies the velocity and the mass have the trend to become axisymmetric distribution.

It is not very surprising that the I_{xx} components can change with time. Various study of Schwarzschild modeling under the Newtonian Gravity show that the mean semi-axis can evolve in the following N-body simulations (Smith & Miller 1982, Merritt & Quinlan 1998).

As a final note, considering existing Schwarzschild plus N-body simulations in the

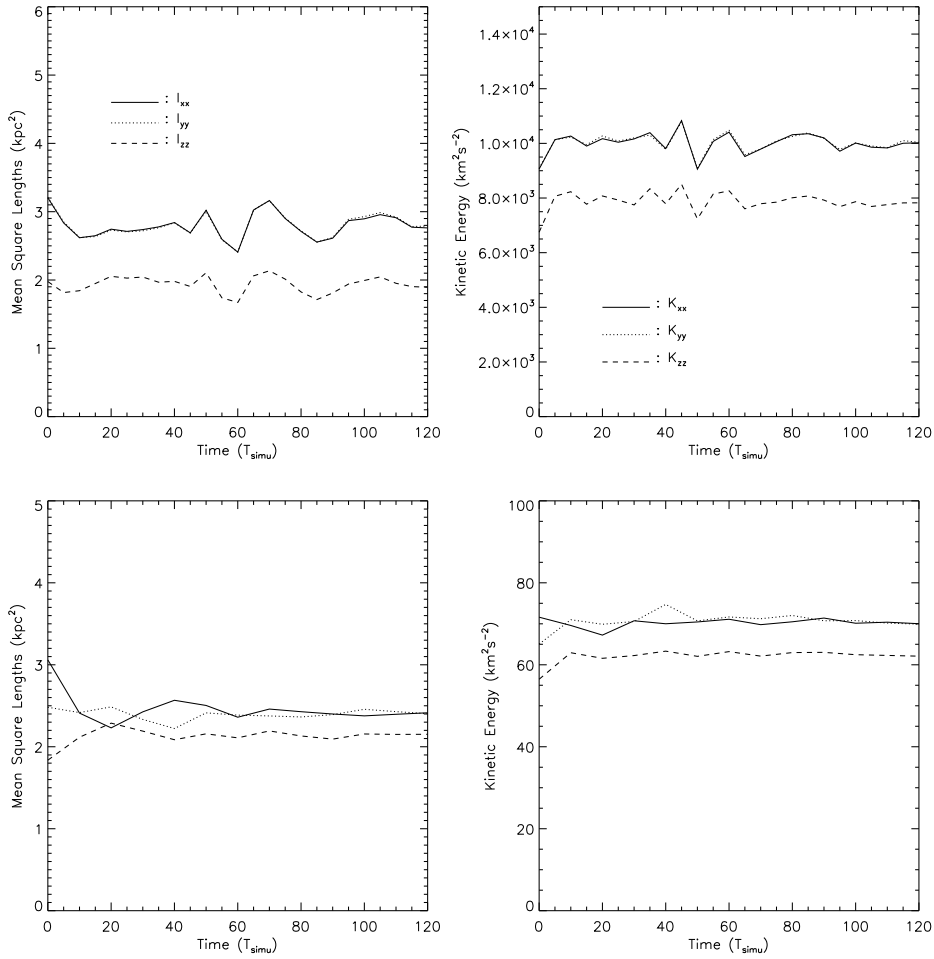


Figure 3.11: Upper and lower panels are different mass models of $5 \times 10^{10} M_{\odot}$ and $10^8 M_{\odot}$. The left panels are the evolution of the inertial tensor I_{xx} (solid line), I_{yy} (dotted) and I_{zz} (dashed). The right panels are the evolution of kinetics energy K_{xx} (solid), K_{yy} (dotted) and K_{zz} (dashed). The total simulation time is 120 T_{simu} .

literature, we find that the evolution seen in our MONDian cuspy elliptical models is comparable to that seen in Fig.5 of Poon & Merritt (2004, ApJ 606, 774) for triaxial ellipticals in Newtonian gravity.

3.4 Conclusions and Discussion

We explored the stability and evolution of the triaxial Dehnen model (Dehnen 1993, Merritt & Fridman 1996, Capuzzo-Dolcetta et al. 2007) with a $\gamma = 1$ central cusp using MOND. We utilized the Schwarzschild method (Schwarzschild 1979) to build orbit models which were in turn used to generate initial conditions (ICs) for N-body simulations using the method outlined in Zhao (1996). These ICs were evolved forward in time for 120 Keplerian dynamical times (at the typical length scale of 1.0 kpc) by the numerical integrator NMODY developed by the Bologna group (Ciotti et al. 2006, Nipoti et al. 2007a, Londrillo & Nipoti 2009) and designed to include the effects of MOND. We additionally ran the same simulations with a second MONDian gravity solver AMIGA (Llinares et al. 2008, cf. Appendix B) based upon an entirely different grid-geometry to confirm the credibility of our results.

In our simulations, the virial theorem was satisfied at all times. We showed that the systems start in quasi-equilibrium with a short relaxation phase of approximately less than five Keplerian dynamical times (1.0 kpc). We found that our models are stable: the virial ratios are satisfied and such quantities as the energy distribution, the density and accumulated mass distribution, the radial velocity dispersion, the anisotropic parameter, and the energy do not have significant evolution with time. We need to note that MSLs of the systems change after the relaxation time, and then stay stable in the course of the simulations; while the axis ratios of the diagonal components of the MSL (as well as the kinetic energy tensor) appear stable with time afterwards.

To further check the credibility of our results and the dependence on the code, we ran the simulations again with a technically substantially different code (AMIGA), which is also capable of integrating the analog to Poisson's equation (cf. equation 3.2 in Appendix B). The results are practically indistinguishable reassuring their validity.

We like to close with the reminder that our systems are isolated systems, corresponding to the cases of field galaxies. The self-potentials of the systems in MOND are logarithmic

at large radii, therefore no stars can escape from such systems. However, for any system embedded in external fields, the potential is truncated when the strength of the external field becomes comparable to the internal field (Milgrom 1984, Wu et al. 2007). Therefore, Poisson's equation should be modified to (also see Eq. 1.37)

$$\nabla \cdot \left[\mu \left(\frac{|\nabla\Phi_{int} - \vec{g}_{ext}|}{a_0} \right) (\nabla\Phi_{int} - \vec{g}_{ext}) \right] = 4\pi G\rho_b, \quad (3.21)$$

where the μ -function is determined by both the internal *and* external gravitational accelerations. Hence the strong equivalence principle is violated: the μ -function has different values along and against the directions of external field even though the mass density distribution is the same. A direct result is that the potentials become non-symmetric along and against the directions of the external field, i.e., a symmetric system is not in equilibrium due to the asymmetry of the self-potential. Therefore, MOND predicts that there are no real symmetric systems within the external gravity backgrounds. This will be explored in greater detail in §4.

4

Stability and Evolution of Galaxies in External Fields

Elliptical galaxies widely exist in the universe, either isolated or embedded in clusters of galaxies, and they have compact centres. The elliptical galaxies inside galaxy clusters are very interesting systems to test modified Newtonian dynamics (MOND). Apart from the central brightest cluster galaxy, other galaxies experience a strong gravitational influence from the other galaxies of the cluster. This influence manifests itself only as tides in standard Newtonian gravity, meaning that the systematic acceleration of the center of the mass of the galaxy has no consequence. However, in the context of MOND, a consequence of the breaking of the strong equivalence principle is that the systematic acceleration changes the own self-gravity of the galaxy.

In the previous chapter §3 we constructed equilibrium models via the Schwarzschild's approach (Schwarzschild 1979, 1982), and further studied their stability. Those models in §3 are isolated, and in the MOND gravity. The aim of this chapter is to construct

equilibrium models for elliptical galaxies in the external fields, i.e. for galaxies embedded in clusters, using the framework of MOND (Milgrom 1983b, Bekenstein & Milgrom 1984). This is achieved by the same numerical tools (Schwarzschild’s method) discussed in §3. We construct a series of Hernquist models, which represent medium-mass elliptical galaxies with mild cusps within a galaxy cluster, providing a MONDian external field on the order of $g_{\text{ext}} \approx a_0$. In addition, the dynamical properties and stability of these systems are studied with the help of N-body simulations.

We find that the Schwarzschild models are not in rigorous equilibrium. After a short phase of virialisation, however, the models appear stable. The outskirts of the galaxies develop lopsided shapes along the external field’s direction during 60 simulation times (Newtonian Keplerian times at scale length of 1kpc) after which the models seem to settle to a stable equilibrium. Meanwhile, the centroid of the galaxy, defined by the outer density contours, is shifted by a few hundreds parsecs with respect to the densest point. Non-detection of such effects for large samples of galaxies with good photometry inside clusters could be used to falsify the modified gravity interpretation of the MOND phenomenology.

The chapter is organized as follows: In §4.1.1, we shall discuss the lopsidedness of galaxy potentials embedded in external fields. After that we will apply Schwarzschild’s technique to construct models of such galaxies in §4.1.2, and test the stability and evolution of the obtained systems in §4.1.3. At the end of this section, we compare our results to the evolution of isolated galaxies, and find that the models appear stable as well. Due to the presence of the external field, however, the outskirts of the galaxies become lopsided, corresponding to a slow (secular) evolution at large radii. In §4.2, we will further study the violation of the symmetry of cluster galaxies and the offsets centroids between the centroids of the galaxies’ inner and outer contours.

4.1 The Stability of Galaxies in Uniform External Fields

In contrast to the Newtonian case, the internal dynamical properties of a gravitating system in MOND are always affected by the presence of an external background field, i.e. even a freely falling system in MOND will exhibit a dynamical evolution different from that of an isolated one. This attribute implies a violation of the strong equivalence principle (SEP), which is usually referred to as the external field effect (see §1.2).

In what follows, we shall only consider external fields which are uniform and constant. Although our assumption yields a less realistic scenario for a galaxy cluster environment because of neglecting tidal effects, it is still useful to investigate the internal dynamics of galaxies within this simplified framework. Our approach can be justified as follows: In both Newtonian gravity and MOND, an external tidal field will have an influence on the system’s internal dynamics. Therefore, the presence of tidal fields would obscure fundamental differences between the two frameworks caused by the SEP violation inherent to MOND, acting as some kind of “noise”. To maximally distinguish between Newtonian and MONDian dynamics, we thus ignore tidal effects in our analysis.¹ Such an idealised case corresponds to systems moving in a slowly, smoothly varying background field, for example, a galaxy circularly orbiting the cluster centre. In these situations, the impact of the external field is mainly dominated by its uniform part, tidal effects play only a subordinate role.

It is quite challenging to build equilibrium models of elongated or triaxial systems for further examination of their dynamical behaviour and evolution. Due to the occurrence of a non-linear Poisson’s equation, it is quite complex to solve the Jeans equations and build equilibrium models in MOND. This is especially true for systems embedded in external fields because the phase distribution of such systems is determined by both internal density and external field. In their galaxy merger simulations, Nipoti et al. (2007b) obtained the distribution function (DF) of a Hernquist sphere by Eddington inversion in a MONDian potential. For more complex triaxial models, however, this is quite challenging and it is generally not possible to obtain analytic solutions to Eddington’s equation. Tiret & Combes (2007, 2008) employed Newtonian equilibrium models for spiral galaxies embedded into a dark halo modelled by a Plummer profile, and continued with replacing the gravitational effects of the dark halo by MONDian dynamics. Similarly, the simulations by Hagi et al. (2009) made use of Newtonian equilibrium models initially, but then the velocities of particles were increased to avoid gravitational collapse when modelling globular clusters embedded in Milky Way external fields. When applied to N -body simulations, however, these ICs will immediately relax until the particle system has reached a new state of equilibrium. It is important to note that MOND cannot be exactly reproduced by

¹Generally, it is desirable to have a full treatment of the problem including tidal effects. This would allow to explore other, more complex scenarios such as evolution in fast-varying backgrounds, e.g. a galaxy crossing the centre of cluster, and will be addressed in future work.

switching to Newtonian gravity and taking additional particles into account; in some cases the phantom density, i.e. the effectively generated density by MOND, can be negative, a phenomenon which would require negative-mass particles (Milgrom 1986, Wu et al. 2009). Schwarzschild’s approach provides another powerful way of constructing equilibrium ICs for N -body simulations directly in MOND, which has been already studied for isolated systems (Wu et al. 2009). Here we will follow this approach. Note that the Schwarzschild’s approach is designed for equilibrium systems, however the models in external fields are not in exact equilibrium. These models are in quasi-equilibrium and will relax to a new equilibrium state. Hence the initially axisymmetric/triaxial models will have self-evolution and relax to asymmetric shapes. We construct the symmetric ICs to study how much they self-evolve. There are several reasons to build the symmetric ICs:

- The lopsidedness of cluster elliptical galaxies in MOND is a new topic, and not much work has been done. We have no idea about the exact in-equilibrium-shapes of systems before the study. We do not even know if there are any self-consistent solutions for those systems.
- Even in a strong external field of $1 a_0$, the external field starts to dominate the dynamics of the system at a radius around 10 kpc. Thus we expect the asymmetric ICs are close to equilibrium, and the self-evolution will not destroy the models.

4.1.1 MOND, mass models and static potentials

For the baryonic density, we adopt the Hernquist profile (Hernquist 1990b), i.e. the $\gamma = 1$ profile of Dehnen (1993), (Eq. 4.1)

$$\rho(r) = \frac{M}{2\pi abc} \frac{1}{r(1+r)^3}, \quad (4.1)$$

where

$$r = \sqrt{\left(\frac{x}{a}\right)^2 + \left(\frac{y}{b}\right)^2 + \left(\frac{z}{c}\right)^2}, \quad (4.2)$$

and the constants a, b, c are the typical length scales of the galaxy’s major, intermediate and minor axes, respectively. We choose three different galaxy models: two axisymmetric elliptical galaxies with (which is the Model 1 in §3) and without external field, respectively, and a triaxial galaxy model embedded in an external field. The parameters of the galaxy models are listed in Table 4.1. These models represent medium-sized elliptical galaxies

Table 4.1: Parameters of the galaxy models

Model	M ($10^{10}M_{\odot}$)	Axes ratio	EF (a_0)	Direction of EF
1	5	1:1:0.7	1.0	x - z diagonal
2	5	1:1:0.7	0	-
3	10	1:0.86:0.7	1.0	x -axis

with masses on the order of $10^{10} - 10^{11}M_{\odot}$, being bright enough to observe the outer parts. In this case, the internal accelerations are comparable to several a_0 . Considering that galaxies should sit on the fundamental plane, there is a strong correlation between stellar masses M and effective radii R_e (Figure 13 of Gadotti (2009)). The effective radii of galaxies with a total mass of $10^{10} - 10^{11}M_{\odot}$ range from 0.5–3 kpc. For all three models, we set $a = 1$ kpc which lies in the R_e dispersion range of observational data points (Gadotti 2009). The strength of the external fields is chosen as $1a_0$, hence the internal and external accelerations at several R_e (about 10 kpc to the galactic centre) are comparable to each other.

We compute the static potential using a numerical MONDian Poisson solver which has been developed by the Bologna group (see §2.1 Nipoti et al. 2007a,b). We adopt a resolution of $n_r \times n_{\theta} \times n_{\phi} = 512 \times 128 \times 256$ on a spherical grid, where the grid segments are defined as

$$r_i = 2 \tan [(i + 0.5)0.5\pi/(n_r + 1)] \text{ kpc}, \quad (4.3)$$

$$\theta_j = \pi \times (j + 0.5)/n_{\theta}, \quad (4.4)$$

$$\phi_k = 2\pi \times k/n_{\phi}, \quad (4.5)$$

with $i = 0..n_r$, $j = 0..n_{\theta} - 1$, and $k = 0..n_{\phi} - 1$. In §2 we showed that the internal potentials are prolate in the direction of the external field. This effect becomes important when the internal and external fields are roughly of the same order; an even more significant effect occurs at weak acceleration, external field dominated regions where $|\vec{g}_{int}| \ll |\vec{g}_{ext}| \ll a_0$. In this case, we find that the potentials are not only prolate (along the external field direction), but also appear distorted. Figure 4.1 shows the contours of isodensity and isopotentials for Model 1 as listed in Table 4.1. The contours correspond to radii of 2, 5, 10, 15, and 20 kpc along the major axis. We can easily identify a distortion of the potential along the direction of the external field at large radii, $r \sim 10$ kpc, where internal and external field are comparable. Note however that the density contours are

still axisymmetric.

For a simplified view on this, let us consider a spherically symmetric system embedded into an external field. Integrating the MOND Poisson's equation (Eq. 1.38 in §1.2.1), we arrive at the following expression (Bekenstein & Milgrom 1984):

$$\mu\left(\frac{|\vec{g}|}{a_0}\right)\vec{g} = \vec{g}_N + \vec{\nabla} \times \vec{h}, \quad (4.6)$$

where g_N is the Newtonian gravitational field, and $\vec{\nabla} \times \vec{h}$ is a solenoidal vector field determined by the condition that \vec{g} can be expressed as the gradient of a scalar potential. Restricting ourselves to the axis parallel to the external field's direction, \vec{g} and \vec{g}_N must be either parallel or anti-parallel, assuming that the symmetry centre coincides with the coordinate origin. Hence the curl term $\vec{\nabla} \times \vec{h}$ vanishes. The strength of the total gravitational acceleration $g = |\vec{g}|$ along the negative semi-axis in the external field's direction, i.e. where the external field cancels part of the internal one, is $g^- = |g_{ext} - g_{int}|$ while on the positive semi-axis it is $g^+ = g_{int} + g_{ext}$. Thus the two different sides have different values of the μ -function at the same radii, leading to a larger MONDian enhancement of gravitation along the negative semi-axis. Clearly, for the underlying spherically symmetric density distribution, the potential and its derivatives are axisymmetric. Note however that, applied to a generic triaxial system, the result is approximately the same. For an external field pointing into an arbitrary direction, such a system has no symmetries anymore, but the curl term in Eq. 4.6 only accounts for corrections on the level of 10% (Brada & Milgrom 1995).

Returning to the situation in Model 1, the axisymmetric model, Fig. 4.1 confirms the above analysis. On the left panel, the isopotential contours are denser in the first quadrant than in the third one. The internal potential is shallower in the first quadrant where $g^+ = |g_{ext} + g_{int}|$, and steeper in the third quadrant where $g^- = |g_{int} - g_{ext}|$. As can be seen from the right panel of Fig. 4.1, the lopsidedness of the potential reaches its maximum at roughly 10 kpc where the external and internal fields are comparable to each other. The semi x-axis ratio $r^- : r^+$ of the isopotential contour is up to 1.14 between 10 and 11 kpc. At small radii ($r < 3$ kpc), the internal gravitational field dominates, and thus the $r^- : r^+$ is basically 1. At larger radii ($r \gg 10$ kpc), the relative contribution of the external field increases, and the $r^- : r^+$ falls down to 1 again because the μ -function

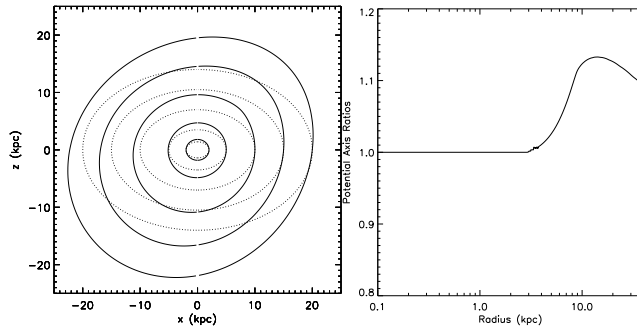


Figure 4.1: **Left panel:** Isodensity (dotted) and isopotential (solid) contours of Model 1. The isodensity contours correspond to ellipsoidal radii of 2, 5, 10, 15, and 20 kpc. The isopotential contours are located at the same radii along major axis. External field is on the negative x-z diagonal direction. **Right panel:** The ratio of isopotentials evaluated at the same radius in anti-parallel and parallel direction of the external field, $(r_- : r_+)_{\Phi(r_+)}$, for Model 1.

approaches a constant, $\mu = \mu(|\vec{g}_{ext}|/a_0)$.

4.1.2 Schwarzschild Technique and Model Self-consistency

Schwarzschild’s method (Schwarzschild 1979, 1982) has been introduced in §3.2.3.

Integration of orbits

We use an orbital integration code which adopts a 7/8 order Runge-Kutta method (Fehlberg 1968) to ensure the accuracy of the orbits (Wang et al. 2008). The way we divide the spatial grid is exactly the same as in (Wang et al. 2008) (also see Wu et al. (2009) for numerical details). Here we highlight the *different treatments* to our present models:

The grid segmentation is the same for the first octants as in §3.2.3. Thus we have in total $16 \times 3 \times 21 = 1008$ equal mass cells excluding the outermost sector. The outermost 48 cells are not taken into account because the sector’s boundaries extend to infinity. Since the density evolves as $\rho \sim r^{-4}$ at large radii, the orbits in this sector should contribute much less than all other orbits, and thus they are negligible. In §3, we ignored the two outermost sectors, thus there were only 912 cells in the models. Here we only dispose of the last sector because in the external fields the outskirts of galaxies might extend to larger radii. In addition, our available hardware has improved a lot, allowing us to consider the very diffuse outskirts.

In §3 we considered isolated triaxial models. Due to the three-folded symmetry, they took only the first octant into account, and then symmetrised the O_{ij} by reflecting all

Table 4.2: Galaxy model and Schwarzschild parameters

Model	1	2	3
M [$10^{10} M_{\odot}$]	5	5	10
$a : b : c$	1: 1: 0.7	1: 1: 0.7	1: 0.86: 0.7
EF [a_0]	1.0	0	1.0
Direction of EF	negative x - z diagonal	-	negative x -axis
Density symmetry	axisym	axisym	triaxial
Potential sym. Axes	y	x, y, z	y, z
Starting octants	I, II, V, VI	I	I, II
Reflecting planes	x - z	x - y , x - z , y - z	x - y , x - z
N_{cells}	3840	960	1920
$N_{stationary}$	15360	3840	7680
$N_{ejecting}$	12000	3000	6000
N_{orbits}	27360	6840	13680

orbits at the octant's boundaries, i.e. the x - y , x - z , and y - z planes. We shall use the same approach for Model 2.

Note that due to the presence of an external field, the symmetry of the resulting potentials is broken, therefore we cannot simply reflect the orbits at these planes anymore. For Model 3, the external field points into negative x -direction, and thus orbits starting from the positive x semi-space are not the mirror of orbits of those starting from the negative x semi-space, i.e. orbits on different sides of the y - z plane behave differently. However, orbits will still have a two-folded symmetry with respect to the x - z and x - y planes. Hence we used the first ($|x|, |y|, |z|$) and second ($-|x|, |y|, |z|$) octants to calculate orbits for Model 3. The total number of cells in this case is set to $960 \times 2 = 1920$, the outermost 96 cells are again excluded.

When the external field is pointing into an arbitrary direction, the symmetry of the model is further reduced. Switching to an axisymmetric model and forcing the external field to point into a direction perpendicular to the symmetry axis (see Model 1 in Table 4.1), however, we can always find a coordinate frame such that the external field is parallel to the x -axis. As the potential will be distorted along the external field direction, we lose the symmetry along the x -axis in addition to the one along the z -axis. However, the potential will still be symmetric with respect to the x - z plane, which can be exploited to simplify the numerics. We fold the system at the x - z plane and consider four octants, the first ($|x|, |y|, |z|$), second ($-|x|, |y|, |z|$), fifth ($|x|, |y|, -|z|$) and sixth ($-|x|, |y|, -|z|$), calculate orbits by reflecting them at the x - z plane. In this case, we have $960 \times 4 = 3840$

Table 4.3: Model self-consistency and equilibrium

Model	1	2	3
N_{orbits}	27360	6840	13680
δ	4.33198×10^{-2}	1.894×10^{-15}	1.19292×10^{-2}
δ_{smooth}	4.33199×10^{-2}	6.592×10^{-5}	1.19302×10^{-2}
$v_{rms}(\text{km s}^{-1})$	230.31	227.39	325.31
$-2K/W$	0.966	0.930	0.965
$L_c(\text{km s}^{-1} \text{kpc})$	259.4	265.9	370.5

mass cells (the outermost 192 cells are excluded) dividing the semi-space. Note that if the system is triaxial and the external field direction does not coincide with one of the axes, we will need to consider all eight octants individually, using $960 \times 8 = 7680$ cells. Since this is computationally quite demanding, we shall limit ourselves to axisymmetric systems (Model 1) and a triaxial system where the external field is anti-parallel to the x -direction.

With the ICs introduced in §3.2.3, one can generate most of the orbits in full phase space (Schwarzschild 1993) for a given potential. The starting points of the orbits for Model 2 are the same as in Wu et al. (2009); for Model 3, we add mirror positions in the second octant, and for Model 1, we use four mirror octants as mentioned above. In Table 4.2, we summarise the ICs for the two models, where $N_{stationary}$ and $N_{ejecting}$ are the numbers of the starting points. Note that with a higher number of cells and orbits, both the size of the array O_{ij} and the linear system 3.4 increase, and building the orbit library becomes computationally more expensive as will be specified below.

All the orbits are integrated for 100 circular orbital times T_{cir} . In Fig. 4.2, we plot the circular orbital time against the radius for all three models, using logarithmic scaling. The circular orbital times of Model 1 and Model 2 start to differ from each other at about 6 kpc. While the slope of Model 2 is approaching 1 at large radii, those of Models 1 and 3 are approaching 3/2. For Model 1, this is due to the fact that the circular velocity for an isolated MOND model is a constant at large radii, $v_c = (GMa_0)^{1/4}$, hence $T_{cir} \propto r$. In the case of strong external fields, however, the interpolating function μ becomes constant far from the system, leading to Newton-like behavior of $T_{cir} \propto r^{3/2}$. For a self-consistent model, the value of self-consistency parameter δ (defined in Eq. 3.11, without the regularization) quickly decreases with an increasing number of orbits, and will be very close to zero if a large number of orbits is adopted.

The **left panels** of Figure 4.3 show the integrated contributions of orbits (for energies

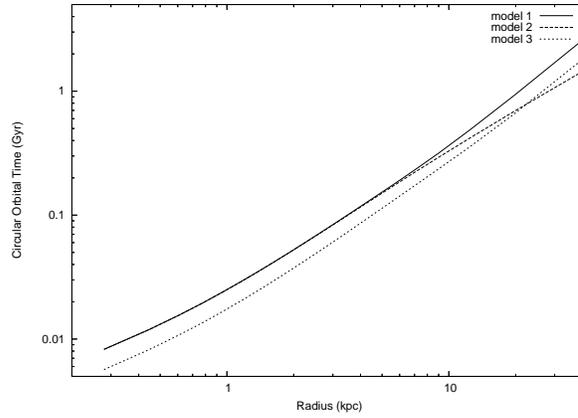


Figure 4.2: The circular orbital time in units of Gyr against radius in units of kpc, using logarithmic scaling: The solid, dotted and dashed lines represent Models 1, 2 and 3, respectively.

$< E$) to the system's mass. The individual contributions of long-axis loop (green), short-axis loop (bright blue) orbits, box (dark blue lines) orbits and stochastic (purple lines) orbits are plotted against the energy E . The orbits are classified in §3.2.3. For Models 1 and 2, we find that short-axis loop orbits provide a large mass fraction, making up almost half of the model's total mass. There appear to be no long-axis loop orbits in the isolated case (Model 2), but their abundance slightly increases if the external field is applied (Model 1). In case of a strong external field, stochastic orbits constitute the second largest orbit family accounting for up to 40% of the total mass while box orbits contribute less than 10%. Looking at low energy levels, the fraction of box orbits is almost zero. Comparing to the isolated model (Model 2), chaotic orbits are much less important than box orbits at all energy levels, and their fraction at low energies is nearly zero. Loop (including short-axis and long-axis loops), box and chaotic orbits account for approximately 45%, 40% and 15% of the total mass. For the triaxial model with external field (Model 3), however, these contributions significantly change. The results for Model 3 show that the main mass component corresponds to chaotic orbits making up over 90% of the total mass. This is something surprising since that in Newtonian Gravity, it has been proved that a galaxy constructed completely by chaotic orbits is not self-consistent (Merritt & Fridman 1996). The two families of loop orbits are the least important components with mass fractions of almost zero at all energy levels. Considering the total fraction of chaotic orbits for all three models (15% for the isolated axisymmetric model, 40% for the axisymmetric model with external field, and over 90% for the triaxial model with external field), we conclude

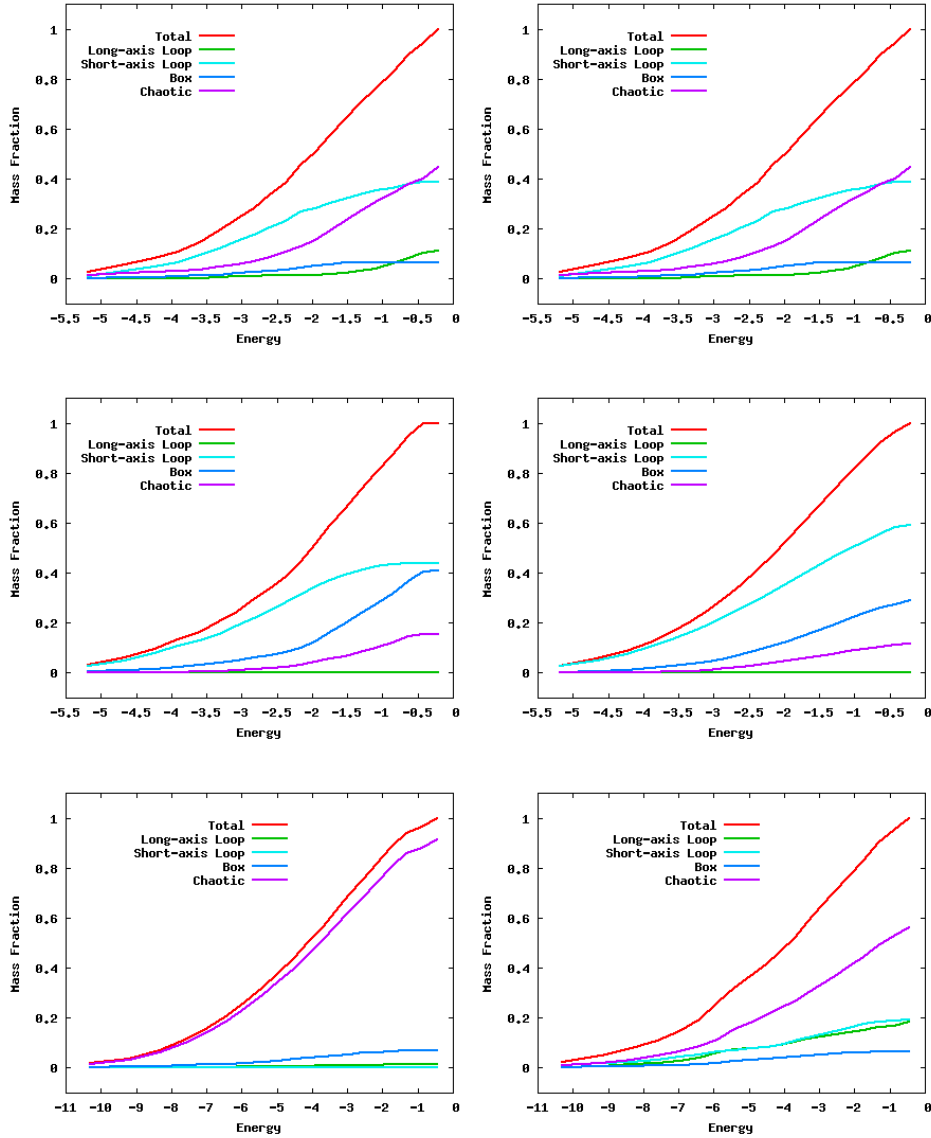


Figure 4.3: Left Panels: The integrated contributions of different orbit families (for energies $< E$) to the mass as a function of energy for Models 1 (upper panel), 2 (middle panel) and 3 (lower panel), assuming Eq. 3.10, i.e. without smoothing. **Right Panels:** The integrated contributions (for energies $< E$) of different orbit families to the mass as a function of energy for Models 1 (upper panel), 2 (middle panel) and 3 (lower panel), assuming the regularisation in Eq. 3.12, i.e. with smoothing.

that chaotic orbits become important for less symmetric systems.

Smooth solutions

We used the same regularization as discussed in §3.2.3. Due to the regularisation, the models end up with a larger χ^2 (defined in Eq. 3.12) than before smoothing, and therefore the solution loses part of the self-consistency. The third line of Table 4.3 shows the self-

consistency parameters $\delta_{smooth} = \sqrt{\chi^2}/\bar{m}$ (\bar{m} is the mean Monte-Carlo mass in cells) for the smoothed models, and compared with second line, we find that the regularisation leads to an additional contribution of χ^2 which is on the order of 10^{-5} .

In Table 4.3, we list the δ_{smooth} of all models. We find that the isolated model is self-consistent, however, the parameters for models in external fields exhibit a worse degree of self-consistency. The δ values for Model 1 and Model 3 are on the order of 10^{-2} , which can be explained as follows: The mass distribution reconstructed by orbits in the lopsided potential are distorted in the outer part, the density becomes lopsided and does not accurately reproduce the analytic density profile.

The **right panels** of Figure 4.3 show the integrated contributions (for energies $< E$) of orbit families to the total mass after regularisation. We find that after smoothing, the amount of chaotic orbits decreases, especially in Model 3. At low energies, loop orbits (including short-axis and long-axis loops) even contribute half of the total mass fraction while chaotic orbits contribute the other half. In total, chaotic orbits account for approximately 55% of mass which is much smaller than before regularisation (90%). Long-axis and short-axis loop orbits contribute nearly 20% each compared to their zero contribution before smoothing.

Computing hardware

The parallelised Schwarzschild programme has been run on the HUYGENS supercomputer at SARA in Amsterdam. The system is equipped with IBM 4.7GHz Power6 processors. We used up to two nodes for the simulation of models, each node consists of 16 dual core processors and has a total memory of 128Gb. The total CPU time was 2400, 600 and 1200 core hours for Models 1, 2 and 3, respectively. While the construction of the orbits library was not really memory demanding, the NNLS routines needed about 8, 2 and 4 Gb of memory to store the massive arrays, and the complete run took around 50, 3 and 12 hours for Models 1, 2 and 3, respectively.

4.1.3 N-body and stability

It is unknown whether a quasi-equilibrium model constructed from Schwarzschild's approach is stable. The direct way to test the stability and evolution is using N-body tools.

Due to the external field, the potentials of axisymmetric density profiles are lopsided, and orbits running in these potentials also become lopsided. For an arbitrary orbit integrated in a given potential for long enough time, the mass reproduced by this orbit is also lopsided. Thus the uncertainty on the model’s stability increases in this case. It is an important issue to investigate the stability of MOND models in external fields since there are many elliptical galaxies observed in clusters. In what follows, we test the stability and evolution of the previously introduced models, starting with the N-body ICs given by Schwarzschild’s approach.

Initial conditions and N-body code

We follow Zhao (1996) and §3.2.4 to generate the ICs for N-body simulations. Note that our models exhibit special symmetries which significantly decrease the amount of computing work (Table 4.2). Also, as the NNLS programme selects hundreds of non-zero weighted chaotic orbits which have not completely relaxed within 100 circular orbital times, the systems’ symmetries in phase space are broken when placing particles on chaotic orbits. Therefore we need to consider additional mirror particles in phase space, with the “mirrors” being the corresponding reflecting planes of our models (see again Table 4.2). In the simulations, we use 10^6 particles for each model after considering the symmetrisation.

The ICs generated by Schwarzschild’s technique are in quasi-equilibrium, therefore the scalar virial theorem should be approximately valid, i.e. the ICs should satisfy $W+2K=0$, where W is the Clausius integral defined in Eq. 3.16 and K is the kinetic energy of the system (Binney & Tremaine 1987). We listed the virial ratios $-2K/W$ and the root mean square velocities of the ICs in Tab. 4.3. We find that $-2K/W = 1 \pm 0.1$ for all three models. All models are “colder” where the virial ratios are smaller than 1. The errors could be resulting from noise in chaotic orbits which have been integrated for 100 Keplerian orbital times and may not have finish relaxation yet. Since the ICs are in quasi-equilibrium, we can apply them in N-body codes for testing the stability.

All results presented in this section were obtained by evolving our systems forward in time using the N-body particle-mesh code NMODY (Ciotti et al. 2006, Nipoti et al. 2007a, Londrillo & Nipoti 2009). The NMODY code has been introduced in §3.3. Since the inclusion of the external field is achieved by means of suitable boundary conditions, the incorporated Poisson solver does not need to be substantially altered, and can be easily

adapted to our purposes. We now use a grid resolution of $n_r \times n_\theta \times n_\phi = 1500 \times 64 \times 64$ (a much higher radial resolution than that in §3, because there is an external field in Models 1 and 3, some high energy particles can escape to far away) in spherical coordinates (r, θ, ϕ) , where the radial grid segments are defined as

$$r_i = 8.0 \tan[(i + 0.5)0.5\pi/(n_r + 1)] \text{ kpc}, \quad (4.7)$$

and the other two remaining grid segments are the same as in § 4.1.1. The time unit used in the code T_{simu} is given by Eq. 3.15 in §3.3.1. The quantity $2\pi T_{\text{simu}}$ has the physical meaning of one Keplerian time at a radius of $r = a$, and the system has total mass of M given in units of $M_{\text{simu}} = 1.0 \times 10^{10} M_\odot$.

It is well known that the typical size of clusters of galaxies is on the scale of several Mpc, and the central regions where there exist strong and nearly uniform gravitational backgrounds are much smaller. To give a rough estimate, the size is one order of magnitude smaller than the size of the cluster, which is around 0.1Mpc. Galaxies are accelerated in an almost constant field at this scale. Converted into a physical time scale where this approximation holds, this gives around $60T_{\text{simu}} \sim 0.28\text{Gyrs}$. Of course, real galaxies are accelerated in an inhomogeneous external field. However, inhomogeneous fields are still too complex to be modeled in such environments, and most of the physics we are interested in at the moment can be explored in a constant background. Thus we simulate our models for a time interval of $60 T_{\text{simu}}$. More details about the time steps used in the code are further discussed in §3.3.1. The N-body simulations take around 260, 400 and 400 hours for all three models on a single processor of the supercomputer, using approximately 15700, 19200 and 20000 time steps, respectively, for $60 T_{\text{simu}}$. We further simulate our models for a longer time interval of $120 T_{\text{simu}}$ (double of the $60 T_{\text{simu}}$), to see if the systems are stable after the simulation time interval we shall perform here. We only show the $120 T_{\text{simu}}$ simulations for the virial ratio of the models.

Figure 4.4 shows the evolution of the virial ratio $2K/|W|$ within $120 T_{\text{simu}}$. At simulation start, the virial ratios of all the three models are around 0.94, and rapidly increase to values near 1 within three simulation times. This implies that the N -body ICs constructed via the Schwarzschild technique are not fully virialised. After relaxation, the virial ratios are oscillating around 1 for all three models, with the oscillation amplitude

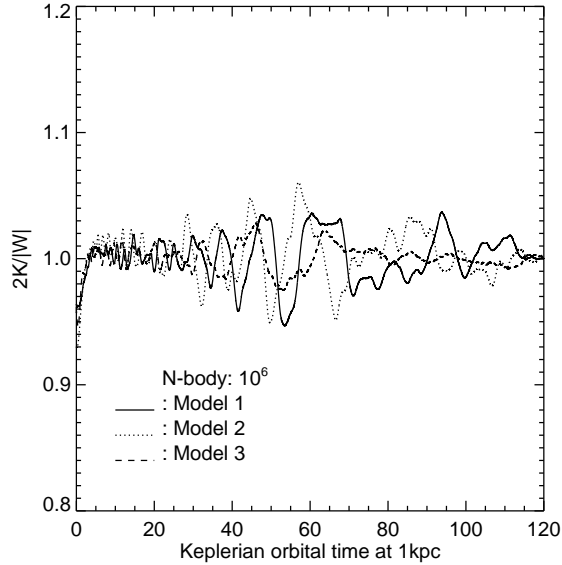


Figure 4.4: Evolution of the virial ratio: The solid, dotted and dashed lines are representing Models 1, 2 and 3, respectively.

being roughly 0.02. Hence we conclude that the virial theorem is valid for all considered models. Starting at $30 T_{simu}$, we notice a gradually increasing oscillation amplitude, which does not seem physical, but is likely related to numerical noise. In Fig. 4.4, we can find the oscillation amplitude decreases after $65 T_{simu}$ for all the models, hence the increasing oscillation amplitude within $60 T_{simu}$ is not a sign of instability but numerical noise.

Mass distribution

Due to presence of the external field, the potential becomes lopsided. Hence the mass density will redistribute inside the total potential until the density with its associated (internal) potential reaches an equilibrium configuration. In the following, we want to address the question of how far-reaching this evolution in the external field is.

The left panels of Fig. 4.5 illustrate the radii $r(M)$ enclosing different fractions of the total mass M , increasing from 10% to 90% in steps of 10%. For all three models, all mass radii are very stable, showing only tiny oscillations within 60 simulation times. Although basically starting from the same density profile, the galaxy’s edge of Model 1 (defined by the radius enclosing 90% of the total mass) is about 30% larger than that of Model 2. Moving to smaller enclosed mass radii, we observe a similar, but increasingly softened effect. For instance, the half mass radii of Models 1 and 2 are 2 kpc and 1.7 kpc ,

respectively. The external field leads to a slightly bigger system size compared to the isolated model, which is already manifest at the level of construction. The same behaviour can be observed in the case of Model 3.

The right panels of Fig. 4.5, show the models' density distribution along the galaxies' major axes. Apparently, the density profiles do not significantly change during the simulation. For Models 1 and 3, however, we note that the density is slightly decreasing at larger radii ($r > 10$ kpc). The found result is consistent with the left panels of Fig. 4.5 where the "expansion" effect becomes significant at a scale of about 10 kpc. The small increase of the systems' size appears as a direct consequence of the external field which changes both depth and shape of the underlying potential. Clearly, all orbits integrated in the potential are affected by this change, and the same applies to the generated ICs for our simulations. Since the relatively large values of the parameter δ ($\sim 1\%$) listed in Table 4.3 are mainly due to contributions from the models' outer parts ($r \gtrsim 10$ kpc), we conclude that the observed effect is originally caused by the lower level of self-consistency, but also remains a stable characteristic of the system throughout the simulation.

Note that there are fewer symmetries for Models 1 and 3, and thus there are fewer mirror particles in phase space. Such a situation could lead to a self-rotation of the models which cannot be canceled due to the lack of counteracting mirror particles. This is especially true for the outer regions where the impact of the external field starts to become important. In §4.1.4, we will further comment this issue.

Kinetics

From §4.1.3, we already know that the outer regions (defined by shells enclosing a certain fraction of the total mass) of the galaxy models embedded into an external field are slightly expanded compared to the isolated case. Additional information on these models can be obtained by exploring their properties in full phase space. To study the dynamical evolution of our systems, we calculate the radial velocity dispersion $\sigma_r(r)$ and the anisotropy parameter

$$\beta(r) = 1 - \frac{\sigma_\theta^2 + \sigma_\phi^2}{2\sigma_r^2}, \quad (4.8)$$

where r is defined in Eq. 4.1 and σ_θ , σ_ϕ are the tangential and azimuthal velocity dispersions, respectively.

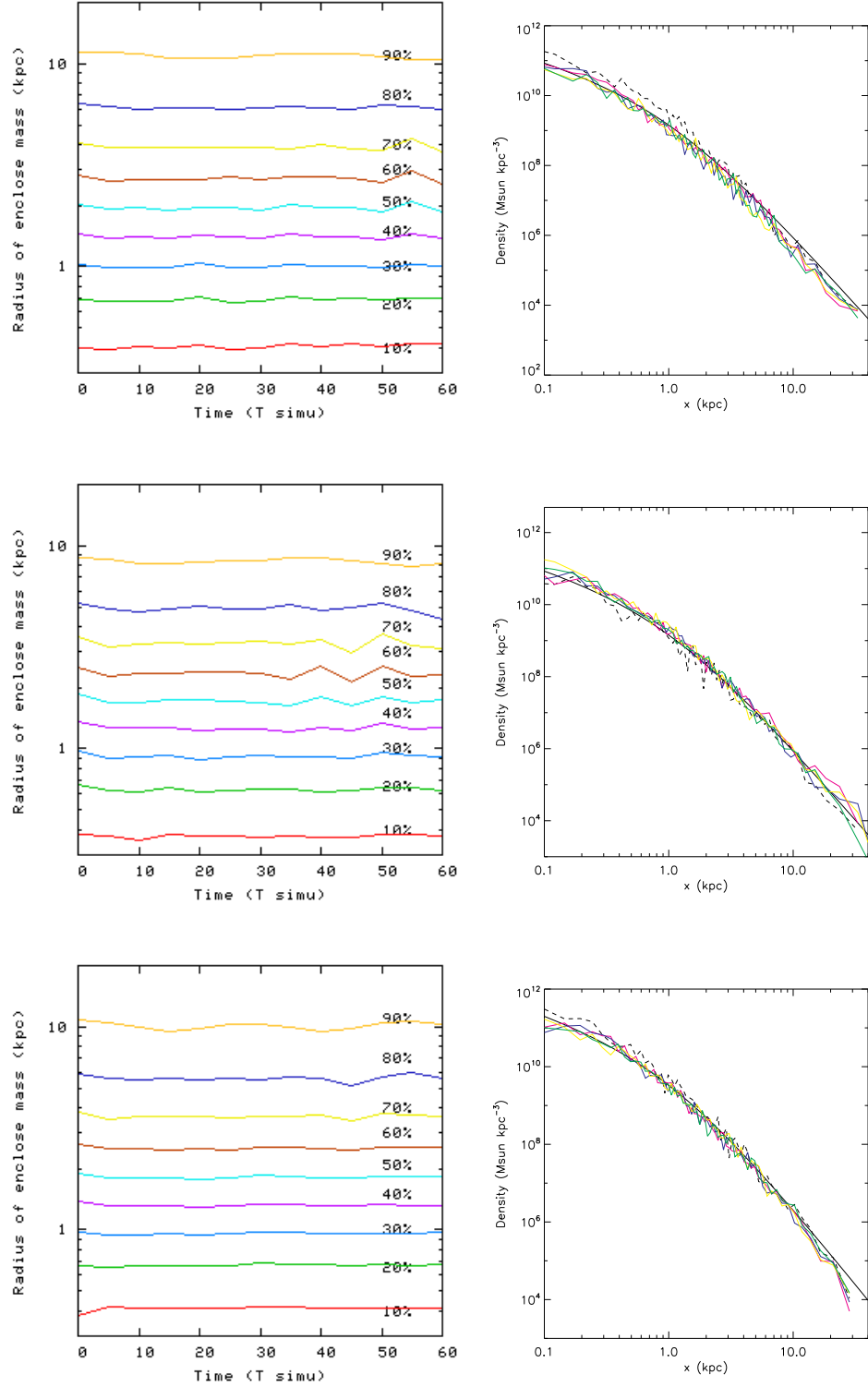


Figure 4.5: **Left panels:** The evolution of radii enclosing certain fraction of mass. The upper, middle and lower panels show the results for Models 1, 2 and 3, respectively. **Right panels:** Density distribution along the galaxies' major axes. The analytic initial density and the density constructed from N particles correspond to the black solid and dashed lines, respectively. The colours represent different periods during the simulations. The violet, blue, yellow and green lines correspond to evolution times of 15 , 30 , 45 and $60T_{simu}$, respectively.

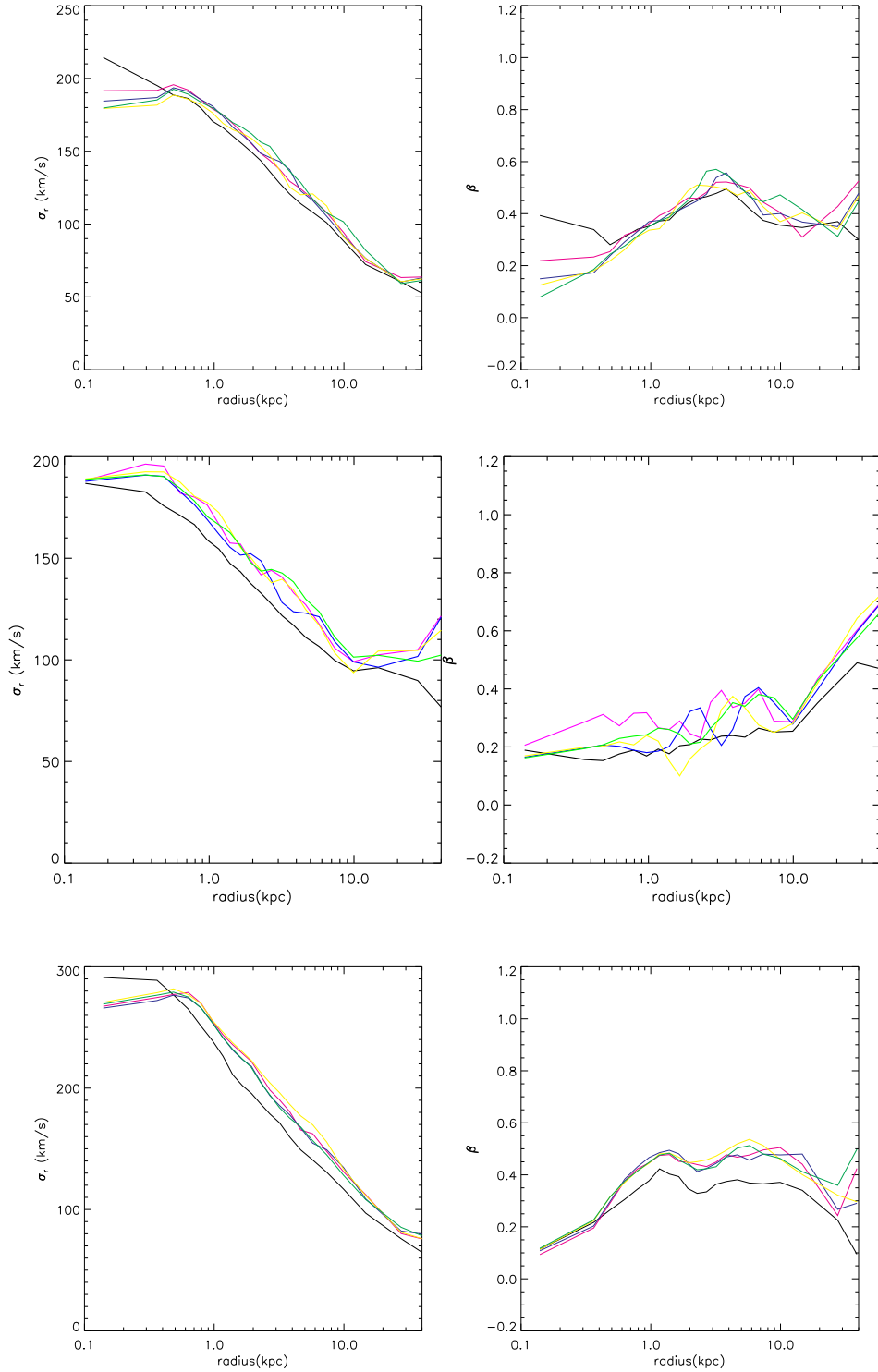


Figure 4.6: **Left panels:** The time evolution of the radial velocity dispersion. The upper, middle and lower panels show the results for Models 1, 2 and 3, respectively. **Right panels:** The anisotropy parameter β . The black lines represent the ICs and different colors are defined the same as in Fig.4.5.

The left panels of Fig. 4.6 show the time evolution of the radial velocity dispersion σ_r . Obviously, all models start off in a quasi-equilibrium state and reach a stable state after a short relaxation phase at the very beginning. In addition, we find that the outer parts of all systems become more radial after the virialisation process. Surprisingly, the models in external fields (i.e. Models 1 and 3) exhibit less evolution than the isolated Model 2. The values of σ_r in the inner region of these models, however, experience a decline after their virialisation. For all three models, the velocity dispersion is flattened in the inner region, approximately inside 0.5 kpc. The discrepancy between IC and the final equilibrium state is caused by the resolution of the numerical simulations and has been explicitly discussed in § 3.3.4. In the case of Model 2, we observe that σ_r becomes slightly larger after relaxation, and thus the whole system slightly hotter. In their simulations of isolated models, Wu et al. (2009) considered a set of galaxy models ranging from $10^8 M_\odot$ to $10^{10} M_\odot$. During the relaxation, the models' cusp centres were found to flatten out, with the radial velocities decreasing in the core region. This is in clear contrast to the here considered Model 2, which keeps the cusp density profile, and can be traced back to a systematic error in Schwarzschild's technique (mentioned in §4.1.2) and the low resolution settings of the simulations in § 3.3.4.

The triaxial profile (Model 3) shows a result similar to Model 1. However, the anisotropic parameter $\beta(r)$ changes more significantly during the relaxation, but keeps stable afterwards. The velocity dispersion of the system becomes more isotropic and σ_r becomes smaller, implying that triaxial density profiles evolve more than axisymmetric profiles.

The profiles of the anisotropy parameter are quite different for isolated and non-isolated models: For Models 1 and 3, β is more isotropic in the centres, then the anisotropic parameter increases with radius, and stays approximately constant at $r > 1.0$ kpc. For Model 1, the anisotropy parameter reaches a maximum value of 0.5 at a radius of 3kpc, and then falls to a constant plateau around $\beta = 0.4$. For Model 3, β approaches its maximum value of 0.5 at 1kpc after which it follows a nearly flat curve. This different behaviour mainly occurs because the total mass (particle mass) is larger than in Model 1. On the other hand, the anisotropy parameter of Model 2 is almost a small constant inside 10kpc, $\beta \approx 0.2$, in accordance with the results of Wu et al. (2009). We also note that Model 2 shows a trend of becoming more radial at large radii (> 10 kpc), which is

again similar to the results presented in Wu et al. (2009).

Kinetic energy and shape

4.1.4 Kinetic energy and shape

As we have seen so far, systems embedded in external fields appear stable after their virialisation. Nevertheless, more dynamical quantities need to be investigated before we can make any safe statements about their stability, and therefore the questions remain

1. whether those galaxies continue their existence after relaxation or whether they are destroyed in the end, and
2. if these galaxies can survive, how do they evolve?

Since the inner and outermost parts of non-isolated models exhibit some evolution during the relaxation, probably causing a few particles to leave the system during this phase, we only consider the remaining (more stable) fraction of the systems' mass for further study.

As the velocities redistribute in Models 1 and 3, we note that the kinetic energy of the systems could also change by a significant amount. The left panel of Fig. 4.7 illustrates the kinetic energy tensor components K_{xx} , K_{yy} and K_{zz} which are given by

$$K_{xx} = \frac{1}{2} \frac{\sum_i m_i \cdot v_x^2}{\sum_i m_i} \quad (4.9)$$

for $r < r_{90\%}$ and analogously for the other directions, where $r_{90\%}$ denotes the radius enclosing 90% of the total mass. Since all the particles have equal mass $m_i = M/N$, Eq. 4.9 is simplified to $K_{xx} = 0.5 \langle v_x^2 \rangle$. We find that Model 2 does not exhibit any significant alterations during $60T_{simu}$. Although initially having the same density profile, the component K_{xx} of Model 1 evolves notably different from that of Model 2, being up to 10% smaller than in Model 2. Since the internal gravitational field is weakened by the external field, Model 1 cannot support a high pressure system like an isolated model. At the beginning, the kinetic energy components K_{xx} (black solid line) and K_{yy} (black dotted line) of Model 1 coincide since the ICs are axisymmetric. However, the x - z diagonal external field decreases the potential along both the x - and the z -direction, causing the components K_{xx} and K_{zz} to drop down in the now shallower potential. Note that along the z -direction, the observed evolution is not as significant as in the x -direction. At around

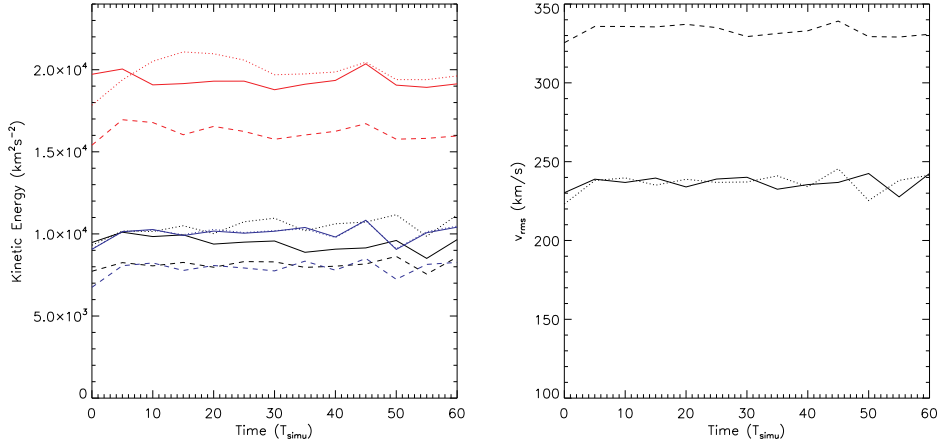


Figure 4.7: Left panel: Time evolution of the kinetic energy tensor components K_{xx} , K_{yy} and K_{zz} . The colours of black, blue and red represent Models 1, 2, and 3, respectively; the solid, dotted and dashed lines denote the different components xx , yy and zz . **Right panel:** Time evolution of the systems’ root mean square velocities. The solid, dotted and dashed correspond to the Models 1, 2 and 3, respectively.

$10T_{simu}$, K_{xx} and K_{yy} separate from each other. For the isolated Model 2 (blue lines), the components K_{xx} and K_{yy} evolve identically. Since the density profiles of Models 1 and 2 are axisymmetric, K_{zz} is always lower than the kinetic energy along the other axes.

The situation for Model 3 is more complex. At the beginning, the kinetic energies along the major axis (K_{xx}) are higher than along the intermediate one (K_{yy}). While K_{xx} initially decreases, the component K_{yy} starts to grow, and eventually becomes larger than K_{xx} after roughly $6 T_{simu}$. This exchange of kinetic energy might imply a self-rotation of the system within the $x - y$ plane, i.e. around the z -axis. Note that the tensor components of all models appear “colder” in the beginning, and the kinetic energy increases after virialisation.

The right panel of Fig. 4.7 shows the time evolution of the models’ root mean square velocities v_{rms} . For all models, v_{rms} increases about 5% after virialisation, and is stable afterwards with tiny ($\pm 2\%$) and smooth oscillations. The values of v_{rms} for the three models are roughly 235, 235 and 335 km s^{-1} , respectively. There are no obvious differences between Models 1 and 2.

The mean square lengths (MSLs) along different axes (first discussed in §3.3), I_{xx} , I_{yy} and I_{zz} , which are defined as

$$I_{xx} = \frac{1}{N_p} \sum_{i=1}^{N_p} x_i x_i, \quad (4.10)$$

and analogously for the other directions, where N_p is the number of particles inside $r_{90\%}$. Note that such a cut-off is also reasonable as the MSLs of a Hernquist profile diverge. Using the MSLs, we are able to obtain information about the shapes of the systems. From the left panel of Fig. 4.8, we notice that the MSL components in the isolated case (blue lines, Model 2) keep stable while the components of both Models 1 (black lines) and 3 (red lines) exhibit evolution during $60T_{simu}$. In Model 2, I_{xx} and I_{yy} have approximately the same value, $I_{xx} \approx I_{yy} \approx 3 \text{ kpc}^2$, and I_{zz} is about 2 kpc^2 , which implies density axis ratios of $a : b : c = 1 : 1 : 0.8$, where $a = \sqrt{I_{xx}}$, $b = \sqrt{I_{yy}}$ and $c = \sqrt{I_{zz}}$. In Model 1 (external field case), however, the components I_{xx} and I_{yy} have initially the same value of roughly 5 kpc^2 , and $I_{zz} \sim 4 \text{ kpc}^2$, implying $a : b : c = 1 : 1 : 0.9$. Induced by the external field pointing into the diagonal $x - z$ -direction, however, the components I_{xx} and I_{yy} start to separate from each other after $10T_{simu}$. And after evolving the system for 40 simulation times, the axis ratio becomes $a : b : c = 0.9 : 1 : 0.9$, with $I_{xx} \sim 4 \text{ kpc}^2$. Since the external field is oriented such that it affects components along the x - and z -axis in the same way, the evolution of I_{xx} and I_{zz} is almost identical, showing similar amplitudes of oscillation.

For Model 3 (red lines), the situation is quite similar. At the beginning, the axis ratio is about $a : b : c = 1 : 0.9 : 0.77$ which is close to the isolated case discussed in Wu et al. (2009). The initial values of I_{xx} , I_{yy} and I_{zz} are around 5, 4 and 3 kpc^2 , respectively. After 10 simulation times, however, the value of I_{xx} decreases and closely follows the component I_{yy} afterwards. The axis ratio at this point is about $a : b : c = 1.0 : 0.95 : 0.87$. At around 30 simulation times, I_{xx} again increases forming an approximately constant offset with respect to I_{yy} thereafter. Since the external field for this model points into the x -direction, i.e. perpendicular to $y - z$ plane, the curves for the components I_{yy} and I_{zz} exhibit nearly the same run. This is in agreement with our results for Model 1. Our results are consistent with the evolution of kinetic energies illustrated in Fig. 4.7, and imply that

1. the MSLs, describing the size of the galaxy, are generally larger in presence of an external field, and that

2. evolution along the external field direction can change the axis ratios, i.e. the shape of the galaxy.

As previously mentioned in §4.1.3, the presence of an external field reduces the symmetry level of the considered model, which could give rise to a self-rotation of the system. Another consequence of the external field is that - unlike the case of an isolated system - the (local) system's total angular momentum is generally no longer conserved; the external field introduces additional torque into the system. Therefore, we already expect to encounter a variation of this quantity in our simulations. To further investigate the above effects, we have calculated the angular momenta for Models 1 and 3. The results are shown in the right panel of Fig. 4.8 which illustrates the unit mass angular momentum components \mathbf{L}_x , \mathbf{L}_y and \mathbf{L}_z in the units of L_c ,

$$\mathbf{L}_x = \frac{1}{M} \sum_{i=1}^{N_p} m_i (\mathbf{L}_x)_i \quad (4.11)$$

and analogously for the other directions, where L_c is defined as the angular momentum of unit mass with circular velocity v_c at a radius $r_c = 1\text{kpc}$, $L_c = r_c v_c$. The values of L_c are listed in Table 4.3.

As we can see, individual components change by up to $0.025L_c$, and depending on the actual model their evolution can be quite different. In the case of Model 1 (black lines), for example, all angular momentum components start from values close to zero ($\lesssim 2 \times 10^{-3}L_c$), and grow in nearly the same fashion. At roughly 30 simulation times, \mathbf{L}_x begins to separate from the other components. Looking at Model 3 (red lines), we find that \mathbf{L}_x and \mathbf{L}_y are almost zero and conserved at all times. The component \mathbf{L}_z evolves in similar way as do the components of Model 1. Again, this behaviour appears related to the external field's orientation along the x -axis. Note however that the evolution of angular momentum is quite sophisticated and less intuitive as it depends on the assumed direction of the external field, the actual orbit composition and the level of numerical noise which increases with simulation time.

Finally, we point out that the observed changes of specific angular momentum components are relatively small, corresponding to a few kpc km s^{-1} . Thus our previous statements on the stability of these systems should remain valid.

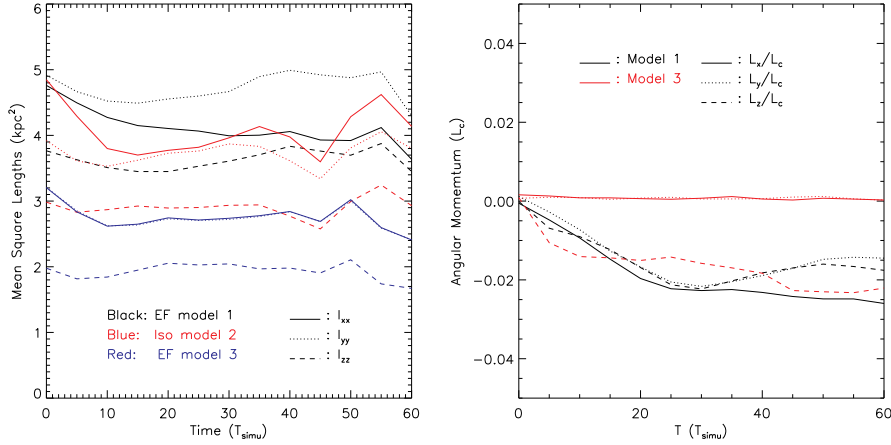


Figure 4.8: **Left panel:** Time evolution of the mean square length components I_{xx} , I_{yy} and I_{zz} . The colours black, red and blue represent the Models 1, 2, and 3, respectively; and the solid, dotted and dashed lines denote the different components xx , yy and zz . **Right panel:** Angular momenta L_x , L_y and L_z of all three models. The line types and colours are the same as those in the left panel.

Lopsidedness

In Fig. 4.1, we present the lopsidedness of the potential for both an axisymmetric and a triaxial density in the external field. The small inconsistency between the potential and density will lead to an additional relaxation of the model. Nevertheless, whether the found lopsidedness is stable, is unknown. By defining an axis ratio $r^- : r^+ = \sqrt{I_{xx}^-} : \sqrt{I_{xx}^+}$ (\pm denotes the upper/lower half space with respect to the x -axis), we can study the the shape of mass distribution at different times during evolution. In both panels of Fig. 4.9, we notice that the axis ratios of the ICs are lopsided at large radii ($r \sim r_{90\%}$, about 1.05 for Model 1 and and 1.07 for Model 3. This result means that one cannot find perfectly symmetric galaxies in the centres of clusters within in the framework of MOND. The strong external fields will distort the original symmetry when the gravitational field strength starts to become comparable to that of the internal one, which is especially true for the outer parts of a galaxy.

4.1.5 Conclusion and discussion

Using Schwarzschild's approach, we constructed (quasi-) equilibrium models for galaxies with a central cusp embedded into a uniform external field within the framework of MOND. Starting from these models, we performed stability tests by means of N -body simulations.

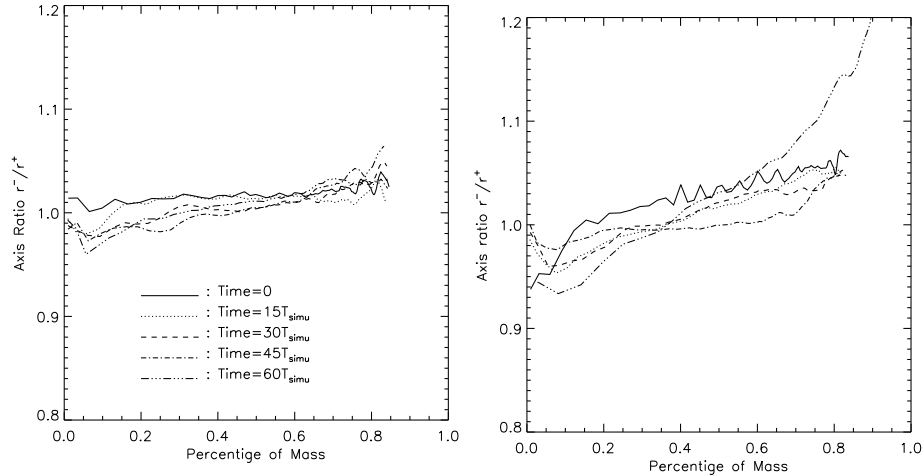


Figure 4.9: The evolution of lopsidedness $r^- : r^+$ of Models 1 and 3. Different line types refer to different evolving times. The **left panel** is for Model 1 and **right panel** for Model 3.

For the simulations, we employed a MONDian N -body code which operates on a spherical grid (Londrillo & Nipoti 2009).

When applying Schwarzschild’s method to galaxies in external fields, we observe a distortion of the systems’ internal potentials, with the NNLS method selecting more radial orbits to fit the analytic density profile by the regularization condition (Eq. 3.12). Thus the constructed ICs are not exactly self-consistent with respect to the original analytic density profile. Such a (slightly) lower level of self-consistency can lead to non-equilibrium ICs. This has been confirmed with help of N -body simulations which showed that the IC states correspond to quasi-equilibrium configurations and relax to dynamic equilibrium within a few simulation times. Note that the ICs of isolated models in Wu et al. (2009) were also found to be in quasi-equilibrium, but the major reason for this is different: While the ICs in external fields are not in equilibrium because they are generated from a not fully self-consistent Schwarzschild model, the problem in the isolated case occurred due to a lack of numerical resolution. Here resolution becomes a secondary problem for setting up ICs in external fields.

Interpreting the results of our N -body simulations, we conclude that galaxy models located within external fields are stable over at least ~ 50 dynamical timescales. Compared to the isolated case, the presence of an external field slightly enhances the size of these systems, with the effect being strongest at larger radii, i.e. the galactic outskirts. After

dynamical relaxation, the systems undergo secular evolution, and we find that a certain degree of lopsidedness arises in the galactic outskirts where internal and external fields are comparable. Our simulations further indicate that the models' central cusps remain stable at all times.

As for the models embedded into an external field, note that the systems are accelerated and moving due to the constant background field. To keep the angular resolution of the simulation at reasonable size, the galactic centre has to be placed into the grid's centre. In our simulations we transform the coordinates at every time step, moving the centre of mass (CoM) to the grid centre and changing to the frame where its velocity is zero. Note that it is not necessary that the CoM coincides with the galactic centre, i.e. the centre of the cusp. Due to the appearance of a lopsided potential, such an offset within the density distribution can develop within MOND. However, this will happen neither in Newtonian gravity nor for isolated models in MOND. For a better understanding of this effect, one could design a simple experiment: A spherically symmetric Plummer model is placed into an homogeneous external field. In the case of Newtonian gravity, the superposition principle applies, and the whole system is equally accelerated into the external field's direction. Hence the position of the CoM does not move in the internal system. For MOND, however, the internal gravity is determined by both external field and internal baryonic matter distribution. As mentioned in §4.1.1, the outer part of the galaxy's density becomes lopsided, generating an additional external field omit itself in the inner part. The additional field will cause the CoM to slightly shift away from the point where gravity equals to the external field, i.e. the point where internal gravitational field equals to zero. Since the lopsidedness appears on the system's outskirts, accounting just for a small fraction of the total mass, this is expected to be only a minor effect. More details on generic cases will be discussed in §4.2.

4.2 Cluster galaxies are non-axisymmetric in MOND

Galaxies inside clusters present us a very interesting environment where the external field has a significant influence. These galaxies experience both their self-gravity and the gravity of the other galaxies of the cluster (except for the galaxy at the center of the cluster): the latter manifests itself only as tides in standard Newtonian gravity, meaning that the systematic acceleration of the center of the mass of the galaxy has no consequence. But in the context of MOND, a consequence of the breaking of the strong equivalence principle is that the systematic acceleration changes the self-gravity of the galaxy.

In this section, we emphasize that, in MOND, the combination of the self-gravity with the external acceleration breaks the front-back symmetry of a purely self-gravitational system. As elliptical galaxies are abundant in clusters, they provide an ideal case to test this front-back asymmetry. Offsets such as those discussed in this Chapter have also been studied in the recent literature in the context of MOND N-body simulations (Knebe et al. 2009), CDM N-body simulations (Llinares et al. 2009), and lensing observations (Shan et al. 2008).

4.2.1 Lopsidedness and offset of the center of gravity

Let us look backward to the simple numerical experiment in Fig. 4.10 : we place a Plummer sphere into an homogeneous external field typical of a cluster environment, of the order of $\sim 10^{-8} \text{ cm s}^{-2}$, and we solve the modified Poisson equation of MOND, which is a non-linear elliptic partial differential equation (Bekenstein & Milgrom 1984): the boundary conditions are taken as in Wu et al. (2008), and the boundary value problem is solved by using the iterative Newton method in spherical coordinates (Ciotti et al. 2006). The isodensity and isopotential contours in the free-falling frame are then plotted on Fig. 4.10 (panel a), where the external field is applied in the negative x -direction: clearly, one sees that the isopotential contours are *flattened* and *lopsided*, in the sense that they do not exactly correspond to the same radii on the positive and negative x -axis. The explanation for this is that, in MOND, the *total* gravity (internal+external) enters the dielectric-like μ -function on the left-hand side of the modified Poisson equation (see e.g. Famaey et al. 2007a, Wu et al. 2007, 2008): because the external field has a direction, this total gravity is increased by the external field on one side of the galaxy

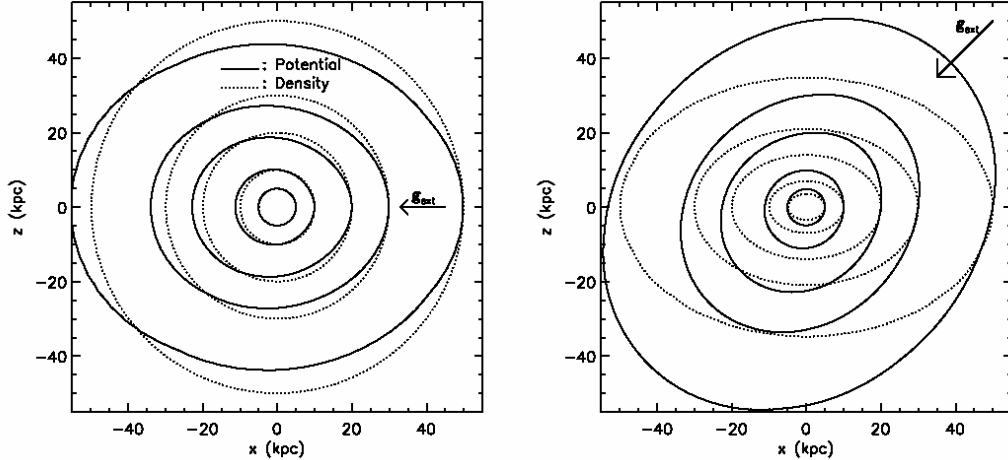


Figure 4.10: Isodensity (dotted) and MOND isopotential (solid) contours of a Plummer sphere with a $5 \times 10^{10} M_{\odot}$ mass and a Plummer scale-length of 1 kpc, embedded in an external field of $1.2 \times 10^{-8} \text{ cm s}^{-2}$ with the direction indicated by the arrow. Left panel: spherical plummer model; right panel: axisymmetric with axis ratio of 1 : 1 : 0.7 plummer model. The arrowheads show the directions of external fields.

center along the x -axis, and decreased by it on the other side. This effect is maximal when the internal and external gravities are of the same order of magnitude. Clearly, for an originally spherically symmetric distribution, the potential and its derivatives are then still axisymmetric, but the same conclusion holds when applied to an axisymmetric system, and if the direction of the external field does not coincide with the original axis of symmetry, the axial symmetry is broken. We also computed a flattened (axis ratio 0.7) Plummer model with a diagonally pointing external field. As expected, we see the twisted and offset potential contours (Fig. 4.10, panel b).

An additional interesting effect is the following: because of this lopsidedness of the potential in the outer parts, an additional “external” field is generated, which acts on the inner parts of the galaxy, akin to the effect in the inner Solar System pointed out by Milgrom (2009b). This will cause the center of the galaxy to be slightly shifted with respect to the point where the internal gravity is zero (see also Knebe et al. 2009). In the Plummer sphere model of Fig. 4.10, the internal gravity is zero at $x = 20 \text{ pc}$. Although this is small, it of course depends on the model parameters, and it means that the initial configuration can never be stable and that the photometric center of the galaxy should shift towards this new centre of gravity, thereby increasing the lopsidedness of the galaxy. We hereafter investigate whether this is the case with numerical N-body models of realistic

elliptical galaxies. Starting from initial conditions built with Schwarzschild modelling, we let the galaxy evolve towards its final state, and check whether it becomes significantly lopsided.

4.2.2 Schwarzschild and N-body models

We use the Initial Conditions (ICs) of Models 1 and 3 obtained from §4.1 via Schwarzschild method (Schwarzschild 1979, Zhao 1996, Wang et al. 2008)². Even when using 27360 orbital building blocks, we still find a significant residue of 4% between the Schwarzschild model and the input density: this means that a fully self-consistent model *cannot* be found for an axisymmetric density model embedded in a strong external field in MOND. We thus expect the system to evolve towards a non-axisymmetric equilibrium configuration.

We then turn this initial Schwarzschild model into a live N-body system by Monte Carlo sampling of the phases of the orbits. Starting with these initial conditions, we use the *N-MODY* code (Londrillo & Nipoti 2009) and let the system evolve. Fig. 4.11 and Fig. 4.12 show the evolution of projected density of the model after 0, and 90 simulation times (1 simulation time is 1 Keplerian time at the typical scale of 1 kpc, see Eq. 3.15 in §3.3.1 and Wu et al. (2009), $1T_{simu} = 4.7Myr$). One can see clearly an offset of ~ 200 pc of the central densest point from the centroids defined by the outer projected density contours. The combination of orbital anisotropy and the broken axisymmetry makes the evolution quite complex. We will report these elsewhere. By and large this live N-body simulation confirms our expectation that the axisymmetry is broken in the presence of an external field, which shows up as a twist of the isophotes and an offset of the density peaks.

The observations of 78 “nucleated” dwarf elliptical galaxies in Virgo Cluster by Binggeli et al. (2000) showed that 20% of the sample are significantly lopsided. The typical centroid offset is about 100 pc for those galaxies. The other dwarfs in this sample are also lopsided but not so significantly (Figure 4.13). We have to note that the lopsidedness is determined by the strength of the external fields. For galaxies far away the center of the clusters of galaxies, they are embedded in a weak field and thus the offsets are smaller. The

²Historically self-consistent galaxy models in Newtonian dynamics mean equilibrium models purely in the gravity of the baryons, without Dark Matter. In MOND this obviously is also the case since no dark matter is supposed to be present. However, the original density reproducing the external field here is not modeled, hence our models are not purely under self-gravity of the model galaxy.

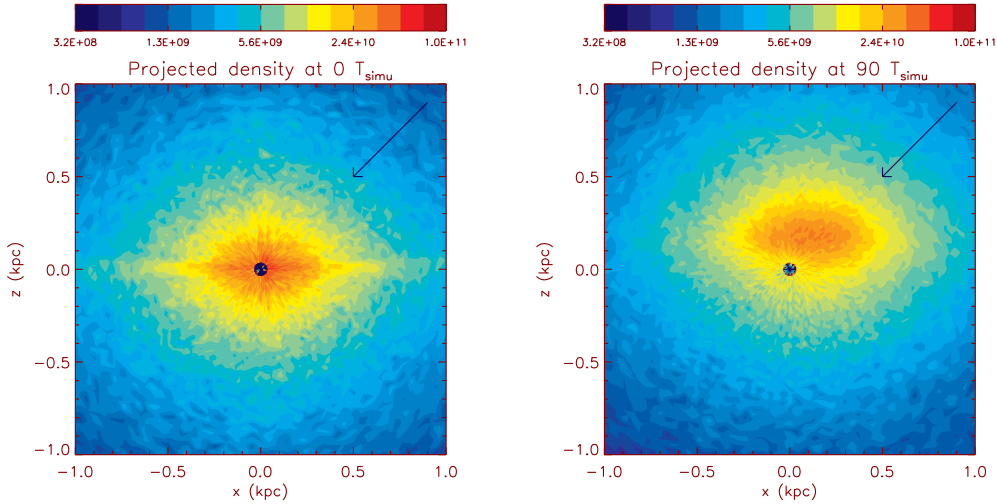


Figure 4.11: Color maps (centroid details on the scale of 1 kpc) of xz -projected density for our initial conditions (left panel) and at $t=90 T_{simu}$ later (right panel). The blue circle in the centre shows the origin point (i.e. center of mass), roughly corresponding to the centroid defined by the outer surface density contours. It is clearly offset from the central density distribution. The arrows indicate the direction of the external field.

Figure 4.13 shows the absolute offsets of the nuclei (on the left panel, in units of arcsecond, using different colours), the relative offsets $\frac{\delta_r}{r_{eff}}$ (on the right panel). The right panel shows that most dwarf galaxies are actually lopsided (the offsets are larger than 5% of their effective radii r_{eff}). Using the MOND gravity, we can easily explain this photometric result. We expect the future high resolution observations for nearby clusters will find more off-centre galaxies.

4.2.3 Conclusion

We estimate that for typical parameters of elliptical galaxies residing in large clusters, a centroid shift of a few hundreds of parsecs is expected in MOND, as compared to the centroid of the outer isodensity contours of the galaxy. While tides can also cause some lopsidedness in Newtonian and MONDian gravity, there is a major distinction with the pure MOND effect under scrutiny here. The tidal effects are small inside the tidal radius, and are traditionally neglected when dealing with dense elliptical centers. The fact that these effects can be neglected in our analysis is confirmed by the fact that the average density of our model galaxy inside the saddle point where the external field starts to dominate is larger than the cluster density. The saddle point is estimated to be 15 kpc from the Plummer sphere (total mass $10^{11} M_{\odot}$) center (Fig. 4.10 of Knebe et al. 2009). Here the

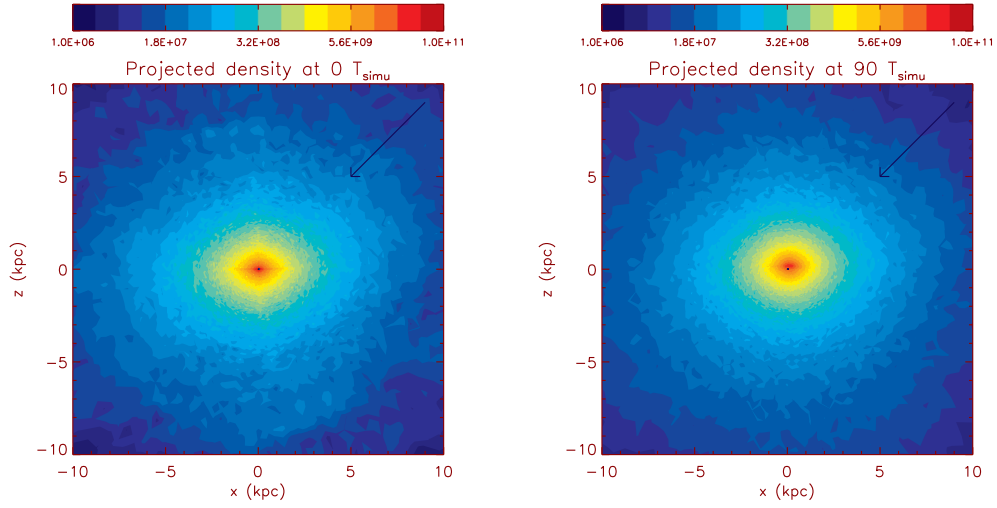


Figure 4.12: Color maps of xz -projected density on the scale of 10 kpc show the twist of isophotes between and inner and outer density distribution. The arrows indicate the direction of the external field.

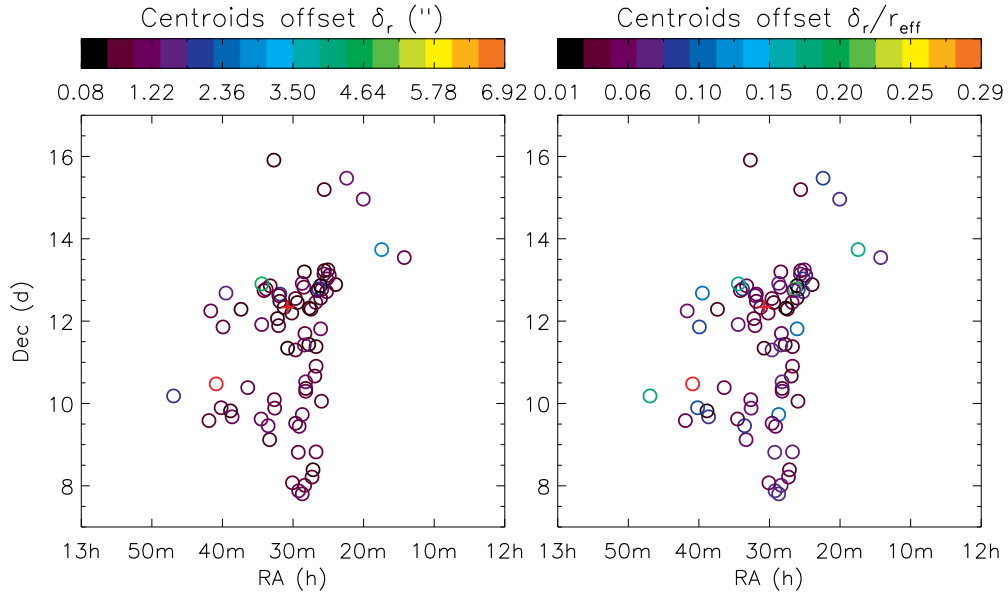


Figure 4.13: The offset of nuclei in dwarf elliptical galaxies in Virgo cluster. The coloured empty circles are the 78 dwarf ellipticals (Binggeli et al. 2000) on the sky, and the red cross in the center is the position of Virgo cluster center. The different colours on the left panel show the centroids' offsets δ_r in unit of arcsecond ($1'' \sim 100$ pc), and on the right panel the different colours show the relative offsets $\frac{\delta_r}{r_{eff}}$, where r_{eff} is the effective radii of the dwarfs.

average density enclosed is $\sim 4 \times 10^{-3} M_{\odot} \text{pc}^{-3}$, typically more than one order of magnitude larger than the typical cluster density at that same radius ($1000 \times \rho_{\text{crit}} \sim 10^{-4} M_{\odot} \text{pc}^{-3}$). Note that Zhao (1995) argues that such tidal criteria holds in MOND as well in Newton.

Thus, we conclude that if real elliptical galaxies in rich clusters show perfectly symmetric light with *no* significant offsets between the centroids of the inner and outer contours, the classical version of MOND is likely excluded. This predicted lopsidedness of galaxies inside distant rich clusters should be falsifiable with photometry *only*, using, e.g. the VLTI. To resolve a centroid offset of 200pc in an elliptical galaxy in a rich cluster of typical internal gravity $\sim 10^{-8} \text{cms}^{-2}$ at a distance of 160-210 Mpc (e.g., Abell 1983, Abell 2717, MKW9 Pointecouteau et al. 2005, Sanders 2003) would require a minimum angular resolution of 0.5 arcsec. The offsets at the centroids of galaxies are between 10 pc and 500 pc: for an elliptical in Coma (100 Mpc far away) this corresponds to 0.02 to 1 arcsec, while for an elliptical in Virgo (20 Mpc far away) it corresponds to 0.1 to 5 arcsec. In Binggeli et al. (2000) they observed such centroid offsets in a sample of dwarf ellipticals in Virgo Cluster, of which 20% are significantly lopsided, and the offsets are typically 1".

On the other hand, observing such a lopsidedness would not constitute a direct falsification of the CDM paradigm. Indeed, CDM simulations predict that isolated CDM halos are typically lopsided due to a lack of relaxation, so this should be the case inside clusters too. Macciò et al. (2007) studied the shapes of a large sample of ten thousand pure CDM halos, and found that any offset between the bary-center (CoM) and the density-center (potential minimum) is correlated with a massive satellite inside an unrelaxed halo, i.e., the offset is a measure of unrelaxedness in the CDM context. This is characterized by an offset of order of 1 or 2 percent between the central dark matter density maximum and the center of mass at the virial radius. Let us note that if this can be translated into a predicted lopsidedness for the light distribution of isolated ellipticals in CDM, this would be a clean test since MOND does not predict such an offset (except at extremely large radii) for isolated galaxies. For galaxies inside clusters, these CDM offsets would however not be expected to be aligned with the direction of the local external field pointing to the cluster center. If a statistically relevant preferred direction is found for galaxies residing in clusters, it would thus be in support of MOND, although it would not constitute a direct falsification of CDM.

A caveat is that our simulations were based on a constant external field of $\sim 10^{-8} \text{ cm s}^{-2}$. However, in reality, while galaxies are orbiting inside clusters, the external field acting on them varies with time, both in direction and amplitude. So the next step will be to make the external field vary as a function of time in our simulations, to check how this affects the predicted lopsidedness.

Finally, we also note that the flattened and lopsided potential created by the external field would also be valid in disk galaxies, although most of them are in the field or at the outskirts of galaxy clusters. Still, the flattened MOND potential would create a differential force with a component normal to the disk, hence a specific torque. This could cause differential precession of the disk angular momentum vector, and could lead to the formation of warps, even in a very low external field for isolated galaxies (e.g., Combes & Tirit 2009).

5

Conclusion

5.1 Summary

In this thesis, we investigated the dynamics of MONDian galaxies:

- We studied on the external field effect and the escape speeds for spiral galaxies in Chapter 2.1 including the Milky Way Galaxy. The external field makes the potential finite at infinity, enabling stars to escape. While MOND fits well with the rotation curve of the Milky Way, it also fits well with the escape speed (RAVE observations) at the solar neighbourhood. The rotation curves of Milky Way-like spiral galaxies are predicted to have a truncation if those galaxies are in the central regions of clusters. The High Surface Brightness (HSBs) in a strong external field will be distorted, and the Low Surface Brightness (LSBs) cannot have normal velocity dispersion like other field LSBs.

We further studied on the potentials of the Milky Way in four CDM models and compared with MOND Besançon model in §2.2, with a weak external field. We com-

pared the escape velocities as a function of position for those models. We showed that MOND predicts deeper potential than CDM, while both gravities fit well with observations and circular velocity for all radii and escape speed at the solar neighbourhood. MOND predicts a “phantom” dark matter distribution that can have negative density in places where the external field is comparable to internal fields.

- We constructed models with the Hernquist density profile for the field (§3) and clustered (§4) ellipticals. We showed that all of our models are stable during the N-body simulations. We further studied the asymmetric profiles of ellipticals embedded in an external field §2.2, there is an offset of centroids defined by the inner and outer contours.

5.2 Future work

So far, the MOND paradigm has been remarkably successful on galactic scales, for both spiral and elliptical galaxies. As an alternative to cold dark matter (CDM), this paradigm is still better suited to explain the observed conspiracy between the distribution of baryons and the gravitational field in spiral galaxies (e.g., McGaugh et al. 2007, Famaey et al. 2007b).

Although we are able to find quasi-equilibrium solutions for galaxies in idealized situations: isolated or embedded in a uniform external field, the following questions remain

- can globulars retain a nearly spherical morphology while orbiting inside the non-uniform *time-evolving external field* of the Milky Way, which changes amplitude and direction when crossing the inner disc?
- Can elliptically symmetric galaxies exist stably in non-uniform external fields inside a realistic galaxy cluster?
- Will background tides destroy these globulars and galaxies?

We plan to further study these systems (star clusters and galaxies) embedded in a time-varying external field of $\pm a_0$, to investigate a more realistic situation with tidal effects, and compare their morphology with observations: for asymmetry of the potential even in a uniform external field. We expect the system to relax to an asymmetric density

distribution too. If the systems cannot survive in a time-varying field, contrary to the observations, MOND would face a major challenge. There are several possible projects to be carried out after this thesis:

Globular clusters in the Galaxy

We plan to construct the simplest Plummer sphere in a uniform external field. The Plummer profile has a central core and a falloff of r^{-5} at large radii, and is widely used in the study of globular clusters,. In order to find out the differences with Newtonian gravity, we shall start with the simplest model, i.e. globular clusters (not galaxies) moving in the Galaxy's background fields.

At the Schwarzschild's modelling stage, we shall study the orbital structure and growth of chaos in the model, and the model self-consistency. Different strengths of external fields will be applied to build equilibrium initial conditions. We plan to construct star clusters with masses of $10^4 M_\odot$, $10^5 M_\odot$ and $10^6 M_\odot$ and different radii. The external fields applied here are the median field ($0.1a_0$) and the strong field ($1a_0$), since most of the globular clusters are bound inside 50 kpc to galactic centres, and the strength of external field ranges approximately from 0.1 to $1a_0$. The code for Schwarzschild's method is ready for a triaxial system based on a Hernquist profile (triaxial), and we shall modify the code to suit the Plummer profile. Due to the violation of symmetry by the external field, orbits starting from the phase-space region along the external field are different to orbits starting from the phase-space region against the external field. We need two sets of starting positions and velocities, along and against the external field.

Once the initial conditions are built, we will vary the strength of external fields at each point of the orbit of the globular cluster, to model the star cluster's gradual approach or recession from the galactic plane, and we will study how it expands or shrinks using N-body simulations. The stability of the models in time-varying external fields will be studied, as well as the lopsidedness of the shape. We shall use the Bologna group's **NMODY** code (Londrillo & Nipoti 2009), which can be applied immediately for a uniform external field, and we shall modify the code to simulate a time-varying external field. We shall simulate an orbit of the globular, pretending it is a test particle, in the static potential of the *Basançon Milky Way* model. We record the external field on each point. By this method we make the least modification to the code and the uniform approach on each

time step is quite reasonable, since the size of a globular cluster is several parsec to tens parsec, which is much smaller than the disc height, and the gravity of the Galactic plane doesn't change significantly on this scale.

Also we shall compare the simulation results with observations, to see if globular clusters can stably exist in MOND.

Galaxies in clusters

This is a follow-up project to §5.2 of this project plan and to Wu et al. (2009a; b). We will apply the more generic triaxial models with central cusps to the time-varying external fields. Again here we will use Dehnen's density model, and the total mass of galaxies we aim to address are : $10^9 M_\odot$, $10^{10} M_\odot$ and $10^{11} M_\odot$, respectively, from dwarf galaxies (in the deep MOND gravity) to median-sized galaxies (in the mild-MOND gravity). The strength of the external field for the initial conditions will be 0, $0.1a_0$, to $1.0a_0$, ranging from field galaxies to galaxies at the centres of rich clusters. Equilibrium models will be built via Schwarzschild's method (We already have some of the isolated models, (Wu et al. 2009) and models in strong external fields (Wu et al. 2009b, submitted)).

Once we have the model, we will let the elliptical galaxy free-fall into a non-uniform gravitational acceleration background; the way of changing the external field will be similar to the globular cluster case above. The potential of the galaxy cluster will be given by solving the MONDian Poisson equation with a King profile (an empirical density profile describes the baryonic distribution in a cluster). The related physical process is elliptical galaxies moving in the centres of rich clusters, and we plan to study whether the cusp centres can stably exist and the evolution of the ellipticals. Also we plan to study the rate of mass loss of the galaxies during their motion in the non-uniform external field.

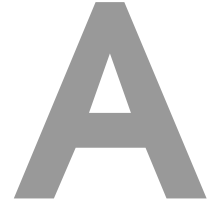
5.2.1 Galaxy mergers and elliptical galaxies

Besides Schwarzschild's method, another popular way to generate elliptical galaxies is by galaxy merging. We will run N-body merger simulations in MOND to merge galaxies (major merger) built in §5.2 and will analyze the end-product to compare with the CDM framework.

We expect that the merging end-products are different from those found in CDM, since

the MOND effect is weakened when the two galaxies are colliding, and becomes important again when they separate far away. One of the interesting physics issues we would like to study is the mass loss of the merger, i.e. how much mass remains in the end-product? We are also interested in the limits of flattening of elliptical galaxies in MOND, i.e. can MOND generate more elongated stable galaxies conflicting with observations?

We shall run simulations in both CDM and MOND frameworks, to compare the results. For MOND simulations.



Phantom Dark Matter in External Fields

The phantom dark matter (see §2.2.2) is the effective dark matter in MOND: first place the phantom dark matter in a certain way, along with the observed baryonic density distribution, and then solve the linear Poisson equation to reproduce the MONDian potential.

The MONDian Poisson's equation embedded in an external field is (i.e., Eq.1.17)

$$-\nabla \cdot \left[\mu \left(\frac{|\mathbf{g}|}{a_0} \right) \mathbf{g} \right] = 4\pi G\rho, \quad \mathbf{g} = \mathbf{g}_{\text{ext}} - \nabla\Phi_{\text{int}}, \quad (\text{A.1})$$

where ρ is the baryonic matter, \mathbf{g}_{ext} an external field, and Φ_{int} the (internal) potential of the system.

Eq. 2.15 in §2.2.2 shows how to derive the density of phantom dark matter ρ_{PDM} in the MOND context. But, as opposed to the dark matter theory, MOND immediately predicts the distribution of the dynamical mass once the baryons ρ and the gravity of the environment \mathbf{g}_{ext} are specified. However, due to the external field \mathbf{g}_{ext} the boundary condition of the (internal) system changes, not necessarily preserving spherical symmetry:

the distribution of the dynamical mass is somewhat different from that of CDM halos (see Wu et al. 2007, 2008). Further, there exist negative solutions of the PDM, and the peaks of dynamical mass can in fact be offset from the baryonic peaks! These effects are most significant at places where the external and internal fields are comparable and should be quantified more carefully in the following subsections (from the sections which I contributed to Bienaymé et al. 2009, Knebe et al. 2009, and Zhao et al. 2010, in preparation).

A.1 Vertical kinematics of the Galaxy

The panels a and c of Fig. 2.5 in §2.2.2 are the density of PDM ρ_{PDM} on the disc scale. We find that inside 20 kpc on the x -axis, there are disc-like distributions of ρ_{PDM} . Inside the Galactic 20 kpc, the gravity acceleration is strong, in the order of magnitude of a_0 . The prediction of effective dark matter disc in the brightest baryonic disc region is interesting. In these regions the MOND effect is mild. By numerically solving the Eq.2.15 with the MOND gravitational potential §2.2.2, we obtain the dynamical density ρ_{dyn} (i.e., baryonic matter density ρ_b plus PDM density ρ_{PDM}) for the Besançon Milky Way model. In Fig. A.1, the dashed line is the radial density distribution of the baryons in the Galactic plane, while the solid line is the total dynamical density. The radial scale length of the thin disc is 2.5 kpc in Besançon model, and the dynamical disc scale length is 3.1 kpc in MOND.

By integrating the volume density along the vertical direction of the Milky Way on the Galactic plane, one can obtain the surface density of the Galactic disc $\Sigma(R, z)$, which is

$$\Sigma(R, z) = \int_{-z_0}^{+z_0} \rho(r, z) dz, \quad (\text{A.2})$$

where R is the projected radius on the Galactic plane. We get the surface density at the solar neighbourhood $\Sigma(R_\odot)$ by integrating the above equation inside the cylinder with disc height $z_0 = 1.1$ kpc. We find that the dynamical surface density $\Sigma_z = \Sigma_{baryons} + \Sigma_{PDM}$ at the solar neighbourhood increases of 57%, 62% and 66% with the solar neighbourhood $R_\odot = 7.5, 8, 8.5$ kpc, where $\Sigma_{baryons}$ and Σ_{PDM} are the surface densities of baryons and phantom dark matter. The dynamical surface density obtained in the Besançon model is about $78 M_\odot/\text{pc}^2$ at $R_\odot = 8.5$ kpc, while the observations by Holmberg & Flynn

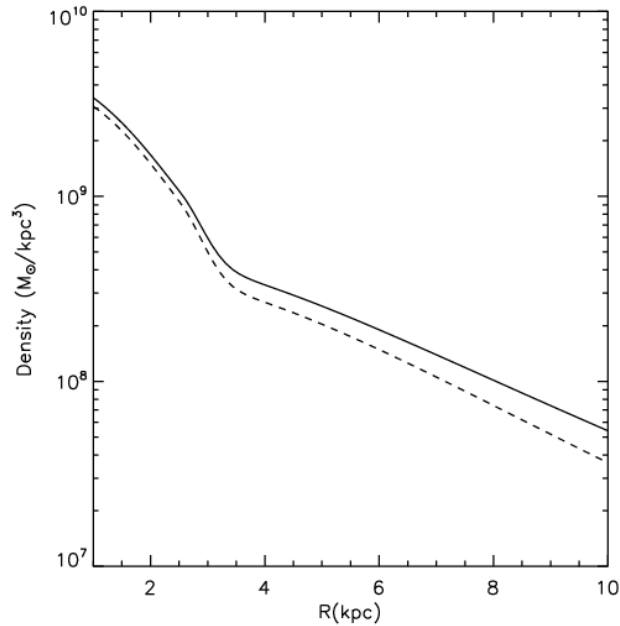


Figure A.1: **Dashed line:** The radial density distribution $\rho(R, z = 0)$ of the baryonic matter within the Besançon model. **Solid line:** The baryonic+phantom density in the Galactic plane from the Besançon MOND model.

(2004) showed that the local dynamical surface density is $74 \pm 6 M_{\odot}/\text{pc}^2$. The dynamical surface density determined by local vertical force, K_z , should be compared as well, where $|z| \leq 1.1$ kpc.

In CDM models, the thin disc dominates the disc mass distribution, implying that the dark matter halo does not make significant contributions to the Galactic disc. Therefore, we would expect that the measurements of dynamical disc from GAIA or JASMINE may be able to test the dynamics of Newton or MOND.

A.2 Offsets of density peaks for PDM

The PDM gives rise to different effects compared with the ordinary cold dark matter, one of which is the above mentioned negative density. Here we shall introduce another effect: the offsets of density peaks for the PDM. The non-cosmological and cosmological environments have been discussed in Knebe et al. (2009), however, we shall only discuss the non-cosmological effect here.

Table A.1: Models and Parameters, mass is in unit of ($10^{10}M_{\odot}$), positions and r_0 are in unit of kpc , external gravity accelerations are in unit of a_0 .

Model	Mass 1	Mass 2	Centre 1	Centre 2	g_{ext}	r_0
G+EF	10.0	-	(0,0,0)	-	1.0	2.0
GG	10.0	10.0	(-5.0,0,0)	(5.0,0,0)	0.0	6.0
GS	10.0	1.0	(-5.0,0,0)	(5.0,0,0)	0.0	6.0
GG+EF	1.0	1.0	(-3.0,0,0)	(3.0,0,0)	1.0	4.0

A.2.1 The Simulations

For the non-cosmological settings studied in this Section we use the MONDian Poisson solver developed by the Bologna group (Ciotti et al. 2006, Nipoti et al. 2007a) to solve Eq. A.1 and hence derive the internal potential Φ_{int} of the systems under investigation. The Poisson solver is a spherical grid code, and our choice for the grid parameters is $n_r \times n_{\theta} \times n_{\phi} = 256 \times 64 \times 128$ with a radial grid spacing given by $r_i = r_0 \tan [(i + 0.5)0.5\pi/(n_r + 1)]$ kpc. We further utilize Eq. 2.15 to derive the dynamical mass and the phantom matter, respectively.

All our (baryonic) galaxies have a Plummer density profile

$$\rho(r) = \left(\frac{3M}{4\pi b^3} \right) \left(1 + \frac{r^2}{b^2} \right)^{-5/2}, \quad (\text{A.3})$$

with a core radius b of 1.0 kpc.

We investigated four scenarios characterized as follows:

- G+EF: a galaxy embedded in strong constant external field,
- GG: a binary galaxy system with equal masses for the two component and no additional external field,
- GS: a binary galaxy system consisting of a host galaxy with a total mass 10 times that of a satellite galaxy; the external field seen by the satellite is that of the host,
- GG+EF: system GG embedded in a strong constant external field.

A summary of the actual parameters can be found in Table A.1.

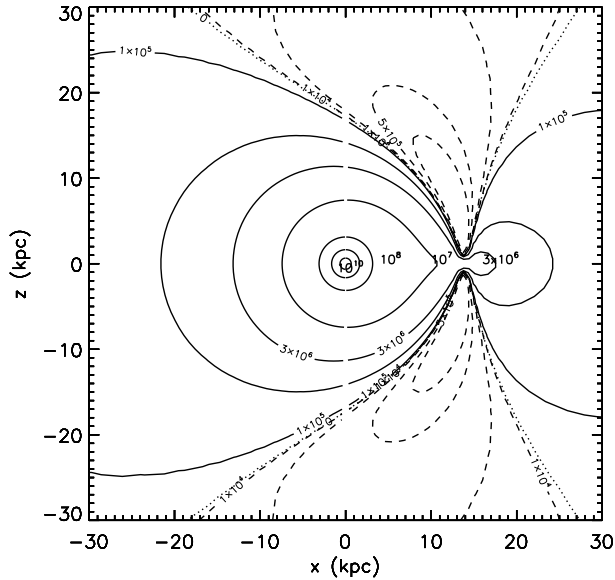


Figure A.2: Isodensity countours of the dynamical mass, i.e. baryons + PDM density, on the $x - z$ plane for a galaxy embedded within an external field along the x -axis.

A.2.2 Density Peak Offsets

Fig. A.2 shows the distribution of the dynamical mass for the model G+EF, i.e. a single galaxy embedded in an external field of strength $g_{\text{ext}} = a_0$ along the x -axis. We notice that when the internal and external field are of the same order of magnitude, i.e. at $x \approx 15$ kpc, there are several noticeable effects: first, a negative dynamical mass is obtained on the fat discs perpendicular to the direction of external field, as mentioned by Milgrom (1986) and Wu et al. (2008); second, there is an additional peak on the x -axis, where the external and internal fields cancel each other! However, this additional peak is four orders of magnitudes smaller than the baryonic peak.

While we also recovered negative dynamical densities for the binary system consisting of two equal mass galaxies (i.e. model GG), there are no additional peaks. This can be seen in Fig. A.3 and in particular the zoom onto the central region between the galaxies in the right panel. However, as soon as the two systems have different masses, we found again an additional peak in the dynamical mass distribution between the two systems where the gravity cancels. This can be viewed in Fig. A.4 where we found the strength of the phantom peak to be 1% of the baryonic peak of the satellite! A similar situation appears when we embed the model GG into an external field: Fig. A.5 clearly shows both the negative dynamical mass densities as well as a (strong) additional peak between the

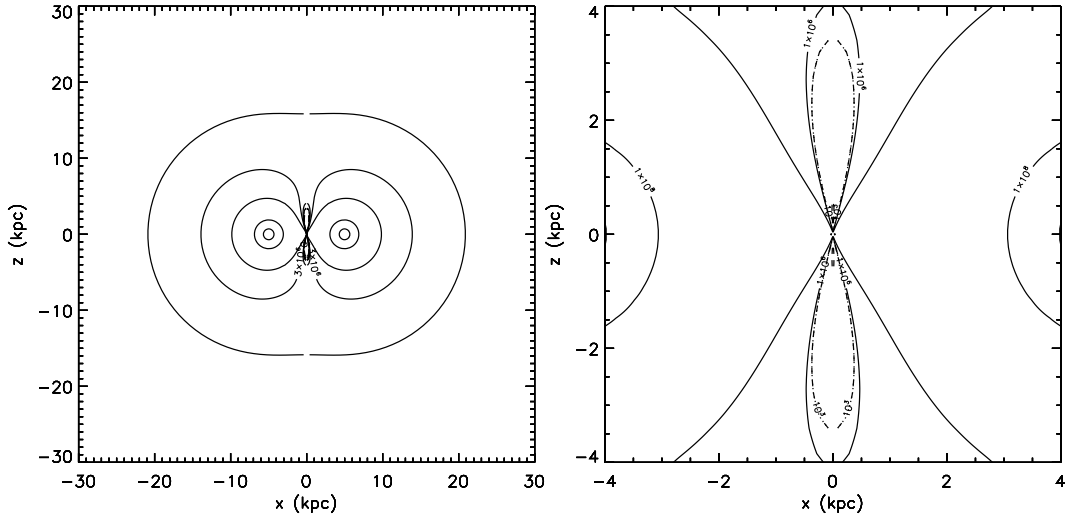


Figure A.3: The same as Fig. A.2 for the binary system consisting of two equal mass galaxies, i.e. model GG. The right panel is a zoom into the central region between the two galaxies.

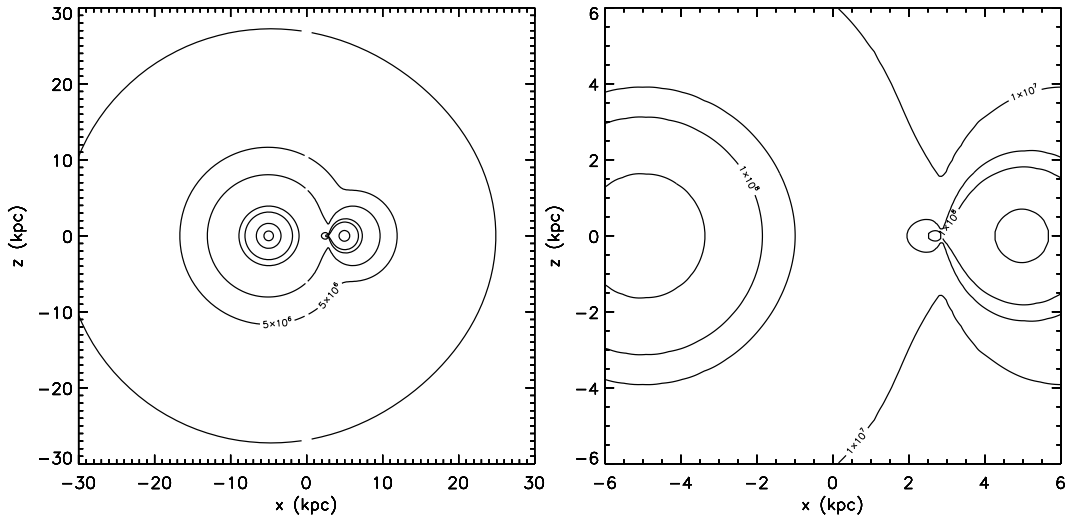


Figure A.4: The same as Fig. A.2 for the binary system consisting of a host and a satellite galaxy with 1/10th of the host's mass, i.e. model GS. The right panel is again a zoom into the central region between the two galaxies.

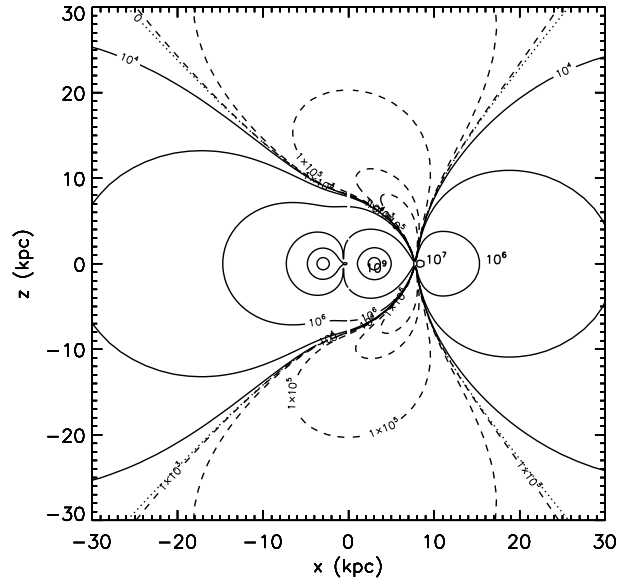


Figure A.5: The same as Fig. A.2 with the system GG now being embedded within an external field along the x -axis, i.e. model GG+EF.

galaxies. This time the strength of such extra peak is 0.1% of the baryonic matter peaks of each individual galaxy.

In summary, we have seen that in most of the situations the interpretation of the MONDian potential in a Newtonian sense leads to the prediction of additional peaks in the distribution of the dynamical mass when compared to the actual (underlying) baryonic matter distribution. However, the strength of these extra peaks varies and depends on the actual setup of the system ranging from as low as four orders of magnitude smaller to as large as 1% for the cases considered here. We therefore may rightfully ask the question whether a self-consistent cosmological simulation can provide a suitable variety of configurations so that we may in fact observe (and quantify) the offset between the baryonic and phantom matter peaks. In Knebe et al. (2009) they further showed that actually the cosmological effect is too weak to be observed, which implies that the offsets of baryons and dark matter in clusters like "Bullet cluster" should require additional dark matter like neutrinos even in MOND.

B

Comparison with another MOND solver

As just highlighted in Section 3, there are numerical challenges to evolving our systems under MONDian gravity using the N-body code NMODY. In order to confirm that the results are not unique to this one code we therefore decided to also use another novel solver for the MONDian analog to Poisson's equation, namely the AMIGA code (Llinares, Knebe & Zhao 2008). AMIGA is the successor to MLAPM (Knebe et al. 2001) that has recently been adapted to also solve Eq. 3.2.¹ The code utilizes adaptive meshes in Cartesian coordinates in a cubical volume as opposed to the spherical grid of NMODY. The solution is obtained via multi-grid relaxation and we refer the interested reader to Llinares et al. (2008) for more details.

However, here we need to elaborate upon the boundary constraints as we cannot assume that the potential on the boundary will be a constant: the box is a cube and not a sphere. We decided to use the solution for a point mass in the center of the box

¹We like to note in passing that MLAPM has already been successfully applied to study cosmological structure formation under MOND (Knebe & Gibson 2004) under certain assumptions.

$$\Phi(r) = -\frac{GM}{2} \left(\frac{1}{r} - \frac{1}{r_0} \right) + (f(r) - f(r_0)), \quad (\text{B.1})$$

with

$$f(r) = -\sqrt{GMa_0} \left[\frac{-1}{2r} \sqrt{q^2 + 4r^2} + \ln \left(2r + \sqrt{q^2 + 4r^2} \right) \right] \quad (\text{B.2})$$

$$q^2 = \frac{GM}{a_0},$$

where, M is the total mass in the box and r_0 is a length scale (a constant of integration). Note that Eq. 16 and Eq. 17 are the initial guess of the potential, for solving the modified Poisson. For $a_0 \rightarrow 0$ we recover the Newtonian solution and for a_0 finite and $r \rightarrow \infty$ we have $\ln(r)$, which is the typical behaviour for any MONDian solution. In the case that we use $r_0 = B$, with B being the size of the cubical box, we end up with $\Phi = 0$ in a sphere of radius B , that is equivalent to the conditions used in NMODY.

We now run simulations with the same Initial Conditions for N-body as used with NMODY utilizing a domain grid with 128^3 cells. Each of these domain grid cells is refined and split into eight sub-cells once the number of particles inside that cell is in excess of 6. The box size is $B = 165.5152\text{kpc}$ and the scale for the boundary conditions is $r_0 = 82.7576\text{Kpc}$ (half of the box).

The results obtained are similar to the NMODY simulations. The system is stable with a normal secular evolution. We observe the same kind of evolution. We confirm that all other quantities behave in a similar manner too, and hence are confident that the results presented in the previous section 3.3 are not dominated and/or contaminated by numerical artifacts.

Bibliography

- Allgood, B., Flores, R. A., Primack, J. R., Kravtsov, A. V., Wechsler, R. H., Faltenbacher, A., & Bullock, J. S. 2006, *MNRAS*, 367, 1781, arXiv:astro-ph/0508497
- Angus, G. W. 2008, *MNRAS*, 387, 1481, 0804.3812
- Angus, G. W., Famaey, B., & Zhao, H. S. 2006, *MNRAS*, 371, 138, astro-ph/0606216
- Angus, G. W., & McGaugh, S. S. 2008, *MNRAS*, 383, 417, 0704.0381
- Angus, G. W., Shan, H. Y., Zhao, H. S., & Famaey, B. 2007a, *ApJ*, 654, L13, astro-ph/0609125
- . 2007b, *ApJ*, 654, L13, arXiv:astro-ph/0609125
- Baes, M., & Dejonghe, H. 2002, *A&A*, 393, 485, arXiv:astro-ph/0207233
- Bailin, J., & Steinmetz, M. 2005, *ApJ*, 627, 647, arXiv:astro-ph/0408163
- Begeman, K. G. 1989, *A&A*, 223, 47
- Begeman, K. G., Broeils, A. H., & Sanders, R. H. 1991, *MNRAS*, 249, 523
- Bekenstein, J. 2006, *Contemporary Physics*, 47, 387, arXiv:astro-ph/0701848
- Bekenstein, J., & Milgrom, M. 1984, *ApJ*, 286, 7
- Bekenstein, J. D. 2004a, *Phys. Rev. D*, 70, 083509, astro-ph/0403694
- . 2004b, *Phys. Rev. D*, 70, 083509, arXiv:astro-ph/0403694
- . 2009, *Nuclear Physics A*, 827, 555, 0901.1524
- Bekenstein, J. D., & Sanders, R. H. 1994, *ApJ*, 429, 480, arXiv:astro-ph/9311062
- Besla, G., Kallivayalil, N., Hernquist, L., Robertson, B., Cox, T. J., van der Marel, R. P., & Alcock, C. 2007, *ApJ*, 668, 949, arXiv:astro-ph/0703196
- Bienaymé, O., Famaey, B., Wu, X., Zhao, H. S., & Aubert, D. 2009, *A&A*, 500, 801, 0904.3893
- Binggeli, B., Barazza, F., & Jerjen, H. 2000, *A&A*, 359, 447
- Binney, J. 2005, *MNRAS*, 363, 937, arXiv:astro-ph/0504387

- Binney, J., & Dehnen, W. 1997, MNRAS, 287, L5, arXiv:astro-ph/9612060
- Binney, J., & Tremaine, S. 1987, Galactic dynamics, ed. S. Binney, J. & Tremaine
- Bissantz, N., Englmaier, P., & Gerhard, O. 2003, MNRAS, 340, 949, arXiv:astro-ph/0212516
- Bosma, A. 1981a, AJ, 86, 1791
- . 1981b, AJ, 86, 1825
- Brada, R., & Milgrom, M. 1995, MNRAS, 276, 453
- . 2000, ApJ, 541, 556, arXiv:astro-ph/0005194
- Broeils, A. H. 1992, A&A, 256, 19
- Bromley, B. C., Kenyon, S. J., Brown, W. R., & Geller, M. J. 2009, ApJ, 706, 925, 0907.5567
- Brown, W. R., Geller, M. J., Kenyon, S. J., Kurtz, M. J., & Bromley, B. C. 2007a, ApJ, 660, 311, arXiv:astro-ph/0701600
- . 2007b, ApJ, 671, 1708, 0709.1471
- Bruneton, J.-P., & Esposito-Farèse, G. 2007a, Phys. Rev. D, 76, 124012, 0705.4043
- . 2007b, Phys. Rev. D, 76, 124012, 0705.4043
- Caldwell, J. A. R., & Ostriker, J. P. 1981, ApJ, 251, 61
- Capuzzo-Dolcetta, R., Leccese, L., Merritt, D., & Vicari, A. 2007, ApJ, 666, 165, arXiv:astro-ph/0611205
- Carignan, C., Chemin, L., Huchtmeier, W. K., & Lockman, F. J. 2006, ApJ, 641, L109, arXiv:astro-ph/0603143
- Chen, D.-M., & Zhao, H. 2006, ApJ, 650, L9, arXiv:astro-ph/0606506
- Chiu, M.-C., Ko, C.-M., & Tian, Y. 2006, ApJ, 636, 565, arXiv:astro-ph/0507332
- Chung, A., van Gorkom, J. H., Kenney, J. D. P., & Vollmer, B. 2007, ApJ, 659, L115, arXiv:astro-ph/0703338
- Ciotti, L., & Binney, J. 2004, MNRAS, 351, 285, arXiv:astro-ph/0403020
- Ciotti, L., Londrillo, P., & Nipoti, C. 2006, ApJ, 640, 741, arXiv:astro-ph/0512056
- Clemens, D. P. 1985, ApJ, 295, 422
- Combes, F., & Tiret, O. 2009, ArXiv e-prints, 0908.3289
- Cortese, L. et al. 2007, MNRAS, 376, 157, arXiv:astro-ph/0703012

- Crane, P. et al. 1993, *AJ*, 106, 1371
- de Vaucouleurs, G. 1948, *Annales d'Astrophysique*, 11, 247
- de Zeeuw, P. T., & Lynden-Bell, D. 1985, *MNRAS*, 215, 713
- Dehnen, W. 1993, *MNRAS*, 265, 250
- Diaz-Rivera, L. M., Samushia, L., & Ratra, B. 2006, *Phys. Rev. D*, 73, 083503, arXiv:astro-ph/0601153
- Dodson, S., & Liguori, M. 2006a, *Physical Review Letters*, 97, 231301, arXiv:astro-ph/0608602
- . 2006b, *Physical Review Letters*, 97, 231301, arXiv:astro-ph/0608602
- Evstigneeva, E. A., Gregg, M. D., Drinkwater, M. J., & Hilker, M. 2007, *AJ*, 133, 1722, arXiv:astro-ph/0612483
- Famaey, B., Angus, G. W., Gentile, G., Shan, H. Y., & Zhao, H. S. 2008, in *Proceed. of the Sixth International Heidelberg Conference on Dark Matter in Astro- and Particle Physics (DARK 2007)*, held at the University of Sydney, Australia, 23-28 September 2007, Eds. H. V. Klapdor-Kleingrothaus, G. Lewis, World Scientific, Singapore, ISBN-13 978-981-281-434-0, ISBN-10 981-281-434-5, pp. 393-401, 393-401
- Famaey, B., & Binney, J. 2005, *MNRAS*, 363, 603, arXiv:astro-ph/0506723
- Famaey, B., Bruneton, J.-P., & Zhao, H. 2007a, *MNRAS*, 377, L79, arXiv:astro-ph/0702275
- Famaey, B., Gentile, G., Bruneton, J.-P., & Zhao, H. 2007b, *Phys. Rev. D*, 75, 063002, arXiv:astro-ph/0611132
- Fehlberg, E. 1968, *Classical Fifth-, Sixth-, Seventh- and Eighth-Order Rung-Kutta Formulas with Stepsize control* (NASA, Washington: NASA Tech. Rep. R-287c.)
- Feix, M., Fedeli, C., & Bartelmann, M. 2008a, *A&A*, 480, 313, arXiv:0707.0790
- Feix, M., Xu, D., Shan, H., Famaey, B., Limousin, M., Zhao, H., & Taylor, A. 2008b, *ApJ*, 682, 711, 0710.4935
- Ferrarese, L., van den Bosch, F. C., Ford, H. C., Jaffe, W., & O'Connell, R. W. 1994, *AJ*, 108, 1598
- Ferreira, P. G., & Starkman, G. D. 2009, *Science*, 326, 812, 0911.1212
- Gadotti, D. A. 2009, *MNRAS*, 393, 1531, 0810.1953
- Gardiner, L. T., Sawa, T., & Fujimoto, M. 1994, *MNRAS*, 266, 567
- Gebhardt, K. et al. 2003, *ApJ*, 583, 92, arXiv:astro-ph/0209483

- Geehan, J. J., Fardal, M. A., Babul, A., & Guhathakurta, P. 2006, MNRAS, 366, 996, arXiv:astro-ph/0501240
- Gentile, G., Famaey, B., Combes, F., Kroupa, P., Zhao, H. S., & Tiret, O. 2007a, A&A, 472, L25, arXiv:0706.1976
- Gentile, G., Famaey, B., Zhao, H., & Salucci, P. 2009, Nature, 461, 627, 0909.5203
- Gentile, G., Salucci, P., Klein, U., & Granato, G. L. 2007b, MNRAS, 375, 199, arXiv:astro-ph/0611355
- Gnedin, O. Y., Gould, A., Miralda-Escudé, J., & Zentner, A. R. 2005, ApJ, 634, 344, arXiv:astro-ph/0506739
- Guhathakurta, P., van Gorkom, J. H., Kotanyi, C. G., & Balkowski, C. 1988, AJ, 96, 851
- Haghi, H., Baumgardt, H., Kroupa, P., Grebel, E. K., Hilker, M., & Jordi, K. 2009, MNRAS, 395, 1549, 0902.1846
- Halle, A., Zhao, H., & Li, B. 2008, ApJS, 177, 1
- Hao, J. G., & Akhoury, R. 2005, ArXiv Astrophysics e-prints, arXiv:astro-ph/0504130
- Heller, P., & Rohlfs, K. 1994, A&A, 291, 743
- Hernández, X., Avila-Reese, V., & Firmani, C. 2001, MNRAS, 327, 329, arXiv:astro-ph/0105092
- Hernquist, L. 1990a, ApJ, 356, 359
- . 1990b, ApJ, 356, 359
- Hernquist, L., & Ostriker, J. P. 1992, ApJ, 386, 375
- Hills, J. G. 1988, Nature, 331, 687
- Holmberg, J., & Flynn, C. 2004, MNRAS, 352, 440, arXiv:astro-ph/0405155
- Jaffe, W. 1983, MNRAS, 202, 995
- Jee, M. J. et al. 2007, ApJ, 661, 728, arXiv:0705.2171
- Jing, Y. P., & Suto, Y. 2002, ApJ, 574, 538, arXiv:astro-ph/0202064
- Kallivayalil, N., van der Marel, R. P., & Alcock, C. 2006a, ApJ, 652, 1213, arXiv:astro-ph/0606240
- Kallivayalil, N., van der Marel, R. P., Alcock, C., Axelrod, T., Cook, K. H., Drake, A. J., & Geha, M. 2006b, ApJ, 638, 772, arXiv:astro-ph/0508457
- Kent, S. M., Dame, T. M., & Fazio, G. 1991, ApJ, 378, 131
- Klypin, A., Zhao, H., & Somerville, R. S. 2002, ApJ, 573, 597, arXiv:astro-ph/0110390

- Knebe, A., & Gibson, B. K. 2004, MNRAS, 347, 1055, arXiv:astro-ph/0303222
- Knebe, A., Green, A., & Binney, J. 2001, MNRAS, 325, 845, arXiv:astro-ph/0103503
- Knebe, A., Llinares, C., Wu, X., & Zhao, H. S. 2009, ApJ, 703, 2285, 0908.3480
- Kroupa, P. 2001, MNRAS, 322, 231, arXiv:astro-ph/0009005
- Kuzmin, G. G. 1973, in Dynamics of Galaxies and Star Clusters, 71–75
- Larson, R. B., & Tinsley, B. M. 1978, ApJ, 219, 46
- Lauer, T. R. et al. 1995, AJ, 110, 2622
- Lawson, C. L., & Hanson, R. J. 1974, Solving least squares problems, ed. R. J. Lawson, C. L. & Hanson
- Li, B., & Zhao, H. 2009, ArXiv e-prints, 0906.3880
- Llinares, C., Knebe, A., & Zhao, H. 2008, MNRAS, 391, 1778, 0809.2899
- Llinares, C., Zhao, H. S., & Knebe, A. 2009, ApJ, 695, L145, 0902.3010
- Londrillo, P., & Nipoti, C. 2009, Memorie della Societa Astronomica Italiana Supplement, 13, 89, 0803.4456
- Lu, Y., Zhang, F., & Yu, Q. 2010, ApJ, 709, 1356, 0910.3260
- Lucy, L. B. 1974, AJ, 79, 745
- Macciò, A. V., Dutton, A. A., van den Bosch, F. C., Moore, B., Potter, D., & Stadel, J. 2007, MNRAS, 378, 55, arXiv:astro-ph/0608157
- Mastropietro, C., Moore, B., Mayer, L., Wadsley, J., & Stadel, J. 2005, MNRAS, 363, 509, arXiv:astro-ph/0412312
- McGaugh, S. S. 2005, Physical Review Letters, 95, 171302, arXiv:astro-ph/0509305
- McGaugh, S. S., de Blok, W. J. G., Schombert, J. M., Kuzio de Naray, R., & Kim, J. H. 2007, ApJ, 659, 149, arXiv:astro-ph/0612410
- McGaugh, S. S., Schombert, J. M., Bothun, G. D., & de Blok, W. J. G. 2000, ApJ, 533, L99, arXiv:astro-ph/0003001
- Merritt, D. 1980, ApJS, 43, 435
- Merritt, D., & Fridman, T. 1996, ApJ, 460, 136, arXiv:astro-ph/9511021
- Merritt, D., & Quinlan, G. D. 1998, ApJ, 498, 625, arXiv:astro-ph/9709106
- Mihos, J. C., McGaugh, S. S., & de Blok, W. J. G. 1997, ApJ, 477, L79+
- Milgrom, M. 1983a, ApJ, 270, 371

- . 1983b, *ApJ*, 270, 384
- . 1983c, *ApJ*, 270, 365
- . 1984, *ApJ*, 287, 571
- . 1986, *ApJ*, 306, 9
- . 1994a, *Annals of Physics*, 229, 384, arXiv:astro-ph/9303012
- . 1994b, *ApJ*, 429, 540, arXiv:astro-ph/9311031
- . 1999, *Physics Letters A*, 253, 273, arXiv:astro-ph/9805346
- . 2002, *ApJ*, 577, L75
- . 2007, *ApJ*, 667, L45, 0706.0875
- . 2008a, *New Astronomy Review*, 51, 906, 0712.4203
- . 2008b, *ArXiv e-prints*, 0801.3133
- . 2009a, *Phys. Rev. D*, 80, 123536, 0912.0790
- . 2009b, *MNRAS*, 1143, 0906.4817
- . 2009c, *MNRAS*, 398, 1023, 0909.5184
- Milgrom, M., & Sanders, R. H. 2007, *ApJ*, 658, L17, arXiv:astro-ph/0611494
- . 2008, *ApJ*, 678, 131, 0709.2561
- Moller, P., Stiavelli, M., & Zeilinger, W. W. 1995, *MNRAS*, 276, 979
- Moore, B. 1999, *Royal Society of London Philosophical Transactions Series A*, 357, 3259
- Murai, T., & Fujimoto, M. 1980, *PASJ*, 32, 581
- Navarro, J. F., Frenk, C. S., & White, S. D. M. 1997, *ApJ*, 490, 493, arXiv:astro-ph/9611107
- Nipoti, C., Ciotti, L., Binney, J., & Londrillo, P. 2008, *MNRAS*, 386, 2194, 0802.1122
- Nipoti, C., Londrillo, P., & Ciotti, L. 2006, *MNRAS*, 370, 681, arXiv:astro-ph/0605260
- . 2007a, *ApJ*, 660, 256, arXiv:astro-ph/0701418
- . 2007b, *MNRAS*, 381, L104, 0705.4633
- Nipoti, C., Londrillo, P., Zhao, H. S., & Ciotti, L. 2007c, *MNRAS*, 379, 597
- Olling, R. P., & Merrifield, M. R. 2001, *MNRAS*, 326, 164, arXiv:astro-ph/0104465
- Perets, H. B. 2009, *ApJ*, 690, 795, 0712.1888

- Perets, H. B., Hopman, C., & Alexander, T. 2007, *ApJ*, 656, 709, arXiv:astro-ph/0606443
- Perets, H. B., Wu, X., Zhao, H. S., Famaey, B., Gentile, G., & Alexander, T. 2009, *ApJ*, 697, 2096, 0809.2087
- Pfenniger, D. 1984, *A&A*, 134, 373
- Piatek, S., Pryor, C., & Olszewski, E. W. 2007, ArXiv e-prints, 0712.1764
- Pointecouteau, E., Arnaud, M., & Pratt, G. W. 2005, *A&A*, 435, 1, arXiv:astro-ph/0501635
- Poon, M. Y., & Merritt, D. 2004, *ApJ*, 606, 774, arXiv:astro-ph/0212581
- Qin, B., Wu, X. P., & Zou, Z. L. 1995, *A&A*, 296, 264
- Radburn-Smith, D. J., Lucey, J. R., Woudt, P. A., Kraan-Korteweg, R. C., & Watson, F. G. 2006, *MNRAS*, 369, 1131, arXiv:astro-ph/0603692
- Richstone, D. O. 1980, *ApJ*, 238, 103
- . 1984, *ApJ*, 281, 100
- Richstone, D. O., & Tremaine, S. 1984, *ApJ*, 286, 27
- . 1988, *ApJ*, 327, 82
- Rix, H.-W., de Zeeuw, P. T., Cretton, N., van der Marel, R. P., & Carollo, C. M. 1997, *ApJ*, 488, 702, arXiv:astro-ph/9702126
- Robin, A. C., Reylé, C., Derrière, S., & Picaud, S. 2003, *A&A*, 409, 523
- Salpeter, E. E. 1955, *ApJ*, 121, 161
- Sánchez-Salcedo, F. J., Reyes-Iturbide, J., & Hernandez, X. 2006, *MNRAS*, 370, 1829, arXiv:astro-ph/0601490
- Sánchez-Salcedo, F. J., Saha, K., & Narayan, C. A. 2008, *MNRAS*, 385, 1585, 0712.0816
- Sanders, R. H. 1996, *ApJ*, 473, 117, arXiv:astro-ph/9606089
- . 1997, *ApJ*, 480, 492, arXiv:astro-ph/9612099
- . 2003, *MNRAS*, 342, 901, arXiv:astro-ph/0212293
- . 2005a, *MNRAS*, 363, 459, arXiv:astro-ph/0502222
- . 2005b, *MNRAS*, 363, 459, arXiv:astro-ph/0502222
- Sanders, R. H., & McGaugh, S. S. 2002, *ARA&A*, 40, 263, arXiv:astro-ph/0204521
- Sanders, R. H., & Noordermeer, E. 2007, *MNRAS*, 379, 702, arXiv:astro-ph/0703352
- Sanders, R. H., & Verheijen, M. A. W. 1998, *ApJ*, 503, 97, arXiv:astro-ph/9802240

Schmidt, F., Liguori, M., & Dodelson, S. 2007, *Phys. Rev. D*, 76, 083518, arXiv:0706.1775

Schwarzschild, M. 1979, *ApJ*, 232, 236

———. 1982, *ApJ*, 263, 599

———. 1993, *ApJ*, 409, 563

Seigar, M. S., Barth, A. J., & Bullock, J. S. 2008, *MNRAS*, 389, 1911, arXiv:astro-ph/0612228

Shan, H. Y., Feix, M., Famaey, B., & Zhao, H. 2008, *MNRAS*, 387, 1303, 0804.2668

Skordis, C. 2006, *Phys. Rev. D*, 74, 103513, arXiv:astro-ph/0511591

———. 2008, *Phys. Rev. D*, 77, 123502

Skordis, C., Mota, D. F., Ferreira, P. G., & Boehm, C. 2006a, *Physical Review Letters*, 96, 011301, arXiv:astro-ph/0505519

———. 2006b, *Physical Review Letters*, 96, 011301, arXiv:astro-ph/0505519

Smith, B. F., & Miller, R. H. 1982, *ApJ*, 257, 103

Smith, M. C. et al. 2007, *MNRAS*, 379, 755, arXiv:astro-ph/0611671

Sofue, Y., & Rubin, V. 2001, *ARA&A*, 39, 137, arXiv:astro-ph/0010594

Solanes, J. M., Manrique, A., García-Gómez, C., González-Casado, G., Giovanelli, R., & Haynes, M. P. 2001, *ApJ*, 548, 97, arXiv:astro-ph/0007402

Sollima, A., & Nipoti, C. 2010, *MNRAS*, 401, 131, 0909.1656

Statler, T. S. 1987, *ApJ*, 321, 113

———. 1991, *AJ*, 102, 882

Takahashi, R., & Chiba, T. 2007, *ApJ*, 671, 45

Tempel, E., Tamm, A., & Tenjes, P. 2007, *ArXiv e-prints*, 0707.4374

Tiret, O., & Combes, F. 2007, *A&A*, 464, 517, arXiv:astro-ph/0701011

———. 2008, *A&A*, 483, 719, 0803.2631

Tiret, O., Combes, F., Angus, G. W., Famaey, B., & Zhao, H. S. 2007, *A&A*, 476, L1, 0710.4070

Tremblay, B., & Merritt, D. 1996, *AJ*, 111, 2243, arXiv:astro-ph/9601038

Tully, R. B., & Fisher, J. R. 1977, *A&A*, 54, 661

van der Marel, R. P., Alves, D. R., Hardy, E., & Suntzeff, N. B. 2002, *AJ*, 124, 2639, arXiv:astro-ph/0205161

- van der Marel, R. P., Cretton, N., de Zeeuw, P. T., & Rix, H.-W. 1998, *ApJ*, 493, 613, arXiv:astro-ph/9705081
- Wang, Y.-g., Wu, X., & Zhao, H. 2008, *ApJ*, 677, 1033, 0801.4135
- Wilkinson, M. I., & Evans, N. W. 1999, *MNRAS*, 310, 645, arXiv:astro-ph/9906197
- Wu, X., Famaey, B., Gentile, G., Perets, H., & Zhao, H. 2008, *MNRAS*, 386, 2199, 0803.0977
- Wu, X., Zhao, H., Famaey, B., Gentile, G., Tiret, O., Combes, F., Angus, G. W., & Robin, A. C. 2007, *ApJ*, 665, L101, 0706.3703
- Wu, X., Zhao, H., Wang, Y., Llinares, C., & Knebe, A. 2009, *MNRAS*, 396, 109, 0904.1425
- Xue, X. X. et al. 2008, *ApJ*, 684, 1143, 0801.1232
- Yao, Y., Nowak, M. A., Wang, Q. D., Schulz, N. S., & Canizares, C. R. 2008, *ApJ*, 672, L21, 0711.3212
- Yu, Q., & Madau, P. 2007, *MNRAS*, 379, 1293, 0705.3514
- Yu, Q., & Tremaine, S. 2003, *ApJ*, 599, 1129, arXiv:astro-ph/0309084
- Zhang, P., Liguori, M., Bean, R., & Dodelson, S. 2007, *Physical Review Letters*, 99, 141302, arXiv:0704.1932
- Zhao, H. 2006, *ArXiv Astrophysics e-prints*, astro-ph/0610056
- . 2007, *ApJ*, 671, L1, 0710.3616
- Zhao, H., Bacon, D. J., Taylor, A. N., & Horne, K. 2006a, *MNRAS*, 368, 171, astro-ph/0509590
- . 2006b, *MNRAS*, 368, 171, arXiv:astro-ph/0509590
- Zhao, H., Xu, B.-X., & Dobbs, C. 2008, *ApJ*, 686, 1019, 0802.1073
- Zhao, H. S. 1996, *MNRAS*, 283, 149, arXiv:astro-ph/9512064
- . 2008, *Modern Physics Letters A*, 23, 555, 0802.1775
- Zhao, H. S., & Famaey, B. 2006, *ApJ*, 638, L9, arXiv:astro-ph/0512425
- Zhao, H. S., & Tian, L. 2006, *A&A*, 450, 1005, arXiv:astro-ph/0511754
- Zlosnik, T. G., Ferreira, P. G., & Starkman, G. D. 2007a, *Phys. Rev. D*, 75, 044017, arXiv:astro-ph/0607411
- . 2007b, *Phys. Rev. D*, 75, 044017, arXiv:astro-ph/0607411